



Resource Assessment for Cornwall, Isles of Scilly and PNMI

Task 1.2 of WP3 from the MERiFIC Project

**A report prepared as part of the MERiFIC Project
"Marine Energy in Far Peripheral and Island Communities"**

April 2014

Written by

Helen Smith (h.c.m.smith@exeter.ac.uk), University of Exeter

Christophe Maisondieu (christophe.maisondieu@ifremer.fr), Ifremer

With contributions from

Joana van Nieuwkoop (j.van-nieuwkoop-mccall@exeter.ac.uk), University of Exeter

Abdessalem Bouferrouk (a.bouferrouk@exeter.ac.uk), University of Exeter



MERiFIC was selected under the European Cross-Border Cooperation Programme INTERREG IV A France (Channel) – England, co-funded by the ERDF.

The sole responsibility for the content of this report lies with the authors. It does not represent the opinion of the European Communities. The European Commission is not responsible for any use that may be made of the information contained therein.

© University of Exeter and Ifremer, April 2014

Table of Contents

1	Introduction	10
1.1	The MERiFIC project	10
1.2	This report.....	10
2	Resource assessment overview.....	11
2.1	Measurement	13
2.1.1	Wave measurement.....	13
2.1.2	Tidal measurement.....	16
2.2	Numerical modelling.....	16
2.2.1	Wave modelling.....	17
2.2.2	Tidal modelling.....	18
3	Resource assessment for Cornwall and the Isles of Scilly.....	20
3.1	Measured data	20
3.1.1	Wave data	20
3.1.2	Current data.....	27
3.2	Numerical modelling.....	30
3.2.1	Model set-up	30
3.2.2	Model validation.....	33
3.2.3	23-year hindcast results: Regional.....	35
3.2.4	23-year hindcast results: Site specific.....	37
4	Resource assessment for the Iroise Sea	47
4.1	Measured data	47
4.1.1	Wave data	48
4.1.2	Current data.....	48
4.2	Wave numerical modelling.....	49
4.2.1	Model set-up	49
4.2.2	Model validation.....	51
4.2.3	19-year hindcast results: Regional.....	53

4.2.4	19-year hindcast results: Site specific.....	55
4.2.5	Discussion on site comparison.....	71
4.3	Numerical modelling of currents	73
4.3.1	Current modelling results: Regional.....	73
4.3.2	Current modelling results: Site specific.....	75
4.3.3	Wave-Current interaction	79
5	Conclusions.....	81
6	References.....	82
	Appendix A: Validation testing for the SWAN wave model for SW England	84
	Appendix B: Iroise Sea wave parameters regional maps.....	91

Figures

Figure 1: Varying resource assessment requirements for different project stages (Ingram et al., 2011).....	11
Figure 2: Methods for obtaining key wave parameters through resource assessment (Ingram et al., 2011).....	12
Figure 3: Methods for obtaining key tidal parameters through resource assessment (Ingram et al., 2011).....	12
Figure 4: (a) Seawatch Wavescan buoy (www.oceanor.com), (b) Datawell Waverider buoy (http://www.rsaqua.co.uk), (c) Seawatch Mini II buoy.....	14
Figure 5: Example of (a) an ADP with four acoustic transducers (RDI Workhorse Sentinel), and (b) an anti-trawl bottom mount.....	15
Figure 6: Schematic showing the HF radar system set-up on the north coast of Cornwall, with transmit-receive arrays located at Pendeen and Perranporth. The dashed red circle shows the approximate area of coverage (source: Daniel Conley, Plymouth University).....	16
Figure 7: MARS2D Embedded models.....	19
Figure 8: Locations of the wave buoy and ADP deployments around the Wave Hub and FaBTest sites.....	20
Figure 9: Time series plot of all wave buoy and ADP H_{m0} data records from 2005 to 2013 for the Wave Hub region.....	22
Figure 10: Time series plot of all wave buoy and ADP T_{m02} data records from 2005 to 2013 for the Wave Hub region.....	22
Figure 11: Annual H_{m0} - T_{m02} scatter plot for the Wave Hub region using data from November 2009 to October 2010 from a combination of ADP and wave buoy records.....	23
Figure 12: The measurement sensors: (a) Modified RDI's ADCP with a vertical 5 th beam, and (b) the ADCP in its pyramid-shaped frame.....	24
Figure 13: Comparison of (a) significant wave height, and (b) energy period from the co-located buoy and ADCP measurements, October 2010.....	26
Figure 14: The 5-beam ADCP and a definition of axes: x-axis is east (u velocity), y-axis is north (v velocity) and z-axis is vertical (w velocity), $\theta = 20^\circ$ from the vertical, b_i is beam velocity along beam i, φ_1 is pitch angle, φ_2 is roll and φ_3 is yaw.....	28
Figure 15: 10-minute time-averaged current velocity magnitude and direction: flood (blue) and ebb (red).....	29

Figure 16: 10-minute averaged time histories of the u (blue), v (red) and w (black) components during the deployment period at three bin locations through the water column.....	30
Figure 17: 10-minute time-averaged current velocity profiles over a tidal cycle.....	30
Figure 18: Bathymetry for the regional model domain.....	31
Figure 19: ECMWF model grid (0.5° squares) and every 10 th grid line of the SWAN grid (black dots), with interpolated wave boundary input points (red circles).....	32
Figure 20: The 1km resolution model domain (D ₀) and 100m resolution nested grids (D ₁ , D ₂ , D ₃). The Wave Hub and FaBTest sites are shown as black squares, the coloured circles show detailed model output locations (yellow – north coast measurement location, blue – south coast measurement location) and the green squares show validation locations.....	33
Figure 21: Time series comparison of computed and measured data for Exeter wave buoy D.....	35
Figure 22: Spatial maps of H _{m0} showing the increasing wave height across the region over an 18 hr period in November 2009.....	36
Figure 23: Mean power in kW/m across the region for the 23-year hindcast period.....	37
Figure 24: Time series of power, H _{m0} and T _{m-10} at Wave Hub.....	38
Figure 25: Joint probability distribution for H _{m0} and T _{m-10} at Wave Hub.....	39
Figure 26: Monthly/annual variation of power at Wave Hub.....	40
Figure 27: Monthly/annual variation of H _{m0} at Wave Hub, with bars showing the standard deviation in the data.....	41
Figure 28: Monthly/annual variation of T _{m-10} at Wave Hub, with bars showing the standard deviation in the data.....	42
Figure 29: Seasonal variation of power at Wave Hub.....	43
Figure 30: Wave rose for wave power [kW/m] at location 1, left-hand figure for power < 50 kW/m, right-hand figure for power > 50 kW/m.....	43
Figure 31: Mean wave power (kW/m) binned by wave direction (°N) in 30 degree bins.....	44
Figure 32: Joint probability H _{m0} and T _{m-10} for wave direction bin 240-270°.....	45
Figure 33: Joint probability H _{m0} and T _{m-10} for wave direction bin 270-300°.....	45
Figure 34: Spectral variation, with frequency [Hz] on the x-axis and energy density [m ² /Hz] on the y-axis.....	46
Figure 35: Location map showing the extent of the Iroise Sea (left) and its relationship to the full numerical model domain (right).....	47
Figure 36: Example of a 62069 Wave Buoy Record - Significant Wave height February 2013.....	48

Figure 37: Mean surface current velocity amplitudes over the period 07/2006 - 08/2011.....	49
Figure 38: Iroise Sea wave model computational grid.	50
Figure 39: Model validation - Cross-comparison with buoy 62069.....	52
Figure 40: Model validation - Cross-comparison with Topex altimeter data.....	52
Figure 41: Annual mean global parameters for the Iroise Sea (H_s (m), $T_{m-1,0}$ (s), D_p (°), C_gE (kW/m)).....	54
Figure 42: Reference sites for the site-specific study.....	55
Figure 43: Key statistics for site I5.....	56
Figure 44: Joint distribution of $T_{m-1,0}$ and D_p as a function of H_s – site I5.....	57
Figure 45: Joint distribution of H_s and D_p as a function of C_gE – site I5.	57
Figure 46 : $T_{m-1,0}$ – H_s scatter diagram – site I5.....	58
Figure 47: Monthly/annual variation of significant wave height at site I5.....	59
Figure 48: Monthly/annual variation of energy period at site I5.....	59
Figure 49: Monthly/annual variation of power at site I5.	60
Figure 50: Monthly variability of peak direction at site I5.....	60
Figure 51: Comparison of power angular distribution with wave peak directions at site I5.....	61
Figure 52: Seasonal variations of H_s , $T_{m-1,0}$ and C_gE at site I5.....	61
Figure 53 : Spectral variation at site I5, with frequency (Hz) on the x-axis and energy density (m^2/Hz) on the y-axis.	62
Figure 54 : Joint distribution of H_s and T_e as a function of $\text{Log}_{10}(Q_p)$ at site I5.....	63
Figure 55: Key statistics for site I7.....	64
Figure 56: Joint distribution of $T_{m-1,0}$ and D_p as a function of H_s – site I7.....	65
Figure 57: Joint distribution of H_s and D_p as a function of C_gE – site I7.	65
Figure 58 : $T_{m-1,0}$ – H_s scatter diagram – site I7.....	66
Figure 59: Monthly/annual variation of significant wave height at site I7.....	67
Figure 60: Monthly/annual variation of energy period at site I7.....	67
Figure 61: Monthly/annual variation of power at site I7.	68
Figure 62: Monthly variability of peak direction at site I7.....	68
Figure 63: Comparison of the power angular distribution with wave peak directions at site I7.	69
Figure 64: Seasonal variations of H_s , $T_{m-1,0}$ and C_gE at site I7.....	69

Figure 65 : Spectral variation at site I7, with frequency (Hz) on the x-axis and energy density (m^2/Hz) on the y-axis.	70
Figure 66 : Joint distribution of H_s and T_e as a function of $\text{Log}_{10}(Q_p)$ at site I7.....	71
Figure 67 : Power statistics with 5m H_s threshold - site I5.....	72
Figure 68: Power statistics with 5m H_s threshold - site I7.....	72
Figure 69: Local maximum current velocity in the Iroise Sea.	73
Figure 70: Occurrence of current velocities above a threshold velocity.....	74
Figure 71: Current zonal and meridional components.....	75
Figure 72: Time series of current velocity and direction, and sea level elevation.....	76
Figure 73: Ebb and flood current direction.....	76
Figure 74: Distribution of current velocities.....	77
Figure 75 : Local maximum current power in the Iroise Sea.	78
Figure 76 : Distribution of current power.....	78
Figure 77: Measurement and modelling of significant wave height at buoy 02911/62069.....	79
Figure 78: Fourier analysis of the significant wave height.	79
Figure 79: Influence of tidal currents on significant wave height.....	80
Figure 80: Bias H_{m0} [m] Exeter wave buoy D.....	84
Figure 81: Root mean square H_{m0} [m] Exeter wave buoy D.	85
Figure 82: Bias T_{m-10} [s] Exeter wave buoy D.....	85
Figure 83: Root mean square T_{m-10} [m] Exeter wave buoy D.....	85
Figure 84: Number of observations Exeter wave buoy D.....	86
Figure 85: Scatter plot H_{m0} , Exeter wave buoy D, for different values of T_{m-10} [s] (see colour bar).....	86
Figure 86: Scatter plot T_{m-10} , Exeter wave buoy D, for different values of H_{m0} [m] (see colour bar).....	87
Figure 87: Bias and scatter H_{m0} vs wave direction, Exeter wave buoy D.	88
Figure 88: Bias and scatter T_{m-10} vs wave direction, Exeter wave buoy D.....	88
Figure 89: Montly/annual variation of the errors in H_{m0} and T_{m-10} Perranporth.....	89
Figure 90: Mean monthly error for H_{m0} and T_{m-10} Perranporth.....	90

Tables

Table 1: Summary of wave buoy deployments at the Wave Hub site.....	21
Table 2: Summary of ADCP deployments at the Wave Hub site.	24
Table 3: Deployment details for the 5-beam ADCP and the buoys.	25
Table 4: Coefficient of determination, R^2 , of the linear regression of wave parameters for the wave buoy and ADCP comparison.	26
Table 5: Statistical comparison of ADCP vs. wave buoys for significant wave height.	26
Table 6: Statistical comparison of ADCP vs. wave buoys for the peak period.....	27
Table 7: Statistical comparison of ADCP vs. wave buoys for the energy period.	27
Table 8: Deployment details for the 5-beam ADCP.	28
Table 9: Wave model validation statistics.....	34
Table 10: Significant wave height return values at site I5.	56
Table 11: Significant wave height return values at site I7.	63

1 Introduction

1.1 The MERiFIC project

MERiFIC is an EU project linking Cornwall and Finistère through the ERDF INTERREG IVa France (Manche) England programme. The project seeks to advance the adoption of marine energy in Cornwall and Finistère, with particular focus on the island communities of the Parc Naturel Marin d'Iroise and the Isles of Scilly. Project partners include Cornwall Council, University of Exeter, University of Plymouth and Cornwall Marine Network from the UK, and Conseil Général du Finistère, Pôle Mer Bretagne, Technôpole Brest Iroise, IFREMER and Bretagne Développement Innovation from France.

MERiFIC was launched on 13th September at the National Maritime Museum Cornwall and runs until June 2014. During this time, the partners aim to

- Develop and share a common understanding of existing marine energy resource assessment techniques and terminology;
- Identify significant marine energy resource 'hot spots' across the common area, focussing on the island communities of the Isles of Scilly and Parc Naturel Marin d'Iroise;
- Define infrastructure issues and requirements for the deployment of marine energy technologies between island and mainland communities;
- Identify, share and implement best practice policies to encourage and support the deployment of marine renewables;
- Identify best practice case studies and opportunities for businesses across the two regions to participate in supply chains for the marine energy sector;
- Share best practices and trial new methods of stakeholder engagement, in order to secure wider understanding and acceptance of the marine renewables agenda;
- Develop and deliver a range of case studies, tool kits and resources that will assist other regions.

To facilitate this, the project is broken down into a series of work packages:

- WP1: Project Preparation
- WP2: Project Management
- WP3: Technology Support
- WP4: Policy Issues
- WP5: Sustainable Economic Development
- WP6: Stakeholder Engagement
- WP7: Communication and Dissemination

1.2 This report

This report provides an overview of resource assessment techniques for marine energy developments and the requirements at different stages of project development. It then details the studies that have been completed in Cornwall and the Isles of Scilly (Section 3) and Finistère and PNMI (Section 4). These studies combine shorter-term in situ measurements, using a range of measurement technologies, and numerical modelling to provide long-term and geographically diverse records.

2 Resource assessment overview

Resource assessment is the process of characterising both the level of resource available for conversion into electrical energy and the detailed physical environment for engineering design. The level of detail required from a resource assessment study will vary with the *stage* of a project development, as defined in Figure 1 (from Ingram *et al.*, 2011). Early stage assessment involves establishing first order characteristics of the wave climate, i.e. the key parameters, over a sufficient geographical extent and timescale to enable an optimal site to be selected and long-term resource variability defined. Once a site has been selected, a more detailed assessment is performed as part of the project development stage. This will involve defining the detailed sea state characteristics such as the spectral shape to provide data for the engineering design process. Temporal variability is also key, in order to develop plans for deployment operations and maintenance. Resource assessment continues to play a role once a site is operational; forecasts are required for power output predictions, and the resource must be continually monitored to benchmark against actual power production.

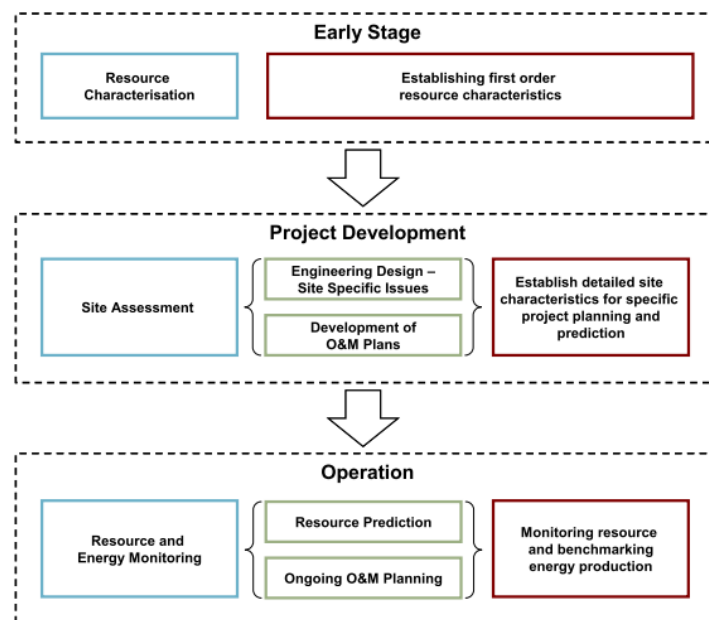


Figure 1: Varying resource assessment requirements for different project stages (Ingram *et al.*, 2011).

Two methods are available for performing resource assessment studies; direct measurement and numerical modelling. Resource measurement has the advantage of providing highly accurate data, however, measurement programmes are typically limited to a single location per measurement device (with the exception of remote sensing techniques, which provide data over a wide geographical area) and instruments are expensive and vulnerable to damage. Measurement data are therefore typically spatially and temporally limited, and usually insufficient on their own for a marine energy resource assessment. Numerical modelling is therefore used as part of the resource assessment process to complement the available measured data. Long-term model data can be produced over wide geographical areas, allowing trends in the data to be identified. Although providing a lower level of accuracy than direct measurement, modelling should be used in conjunction with a measurement programme to allow for comparison between the two datasets for the purposes of calibration and validation.

Summaries of how measurement and model data are utilised for resource assessment for wave and tidal projects are shown in Figure 2 and Figure 3.

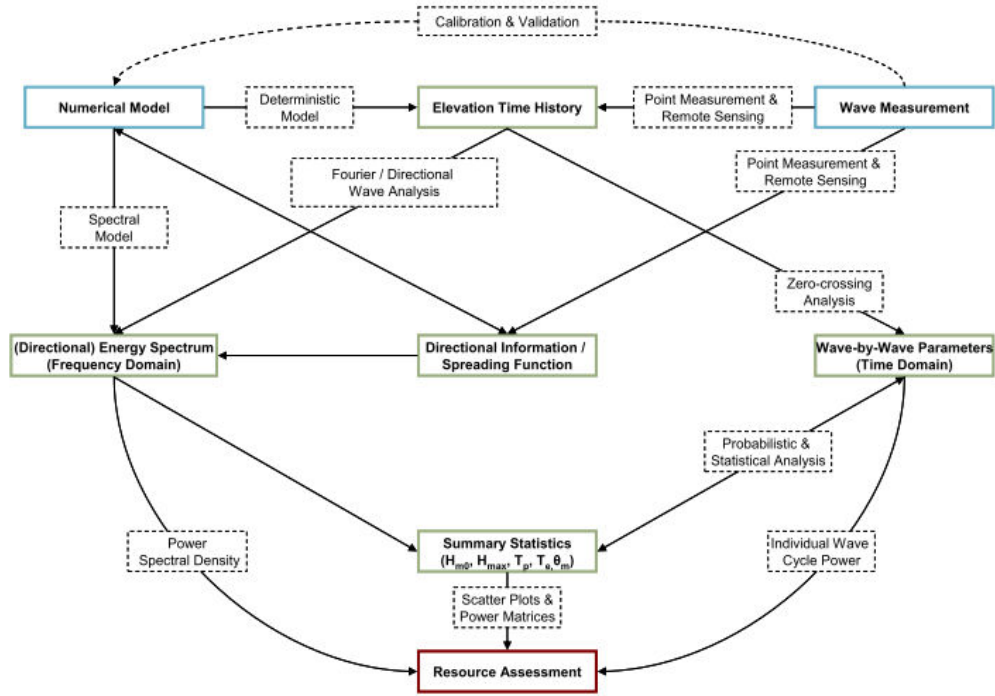


Figure 2: Methods for obtaining key wave parameters through resource assessment (Ingram *et al.*, 2011).

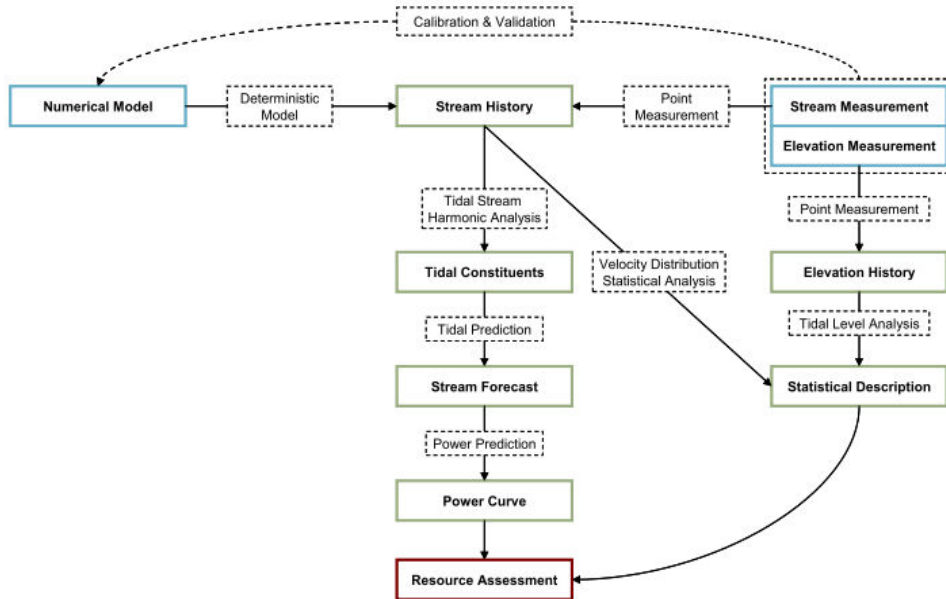


Figure 3: Methods for obtaining key tidal parameters through resource assessment (Ingram *et al.*, 2011).

2.1 Measurement

The most commonly used wave measurement technologies are wave buoys and acoustic Doppler profilers (ADPs), both of which are point measurement devices. However, radar systems such as HF or X-band radar are increasingly being deployed for wave measurement studies, with the advantage over point measurement devices of providing data over a wide geographical area. Tidal measurement typically employs ADPs, although current meters are still used for short-term measurement studies and radar systems can also be used to measure tidal currents. These measurement techniques are described below, with the wave measurement technologies presented in Section 2.1.1 and the tidal technologies in Section 2.1.2.

2.1.1 Wave measurement

Wave buoys

Buoys used for wave measurement are surface following buoys, and they can be categorised based on their mode of operation: pitch-roll-heave (PRH) buoys follow the surface slope of the wave, and particle-following buoys follow the sea surface water particle orbits. PRH buoys, for example the Fugro Oceanor Seawatch Wavescan buoy (Figure 4a), were the earliest directional wave buoys to be developed and were first deployed in the 1960s. By following the surface slope of the waves, they record the triplet measurements of time series of the vertical (heave) acceleration and two orthogonal components of the surface slope (pitch and roll). Particle-following buoys, such as the Datawell Waverider (Figure 4b) and the Fugro Oceanor Seawatch Mini II (Figure 4c) are designed to follow the water particle orbits at the surface, and an accelerometer housed within the buoy measures the acceleration (from which displacement can be calculated) along the heave, N-S and E-W axes, thus also providing a triplet measurement.

From the triplet measurements of either sensor type, a directional spectrum can be estimated using the theory of Longuet-Higgins, et al. (1963) to calculate the auto- and cross-spectra between the records, and spectral parameters can thus be computed. Data is typically processed on-board, and both raw and processed data may be stored or transmitted to shore via a radio or satellite link.

PRH buoys are designed to operate in offshore locations, and are used world-wide for long-term wave measurement programmes. However for marine energy resource assessment purposes, which are likely to involve shorter term deployments in coastal regions, particle-following buoys are often considered to be a better option due to their lower cost, smaller size, increased robustness, and less complex moorings.

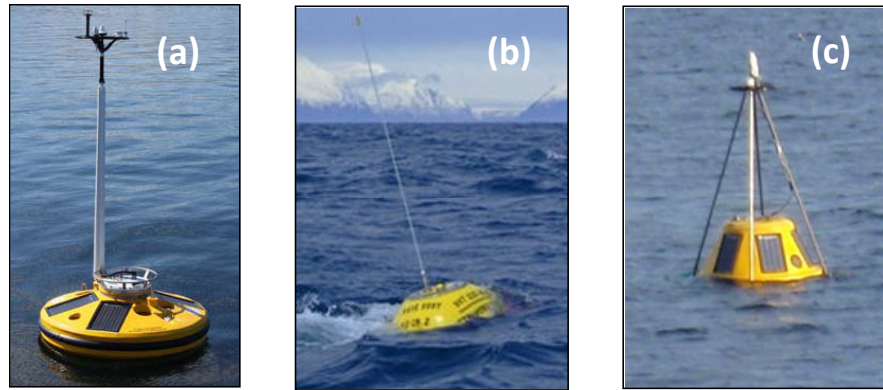


Figure 4: (a) Seawatch Wavescan buoy (www.oceanor.com), (b) Datawell Waverider buoy (<http://www.rsaqua.co.uk>), (c) Seawatch Mini II buoy.

Wave buoys are generally considered to provide the most accurate data of the available wave measurement technologies. However, individual units are costly, and due to their surface deployment they are vulnerable to damage from shipping. Care must be taken with the mooring arrangement to ensure minimal impedance to the buoy motion. Additionally, calibration studies must be performed pre- and post-deployment. If buoys are to remain on-station for periods greater than 6-12 months, maintenance will be required to replace batteries, service the instrument and re-calibrate.

ADPs

An ADP is an instrument designed to measure currents in the water column through the Doppler shift of backscattered acoustic signals from 'scatterers', i.e. particulate matter suspended in the water column and moving at the same speed as the water particles. An ADP with four acoustic transducers is shown in Figure 5a. However, the measurement technology can also be applied to the wave orbital velocities, allowing computation of the wave elevation time series and the directional spectrum. ADPs may also have the capability to operate as an inverted echo-sounder with an upward facing beam transmitting a signal that reflects off the water surface, thereby producing a time series of surface elevation from which a non-directional spectrum can be computed. Some instruments also contain a pressure sensor, which records the changing dynamic pressure as waves pass overhead, again producing a time series of surface elevation. However, pressure sensor records are only accurate in comparatively shallow waters due to the attenuation of the pressure signal with depth.

ADPs are usually deployed on the seabed with anti-trawl mountings to avoid entanglement with nets (Figure 5b), and are therefore less vulnerable to damage than surface measurement devices. However, unless connected to a surface buoy with transmission capabilities or to shore via a subsea cable, they are unable to transmit data, and therefore require frequent recovery visits to retrieve data. The following factors affect the accuracy of the measured data, and must be considered if an ADP is to be used as the primary method of wave measurement:

- Beam spreading will lead to decreased measurement resolution as the beam diverges with distance from the instrument. This means lower wavelength (higher frequency) waves will not be measured, effectively introducing a high frequency cut-off to the spectrum.
- Long, low swell exhibits close to horizontal particle motion, and if the instrument is unable to resolve the vertical motion, the calculation of the directional spectrum will not be possible.

- Bubbles in the water column due to turbulence or marine life will lead to measurement inaccuracies.

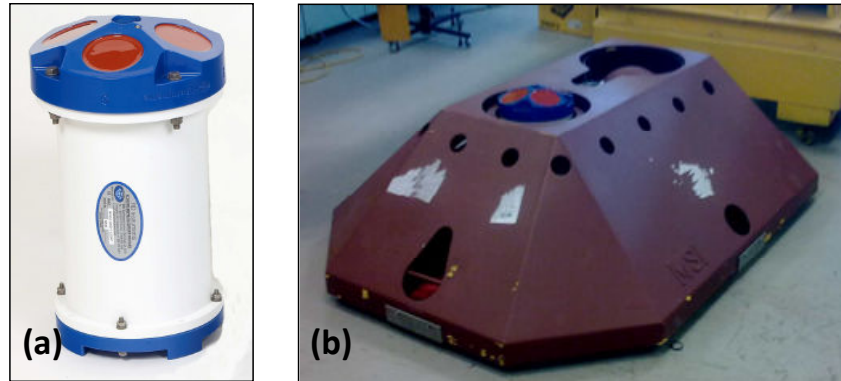


Figure 5: Example of (a) an ADP with four acoustic transducers (RDI Workhorse Sentinel), and (b) an anti-trawl bottom mount.

Radar

Radar systems provide land- or ship-based methods of wave measurement that enable data to be collected over a wide geographical area (up to 150 km). Although wave measurement is a relatively new application of such systems, two types of radar are predominantly being developed to meet these needs: HF (high frequency) and X-band radar.

HF radar is a land-based system, operating in the 3-30 MHz frequency range, i.e. radar wavelengths of the same order as ocean waves. A typical system comprises two shoreline transmit-receive stations with overlapping transmission regions, located sufficiently far apart that their radar bearings are as close as possible to 90°. It uses the phenomenon of Bragg scattering, through which the transmitted radio signal is scattered by ocean waves of exactly half the frequency of the signal. By recording the shape of the spectrum produced by the Doppler shift of the back-scattered signal, the directional spectrum of the ocean waves can be obtained through the use of inversion techniques in post-processing, and wave parameters thus calculated. HF radar systems can provide measurements with a temporal resolution of up to 10 minutes and a spatial resolution up to approximately 1km over an area of 40 km x 40 km, although as the area of coverage increases, the spatial resolution will decrease. Figure 6 shows a schematic of an HF radar system set-up.

X-band radar is primarily used as a shipping management and navigation tool, with installations on most marine structures and large vessels. It uses the same principal of Bragg scattering as HF radar, but transmits shorter, ~3 cm electromagnetic waves which interact with ripples on the sea surface.

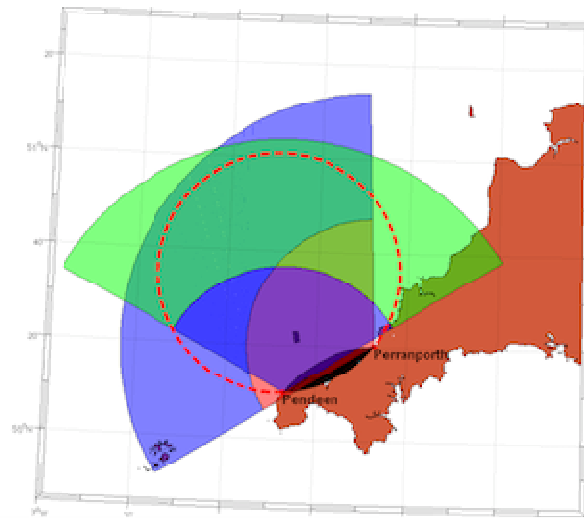


Figure 6: Schematic showing the HF radar system set-up on the north coast of Cornwall, with transmit-receive arrays located at Pendeen and Perranporth. The dashed red circle shows the approximate area of coverage (source: Daniel Conley, Plymouth University).

2.1.2 Tidal measurement

ADPs

ADP measurement of tidal currents employs a similar methodology as the wave measurement, however, instead of measuring the orbital velocities of the surface water particles, the ADP measures particle velocities due to ocean and tidal currents. The device beams are split into cells, or bins, usually of the order 0.5 – 1 m in length. By averaging the velocities recorded in each bin, a current profile throughout the water column can be acquired.

Radar

HF radar systems are also used to produce fields of current velocities and directions. By measuring the difference in the Doppler shift from that expected due to the wave speed, the current velocity can be calculated. When two or more transmit-receive stations are used, the directional properties of the currents can also be found.

2.2 Numerical modelling

The wave models typically used for resource assessment studies are third-generation spectral models, including the global Wavewatch III and WAM, and the nearshore SWAN and TOMAWAC. Tidal models, such as ROMS, MIKE, MARS and TELEMAC use hydrodynamic modelling techniques to compute sea levels and currents. A detailed description of all these models is provided in MERiFIC deliverable 3.4.5, “*Best practice report – application of numerical models and codes*”. Overviews of the models used for the resource assessment studies described in the report are provided in Sections 2.2.1 (wave models) and 2.2.2 (tidal models) below.

2.2.1 Wave modelling

SWAN

SWAN (Booij *et al.*, 1999) is a third-generation spectral wave model, developed by Delft University of Technology and freely available to download. It is therefore commonly used in academic and research institutions and also within industry. SWAN has been specifically developed to model nearshore wave propagation, and can simulate nearshore wave transformation and dissipative processes including refraction, bottom friction, depth-induced breaking and triad wave-wave interactions. It has been extensively used around the globe for marine energy resource assessment studies, e.g. Kim *et al.* (2011), Iglesias and Carballo (2010) and Akpınar and Komurcu (2012).

SWAN computes the evolution of wave action density, N , with time, t , using the action balance equation:

$$\frac{\partial N}{\partial t} + \frac{\partial}{\partial \lambda}(c_\lambda N) + \frac{\partial}{\partial \varphi}(c_\varphi N) + \frac{\partial}{\partial \theta}(c_\theta N) + \frac{\partial}{\partial \sigma}(c_\sigma N) = \frac{S_{tot}}{\sigma} \quad \text{Equation 1}$$

The terms on the left-hand side of equation 1 represent, respectively, the change in wave action over time, the propagation of wave action in geographical space, depth and current-induced refraction (with propagation velocity c_θ in directional space θ) and the shifting of the relative radian frequency σ due to variations in mean current and depth (with the propagation velocity c_σ). The right-hand side of equation 1 represents processes that generate, dissipate or redistribute wave energy, given by:

$$S_{tot} = S_{in} + S_{wc} + S_{nl4} + S_{bot} + S_{br} + S_{nl3} \quad \text{Equation 2}$$

These include the deep water processes of wind input (S_{in}), whitecapping dissipation (S_{wc}), quadruplet nonlinear interaction (S_{nl4}), and the shallow water processes of bottom friction dissipation (S_{bot}), depth-induced breaking (S_{br}) and triad wave-wave interactions (S_{nl3}).

SWAN propagates wave conditions across a bathymetric grid with typical resolution 200m – 1000m, although higher resolution grids can be used if computational facilities allow. Stationary or time-varying wave parameters or spectra must be defined at the grid boundaries, and optional grids of wind and current data can also be incorporated. Both wave parameters and spectra can be output at individual locations within the grid for site-specific investigations, or maps of varying parameters across the grid produced for more geographically diverse studies.

A large number of the parameters describing the various processes within the model are user-defined (although default values are recommended), therefore, where available measurement data allows, model calibration and validation studies should be performed to assess the optimal values of parameters and the accuracy of the model output.

Wavewatch III

WaveWatch III© (WW3 hereafter) is the ocean wave model developed at NOAA/NCEP. WW3 is a phase-averaged wave model resolving the random phase spectral action density balance equation for wavenumber-direction spectra (Tolman, 1999), similar to equations 1 and 2. A major assumption in this equation is that currents and water depth vary in time and on space scales much larger than those of a single wave. Source terms describing parameterisation of the physical processes include :

- Wave growth and decay due to wind action
- Nonlinear resonant interactions
- Energy dissipation induced by 'whitecapping', bottom friction, surf-breaking
- Scattering due to wave-bottom interactions.

Forcing fields include winds, water level and currents. Ice coverage can also be dynamically updated.

Use of unstructured computational grids is available. A large number of global wave parameters, such as significant wave height, periods and directions can be saved as output on this grid, including partitioned wave field information. Additionally, wave directional spectra can be saved at selected locations.

Version 3.14 of the model was released in 2009. An updated version, 4.18, was released early 2014.

2.2.2 Tidal modelling

MARS2D/3D

The MARS model (Model for Application at Regional Scale) is a hydrodynamic model developed at IFREMER designed for the simulation of flows in coastal areas from the regional scale down to the scale of small bays or estuaries where circulation is generally driven by complex processes (Lazure and Dumas, 2008).

Navier-Stokes equations are simplified using the classic Boussinesq approximation and hydrostatic assumption, considering small horizontal scales compared to the earth radius together with small space vertical scales compared to the horizontal scale. In addition, thermodynamics is introduced through equations taking temperature and salinity fields into account. Mixing processes in the boundary layer are described introducing turbulence equations.

Equations are solved on an ARAKAWA C type horizontal grid (Arakawa, 1966) using a sigma coordinate system (Blumberg and Mellor, 1987). A specificity of the MARS model is the coupling between the barotropic and baroclinic modes using a semi-implicit method for the time integration (A.D.I).

Various configurations of the Mars model are used in the operational forecast service Previmer (www.previmer.org) covering the Channel and North-east Atlantic as well as the Mediterranean Sea. Three levels of embedded models are coupled. For the Mars 2D version where currents are averaged along the vertical axis in the water column, meshes size ranges from 2.5 km for the coarse grid of the regional model (with a one hour time step) down to 250 m for the refined grid of the local models (with a 1/4 hour time step).

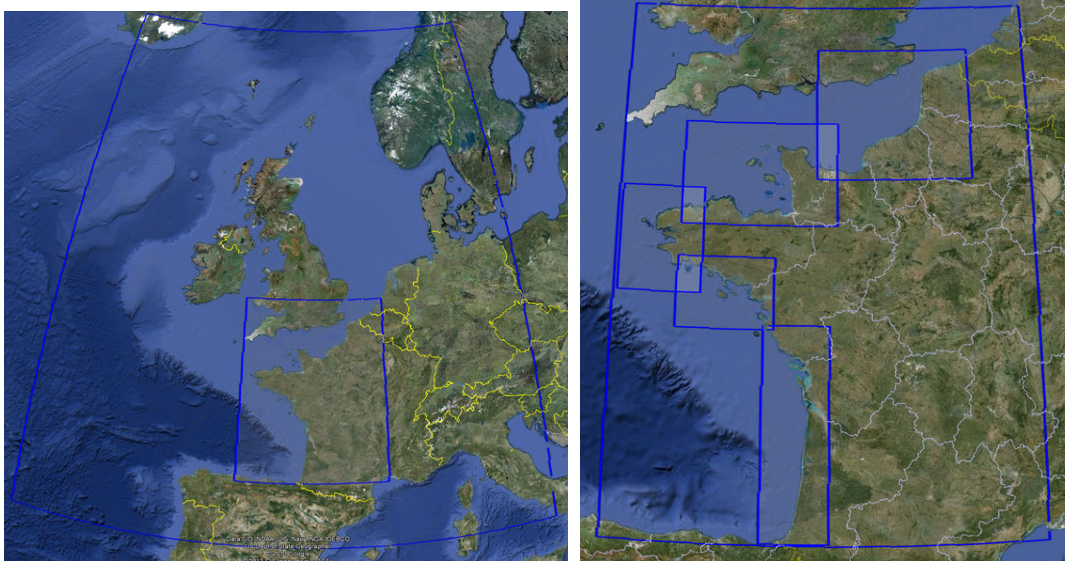


Figure 7: MARS2D Embedded models.

Mesh sizes of the MARS3D model, providing output at 30 levels through the water column, range from 4 km on the coarse regional grid down to 2.5 km on the local grids. Currents, sea water level, surges, temperature and salinity are provided. Additional modules for computation of Lagrangian transport or sediment transport can also be coupled to the MARS models (Le Hir *et al.*, 2011).

3 Resource assessment for Cornwall and the Isles of Scilly

This section provides an overview of the resource assessment studies that have been performed to determine the available wave and tidal resource for Cornwall and the Isles of Scilly over the last decade. The equivalent data for the Iroise Sea, Finistère, France is provided in Section 4. The two primary areas of interest for direct and remote sensing measurement programmes are the two wave energy test sites and their immediate surroundings. Wider geographical assessment is provided by longer-term numerical modelling studies.

3.1 Measured data

3.1.1 Wave data

Wave buoys

Buoy deployments have been made in Cornish waters to support the development of both the Wave Hub and FaBTest sites. Since 2005, a series of buoy measurement programmes have been established, some run by commercial consultancies and others by the University of Exeter. Details of the instrumentation and the data acquired from each deployment are summarised in Table 1 below, and a map of the locations is provided (Figure 8).

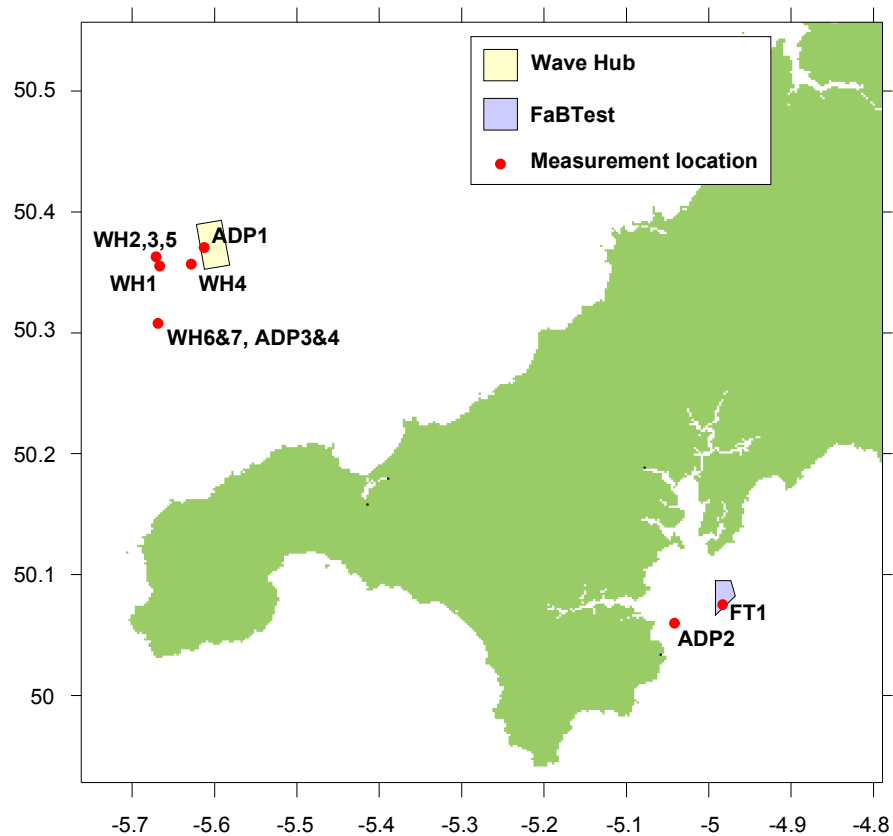


Figure 8: Locations of the wave buoy and ADP deployments around the Wave Hub and FaBTest sites.

Table 1: Summary of wave buoy deployments at the Wave Hub site.

Dataset	Instrument	Dates deployed	Operator	Mean depth (m)	Sampling interval	Data formats
WH1	Seawatch mini buoy	Jan 05 – Nov 05	Halcrow	52	2 hr	Raw, spectral, parameters
WH2	Datawell directional Waverider buoy	Dec 05 – Jan 06	Halcrow	52	1 hr	Spectral, parameters
WH3	Datawell directional Waverider buoy	Jan 06 – Apr 06	Halcrow	52	1 hr	Spectral, parameters
WH4	Datawell directional Waverider buoy	Dec 06 – Mar 07	Halcrow	52	1 hr	Spectral, parameters
WH5	Triaxys directional wave buoy	Feb 08 – Mar 09	Halcrow	52	1 hr	Parameters
WH6	4 x Seawatch mini II buoys	Oct 09 – Nov 10	University of Exeter	45	30 mins	Raw, spectral, parameters
WH7	2 x Seawatch mini II buoys	Jul 11 – Jan 12	University of Exeter	45	30 mins	Raw, spectral, parameters
FT1	Seawatch mini II buoy	Mar 12 – Aug 13	University of Exeter	45	30 mins	Raw, spectral, parameters

Figure 9 shows the time series record from 2005 to 2013 of the recorded significant wave height, H_{m0} , from the buoys and ADP deployed in the vicinity of the Wave Hub site, and Figure 10 shows the equivalent mean period, T_{m02} , data. All data have been subjected to appropriate quality control checks, described fully by Tucker (1993) and Ashton (2011). Data from the FaBTest site have not been included here because processing and quality control are ongoing. The data plots clearly show the large gaps in the time series of measurements over an 8-year period, and highlight the problems with long-term *in situ* measurement programmes and their ability to deliver uninterrupted datasets.

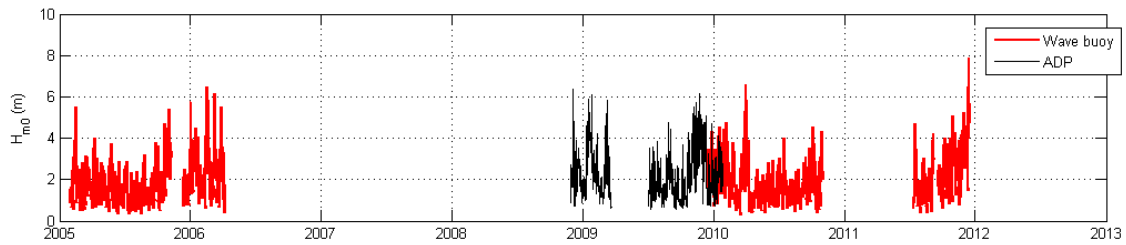


Figure 9: Time series plot of all wave buoy and ADP H_{m0} data records from 2005 to 2013 for the Wave Hub region.

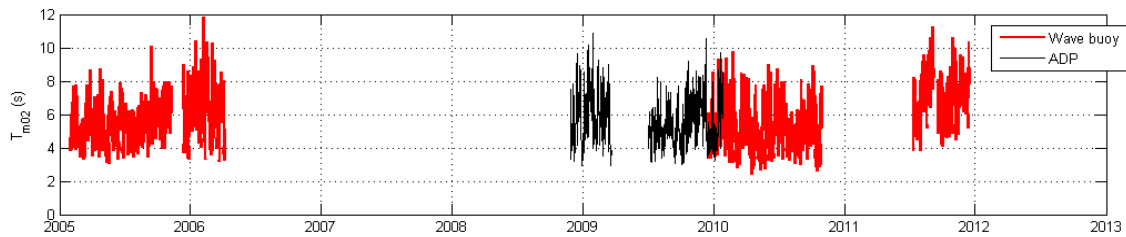


Figure 10: Time series plot of all wave buoy and ADP T_{m02} data records from 2005 to 2013 for the Wave Hub region.

Another constraint on the data use caused by the gaps is that no single instrument provides a full year of data to enable, for example, an annual scatter diagram illustrating the joint distribution probability of the wave height and period. Although the WH1,2&3 and WH6&7 datasets each provide over ten months of data for a single year, the missing data in both cases are from the energetic months of November and December. Constructing a scatter diagram which excludes data from these months risks significantly under-representing the overall resource for the region. In order to provide a full-year scatter plot, data from December 2009 – October 2010 from one of the four buoys in the array has been combined with data from November 2009 – December 2009 from the Wave Hub ADP to produce an H_{m0} - T_{m02} scatter plot (Figure 11). Although the two measurement locations are approximately 5km apart, this provides a better overview of the annual resource at Wave Hub than a scatter plot excluding 1.5 months of data.

For further details on variations in the resource measured by different instruments and at different locations, see Smith *et al.*, 2013.

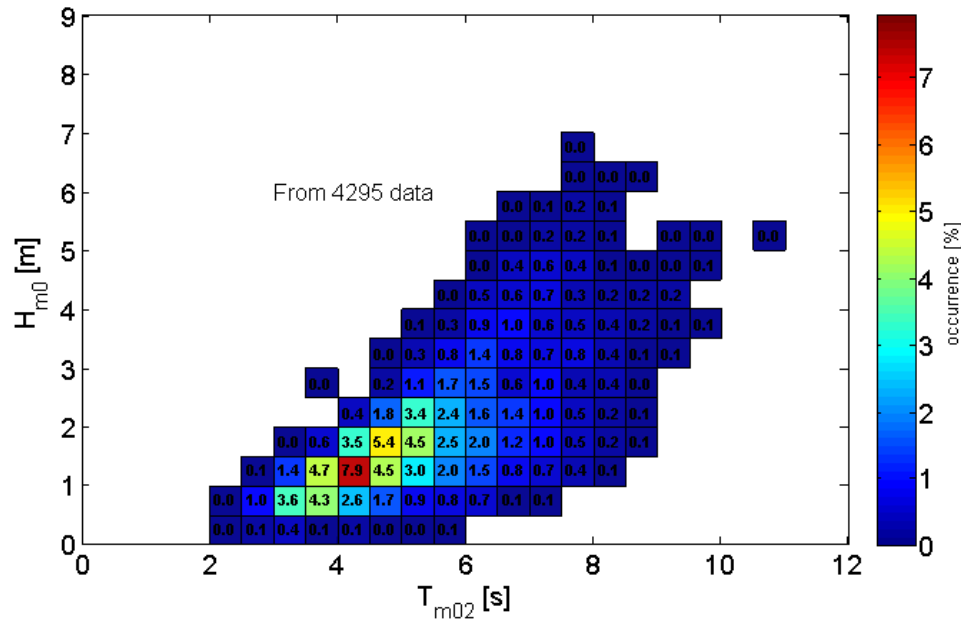


Figure 11: Annual H_{m0} - T_{m02} scatter plot for the Wave Hub region using data from November 2009 to October 2010 from a combination of ADP and wave buoy records.

ADPs

The initial measurement program at Wave Hub switched from using wave buoys to an acoustic Doppler profiler (ADP) in November 2008 due to successive losses of wave buoys and the large costs incurred. Three successful ADP deployments were completed at the Wave Hub site (ADP1), however, the instrument chosen for this deployment (a Nortek AWAC) only delivered parameter data and not spectra. The measured data are illustrated in Figure 9 and Figure 10. After the instrument was lost in January 2010, the measurement programme was discontinued.

Subsequently however, two short term deployments of a modified 5-beam instrument (ADP3 and ADP4) were made at the site of the four buoy array to enable detailed comparisons between buoy and ADP data. These datasets included spectral information as well as parameter data and sea surface elevation time series. An ADP was also been deployed in Falmouth Bay at the South West Moorings Test Facility (SWMTF) site (ADP2) to provide sea state data to support the testing of mooring line configurations. The locations of all deployment sites are shown in Figure 8. This section of the report focuses primarily on the detailed data acquired by the modified instrument deployed at the wave buoy array site, a Teledyne RDI Workhorse Sentinel 300 kHz ADCP (Acoustic Doppler Current Profiler) with four inclined beams (each at 20° off the vertical) and an integrated vertical 5th beam (see Figure 12).

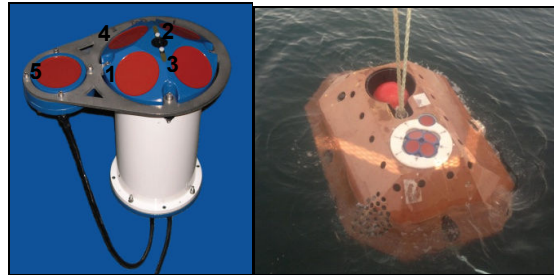


Figure 12: The measurement sensors: (a) Modified RDI's ADCP with a vertical 5th beam, and (b) the ADCP in its pyramid-shaped frame.

Table 2: Summary of ADCP deployments at the Wave Hub site.

Dataset	Instrument	Dates deployed	Operator	Depth (m)	Sampling interval	Data formats
ADP1	Nortek AWAC ADCP, 600kHz	Nov 08 – Mar 09 ¹ Jul 09 – Jan 10	Halcrow	60.0	2 hr	Parameters
ADP2	Teledyne RDI Workhorse Sentinel	Sep 10 – Oct 10	University of Exeter	25	17 min	Parameters
ADP3	Teledyne RDI Workhorse Sentinel	Oct 10	University of Exeter	45	30 min	Raw, spectral, parameters
ADP4	Teledyne RDI Workhorse Sentinel	Jul 11 – Sep 11	University of Exeter	45	30 min	Raw, spectral, parameters

Notes:

¹A single instrument was used throughout the measurement period, with data retrieval occurring on 21/03/09, 01/07/09, 10/08/09 and 27/01/09. On 01/07/09, it was found that the instrument had failed to record during the previous deployment period, hence the gap in the dataset.

In order to measure non-directional waves, the 5-beam ADCP offers three independent methods: (i) direct surface tracking operated by the vertical beam (labelled 5 in Figure 12), (ii) orbital velocities measured by the inclined beams (numbered 1 to 4 in Figure 12), and (iii) the built-in ADCP pressure sensor. The velocity-based surface displacement spectra are derived from a translation of the orbital velocity spectra using linear wave kinematics and involves some complex array processing e.g., using the maximum likelihood method. This technique is limited by the depth dependent array and the rapid attenuation of orbital velocities with depth, especially at high wave frequencies. The rapid decay of water particle motions with depth, leading to a weak wave-induced pressure signal, is the same reason why wave data from the pressure sensor are confined to low frequencies (here 0.12 Hz maximum), making it an unreliable measurement at 40 m. The acoustic surface tracking by the vertical beam circumvents the depth limitations of pressure and orbital velocity. In a standard 4-beam 'Janus' setup, the water column is discretised to achieve both good surface tracking and low velocity

variance. With a 5-beam ADCP, however, the vertical beam is dedicated to high resolution surface tracking while the slant beams are optimised for low velocity variance to compute directional wave spectra. This independent optimised setup for the ADCP beams is reflected in the size and number of acoustic bins for each: 15 x 4 m cells for the inclined beams and 100 x 21 cm cells for the vertical beam (see Table 3). The number and size of ADCP bins were recommended by the manufacturers to give a good balance between resolution, accuracy, and power consumption. RDI's processing software WavesMon has a built-in linear interpolation algorithm associated with the surface tracking which improves the vertical resolution by a factor of $\sqrt{12}$, meaning the actual bin size is as small as 6 cm. The selected vertical cells exclude the near-bottom and near-surface bins that might be affected by bottom and surface effects respectively. The pressure signal provides a redundant measurement of average water depth. Attached to the inside bottom of the frame is an acoustic release with a pop-up float buoy to recover the unit.

A comparison between data from the 5-beam ADCP and from the four buoys was undertaken, with details of the deployments given in Table 3. The frequency range covered by both sets of measurements (0.05 - 0.50 Hz) is typical of the wave climate at the site.

Table 3: Deployment details for the 5-beam ADCP and the buoys.

Parameter	300 kHz 5-beam ADCP	Directional wave buoys
Deployment period	12-23 Oct 2010	Oct 2009- Oct 2010, except periods of maintenance/failure
Burst interval	Continuous	~17.07 minutes @ start and middle of every hour
Sampling frequency	2 Hz: waves & currents	2 Hz for waves
Length of processed time series per burst	2048	2048
Low cut-off frequency	0.05 Hz	0.05 Hz
High cut-off frequency	0.5 Hz	0.5 Hz
Blanking distance	6.25 m	n/a
Number of bins	15 for slant beams, 100 for vertical	n/a
Size of bins	4 m for slant beams, 21 cm for vertical	n/a

In Figure 13 the time-series of parameters H_{m0} and T_{m-10} as estimated by the ADCP's vertical beam and the buoys are shown. The coefficients of determination, R^2 , of the linear regression of the data comparison are summarised in Table 4. Table 5, Table 6 and Table 7 give the bias, relative bias, root mean square error (RMSE) and scatter index (SI = RMSE / mean (buoy data)) between the ADCP and each buoy. For all parameters except T_p a very good correlation is found, without any substantial bias (always < 8%, except T_p). The scatter index is very low for T_{m-10} (~9%), and slightly higher for H_{m0} (~12%).

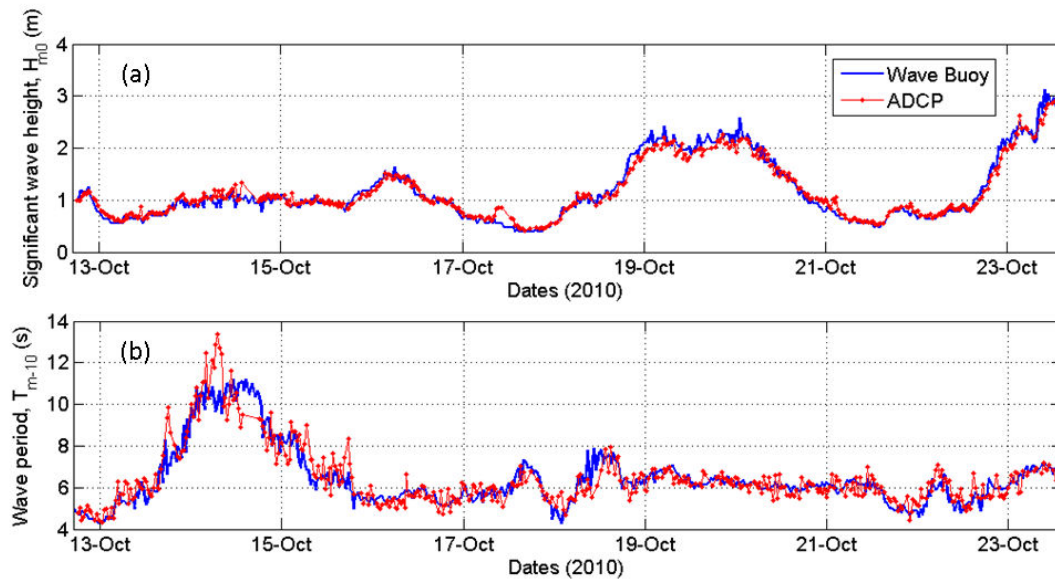


Figure 13: Comparison of (a) significant wave height, and (b) energy period from the co-located buoy and ADCP measurements, October 2010.

Table 4: Coefficient of determination, R^2 , of the linear regression of wave parameters for the wave buoy and ADCP comparison.

R^2 ADCP vs. buoy	Buoy A	Buoy B	Buoy C	Buoy D
T_p [s]	0.46	0.36	0.38	0.36
H_{m0} [m]	0.96	0.96	0.96	0.96
T_{m-10} [s]	0.90	0.88	0.89	0.88

Table 5: Statistical comparison of ADCP vs. wave buoys for significant wave height.

H_{m0}	Buoy A	Buoy B	Buoy C	Buoy D
Bias [m]	-0.05	-0.04	-0.05	-0.03
Rel. bias [%]	-4.1	-3.1	-4.0	-2.2
RMSE [m]	0.14	0.14	0.14	0.13
SCI [%]	11.6	11.7	11.9	10.8

Table 6: Statistical comparison of ADCP vs. wave buoys for the peak period.

T_p	Buoy A	Buoy B	Buoy C	Buoy D
Bias [s]	0.7	1.0	0.9	1.1
Rel. bias [%]	8.5	12.8	11.6	14.5
RMSE [s]	2.6	2.9	2.8	2.9
SCI[%]	32.3	37.9	36.5	38.6

Table 7: Statistical comparison of ADCP vs. wave buoys for the energy period.

T_{m-10}	Buoy A	Buoy B	Buoy C	Buoy D
Bias [s]	0.1	0.3	0.1	0.3
Rel. bias [%]	2.2	4.4	2.1	4.0
RMSE [s]	0.5	0.6	0.5	0.6
SCI [%]	8.0	9.2	8.0	9.0

HF radar

Wave height data is available from the Plymouth University HF radar installations on the north coast of Cornwall from March 2011. Full details of the data collected and the processing methods used in their analysis are provided in the MERiFIC deliverable 3.1.4, *“Processing and Analysis of HF Radar Measurements of Currents and Sea States in the Iroise and Celtic Seas”*.

3.1.2 Current data

ADPs

Tidal data were collected in parallel with wave data by all ADPs deployed in the region (Table 2). However, the data presented in this section derive from measurements by the same 300 kHz 5-beam ADCP Workhorse, sampling at 2 Hz, that was deployed at the site of the wave buoy array. The deployment encompassed one period of neap tide and the majority of a period of spring tide. In addition to the wave data acquired, the ADCP simultaneously measured current velocities at 15 bin locations through the water column along the four inclined beams, with bin size 4m. Details of the deployment for current measurements are shown in Table 8. An illustration of the 5-beam ADCP, with a definition of the axis system and geometrical angles, is shown in Figure 14.

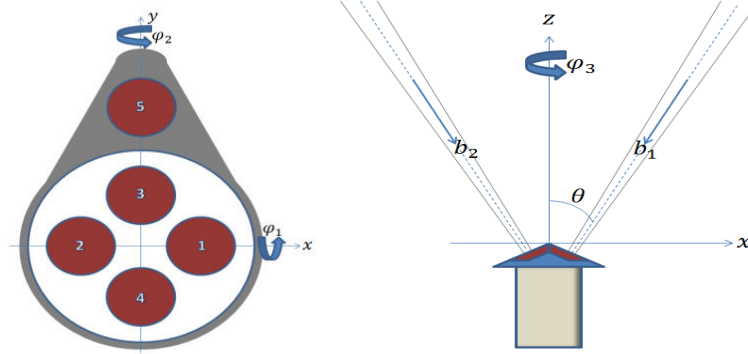


Figure 14: The 5-beam ADCP and a definition of axes: x -axis is east (u velocity), y -axis is north (v velocity) and z -axis is vertical (w velocity), $\theta = 20^\circ$ from the vertical, b_i is beam velocity along beam i , φ_1 is pitch angle, φ_2 is roll and φ_3 is yaw.

From the raw ADCP data, time series of along-beam velocities were output using RDI's BBLList utility. Processing through the software provides a good degree of data quality assurance, with samples corresponding to specific signal to noise ratios and correlations of less than 70% removed. Within the software a standard test is implemented to screen out data points with four standard deviations or more. Further quality control procedures were applied to the time series current data to remove outliers, and spline interpolation was used to account for missing data (typically $< 1\%$) in order to minimise effects of bias on the computation of turbulent parameters. The instantaneous current velocities (at 2 Hz), recorded in ADCP beam coordinates, were transformed into the cartesian system (u, v, w) , where directions of horizontal velocities u and v and vertical component w are positive to east, north and upwards, respectively. The measurements start at 6.2 m above the seabed. With reference to Figure 14, the pair of beams 1 and 2 resolve for u and w while beams 3 and 4 resolve for v and w .

Table 8: Deployment details for the 5-beam ADCP.

Parameter	Details
Burst strategy	Continuous
Sampling frequency	2 Hz
Samples per burst	2048
Blanking distance	6.2 m
Number of bins	15
Bin height	4 m

Ten minute time-averaged Earth-fixed u , v and w velocities were used to understand the underlying nature of the mean flow. Figure 15 shows current velocity variations clearly illustrating some bi-directionality between ebb and flood. There is, however, slightly more directional scatter during the flood compared with the ebb phase. For both ebb and flood there is slightly more directional spread at slower velocities. The mean directions from north are

248° and 66° for flood and ebb respectively. Time-histories of 10-minute time-averaged u , v and w velocities during the deployment period are shown in Figure 16 for three bin locations through the water column. It can be seen that the vertical component is very small compared with the horizontal u and v components. The flood velocities appear to be only slightly greater than the ebb on most tidal cycles. Mean current profiles plotted against water height above the seabed are shown in Figure 17, illustrating sheared profiles with the highest velocities observed near the surface. Only 10 bins are shown for the mean velocity profiles because the remaining ones contained too much spurious data that could not be used to derive statistics. Throughout the profile, the current magnitude during flood is greater than that during ebb by about 0.1 ms^{-1} . The qualitative profiles of mean velocity during low and high waters are similar, but with slightly higher velocities, especially towards the surface, during low water (a difference of about 0.03 ms^{-1}). Shear in the velocity profiles indicates strong turbulence that enhances dissipation of kinetic energy and represents some degree of turbulent mixing (Osalsusi *et al.*, 2009).

It is observed from Figure 17 that while the low and high water mean profiles exhibit similar trends, the profiles corresponding to flood and ebb are distinctly different not only in the shape of the respective profiles but also in the value of mean velocities with depth. Specifically, there is a greater reduction in velocity during ebb compared with flood tide.

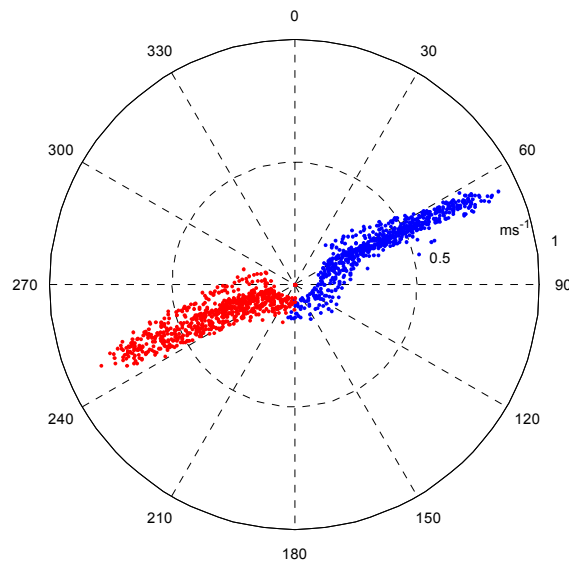


Figure 15: 10-minute time-averaged current velocity magnitude and direction: flood (blue) and ebb (red).

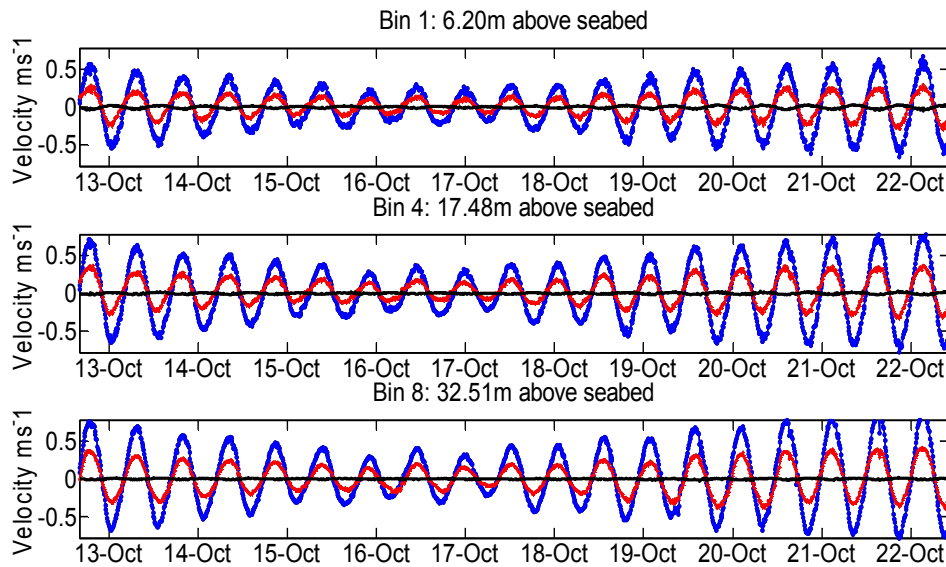


Figure 16: 10-minute averaged time histories of the u (blue), v (red) and w (black) components during the deployment period at three bin locations through the water column.

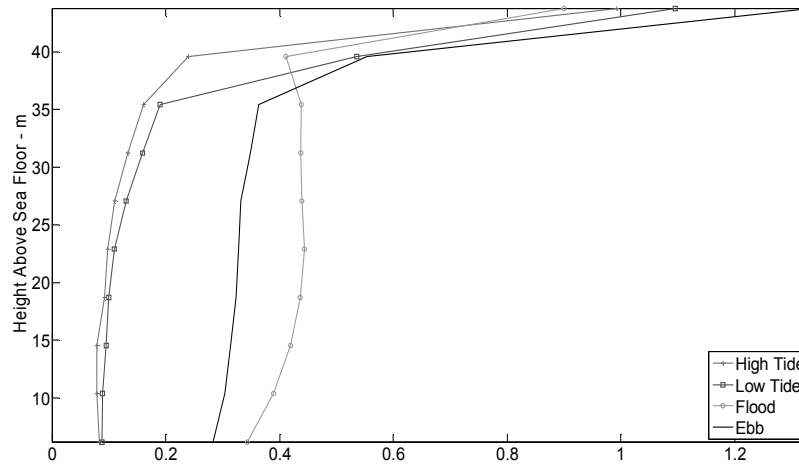


Figure 17: 10-minute time-averaged current velocity profiles over a tidal cycle.

3.2 Numerical modelling

A high resolution regional SWAN model was established with the aim of creating a dataset for the Isles of Scilly region and the Wave Hub and FaBTest development areas over a 23-year period. This section of the report details the model set-up, validation studies and a sub-set of the results.

3.2.1 Model set-up

The model domain was set up to cover the area of 4 to 7 degrees west and 49 to 51 degrees north, comprising the whole Cornwall coast, including the Isles of Scilly, and part of the Devon coast, with a grid resolution of 1 km x 1 km. Higher resolution nests (100 m x 100 m) were established for nearshore areas of interest, i.e. the Wave Hub, FaBTest and Isles of Scilly

regions. The model bathymetry used, constructed from Marine Digimap datasets, is illustrated in Figure 18.

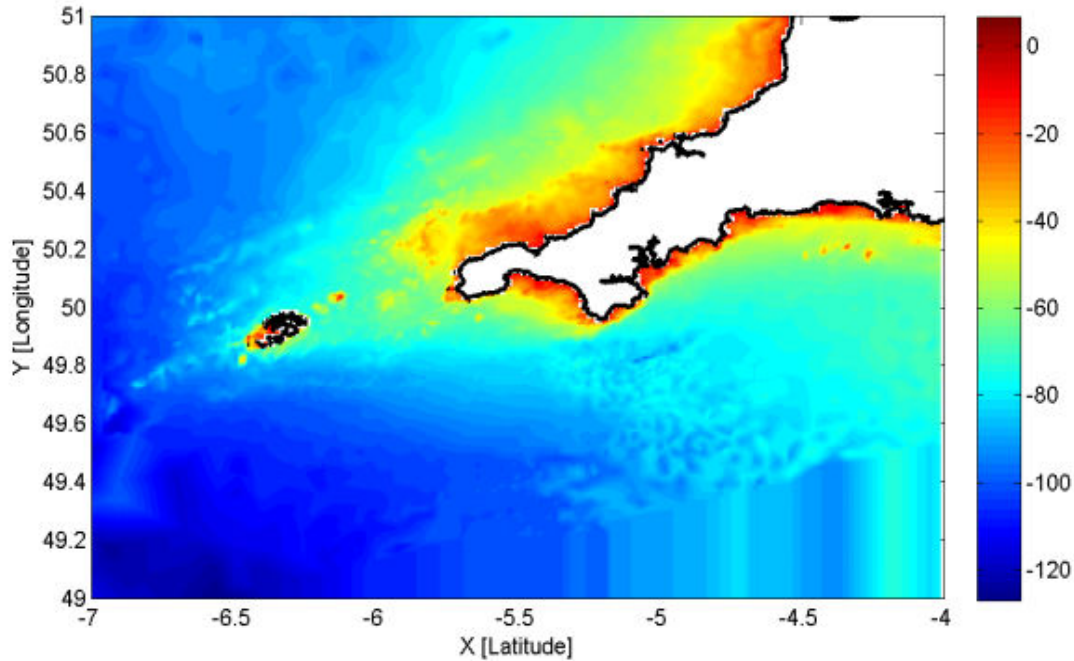


Figure 18: Bathymetry for the regional model domain.

Offshore data from the global model hindcast of ECMWF (European Centre for Medium-Range Weather Forecasting), which runs the global wave model WAM, were used as wave and wind boundary conditions. The grid resolution of the ECMWF model is 1.5 x 1.5 degrees and is therefore very coarse compared to the SWAN model resolution (Figure 19), while the temporal resolution is 6 hours. The wave parameters significant wave height (H_{m0}), peak period (T_p) and wave direction, plus the wind velocity and wind direction were acquired from ECMWF, and the wave parameters interpolated to the SWAN model corner points. The ECMWF wind data were interpolated to the SWAN model grid by SWAN itself. No water level variations and currents are taken into account.

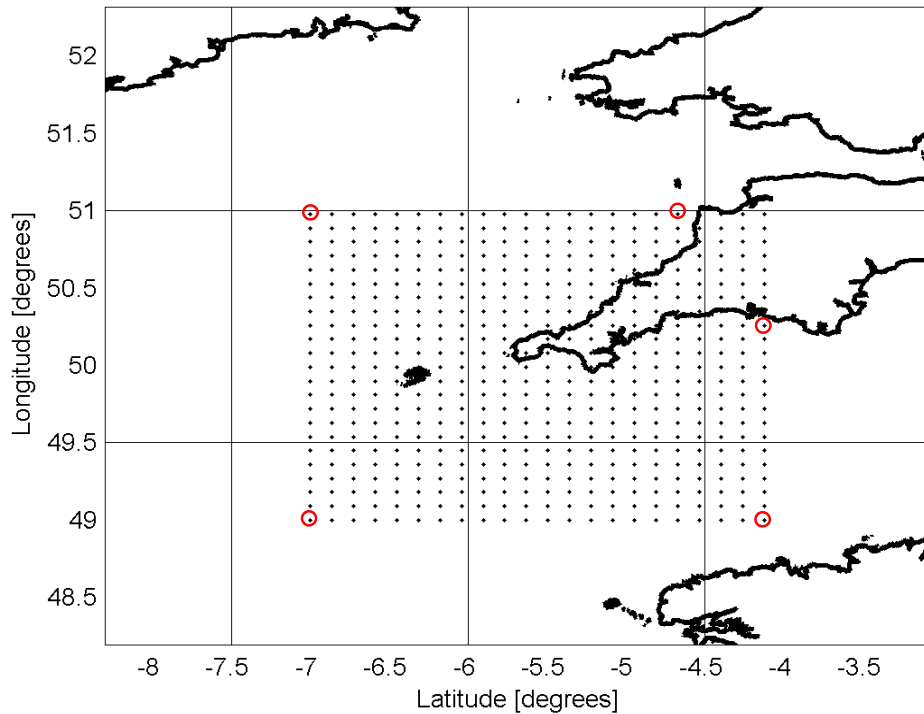


Figure 19: ECMWF model grid (0.5° squares) and every 10th grid line of the SWAN grid (black dots), with interpolated wave boundary input points (red circles).

SWAN default parameterisations for wind, nonlinear quadruplet wave interactions, bottom friction dissipation, depth-induced breaking and triad wave-wave interactions were used. For whitecapping, the formulation proposed by Rogers (2003) was applied. The weighting of the relative wavenumber term in the whitecapping formulation was altered ($n = 2$ instead of $n = 1$). Increasing n reduces the dissipation at lower frequencies and increases it at higher frequencies compared to the default SWAN settings.

Output was generated at various points across the model grid, and validated against buoy data at a number of locations (described in Section 3.2.2). The output points relevant to this study are shown in Figure 20 with the green squares indicating the validation locations. The hindcast was run over the period 1st January 1989 to 1st November 2011 with a time step of 60 minutes and a directional bin size of 8° to provide a sufficiently fine resolution for swell waves. For the spectral resolution, a range of 0.03 – 0.6 Hz was used, resulting in 31 bins. SWAN version 40.81 was used for the model computations, run on a Beowulf cluster.

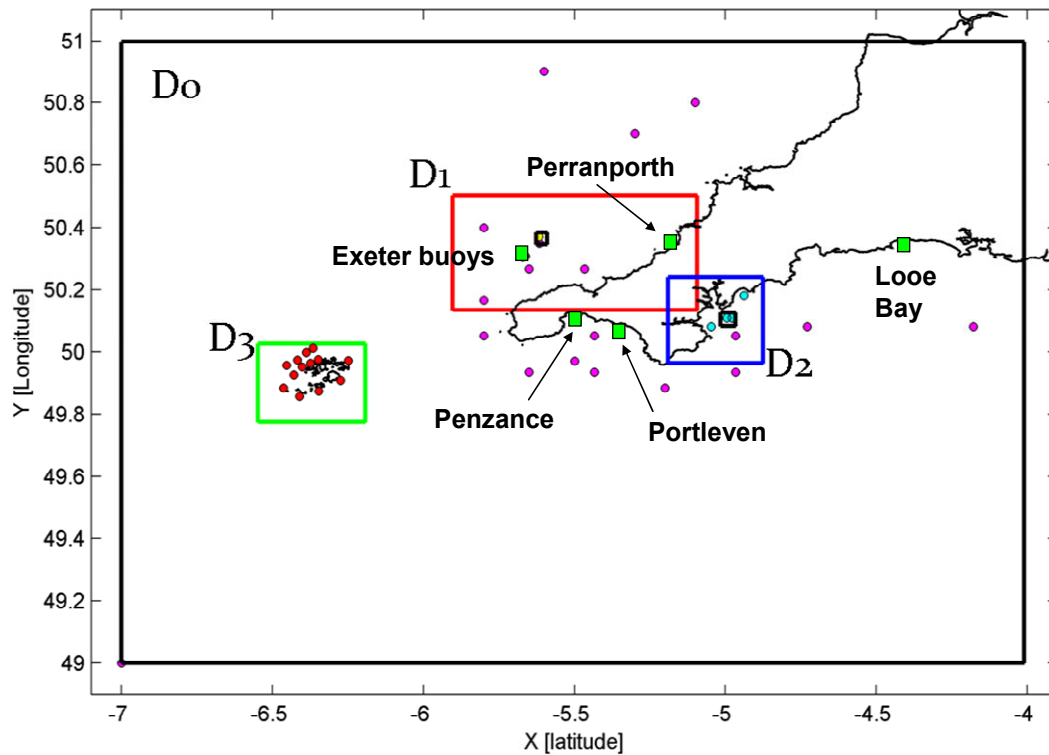


Figure 20: The 1km resolution model domain (D_0) and 100m resolution nested grids (D_1 , D_2 , D_3). The Wave Hub and FaBTest sites are shown as black squares, the coloured circles show detailed model output locations (yellow – north coast measurement location, blue – south coast measurement location) and the green squares show validation locations.

3.2.2 Model validation

The model set-up was validated against buoy data from six different buoys over the time periods where data was available. The buoys include two of the Exeter wave buoys from the array (described in Section 3.1) and four buoys deployed by the Coastal Channel Observatory at Perranporth, Penzance, Porthleven and Looe Bay (see Figure 20). The statistical results of the comparison between the measurement data and model results are shown in

Table 9. For each dataset the bias, the relative bias, the root mean square error (RMSE) and the scatter index, SI (the root mean square error normalized by the mean of observed values), have been calculated.

It can be seen that the significant wave height is generally underestimated by a few centimetres by SWAN. Comparisons between model and measurement data reveal a root mean square error in the order of 0.3 m. This means that the scatter index is approximately 20% for the northerly locations. Penzance and Looe Bay have a relatively high scatter index due to the fact that average wave height is lower at these locations. These buoys are relatively close to the shore and in shallow water and therefore errors are more likely because of wind input errors on the land-sea boundary, shallow water processes and wave-current interactions.

The wave period is also underestimated. In general, less underestimation of the wave period can be seen for south coast locations than for north coast locations. The scatter index varies between 20 and 30% depending on the location.

Table 9: Wave model validation statistics.

Buoy name	H_{m0}					$T_{m-1,0}$				
	N	Bias (m)	R. bias (%)	RMSE (m)	SI (%)	N	Bias (s)	R. bias (%)	RMSE (s)	SI (%)
Exeter A	5006	-0.08	-4	0.29	17	5006	-1.4	-18	1.9	24
Exeter D	7050	-0.05	-3	0.32	17	7050	-1.2	-15	1.6	20
Perranporth	40003	-0.06	-4	0.28	19	40003	-1.6	-20	2.2	27
Penzance	38562	-0.09	-15	0.19	32	38562	-1.1	-17	2.2	35
Porthleven	363	-0.01	-1	0.27	19	363	-0.5	-7	1.0	13
Looe Bay	19159	0.05	6	0.20	24	19159	-0.5	-9	1.7	28

Figure 21 shows the comparison between the measured and computed datasets for Exeter wave buoy D. The results illustrate that the performance of the model compared to the measurements is best for medium range wave heights between 0.5 and 3 meters. Above and below these levels the wave height is often underestimated by the model. It can be seen that the wave period is almost consistently underestimated by the model at the Exeter wave buoy D, although the computed wave direction compares in general relatively well to the measurements.

A more detailed overview of the validation process is presented in Appendix C.

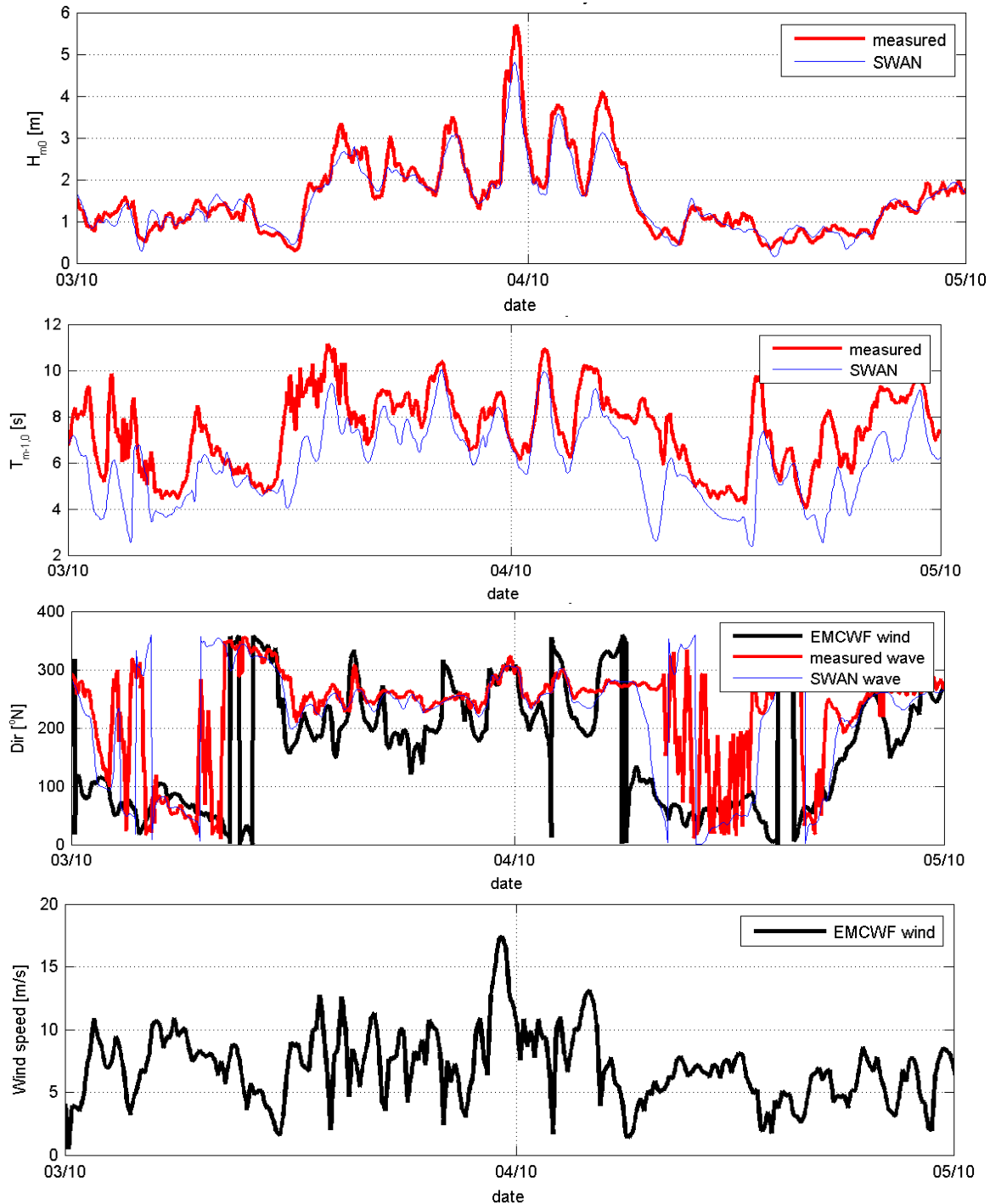


Figure 21: Time series comparison of computed and measured data for Exeter wave buoy D.

3.2.3 23-year hindcast results: Regional

Wave parameters, including significant wave height and mean period, were output at every grid point across the model domain, allowing maps showing the variability of the parameter

with space and time to be produced, e.g. Figure 22. By averaging the values at each grid point over a specific period of time, maps can also be produced to show average parameter values, e.g. seasonal or annual. Figure 23 shows the mean power across the region for the entire hindcast period. Power, P , is usually calculated from spectral data, using

$$P = \rho g \int S(f) c_g(f) df \quad \text{Equation 3}$$

where ρ is the water density, g is acceleration due to gravity, $S(f)$ the spectral variance density (in m^2/Hz) as a function of frequency f , and c_g is the wave group velocity. However due to data storage availability, output spectral data was not stored for every grid point within the model, only parameters. An approximation was therefore used to calculate the wave power:

$$P = \rho g H_{m0}^2 c_{gm-10} \quad \text{Equation 4}$$

where c_{gm-10} is the 'energy' group velocity, calculated from the energy period T_{m-10} and the wavelength found using T_{m-10} .

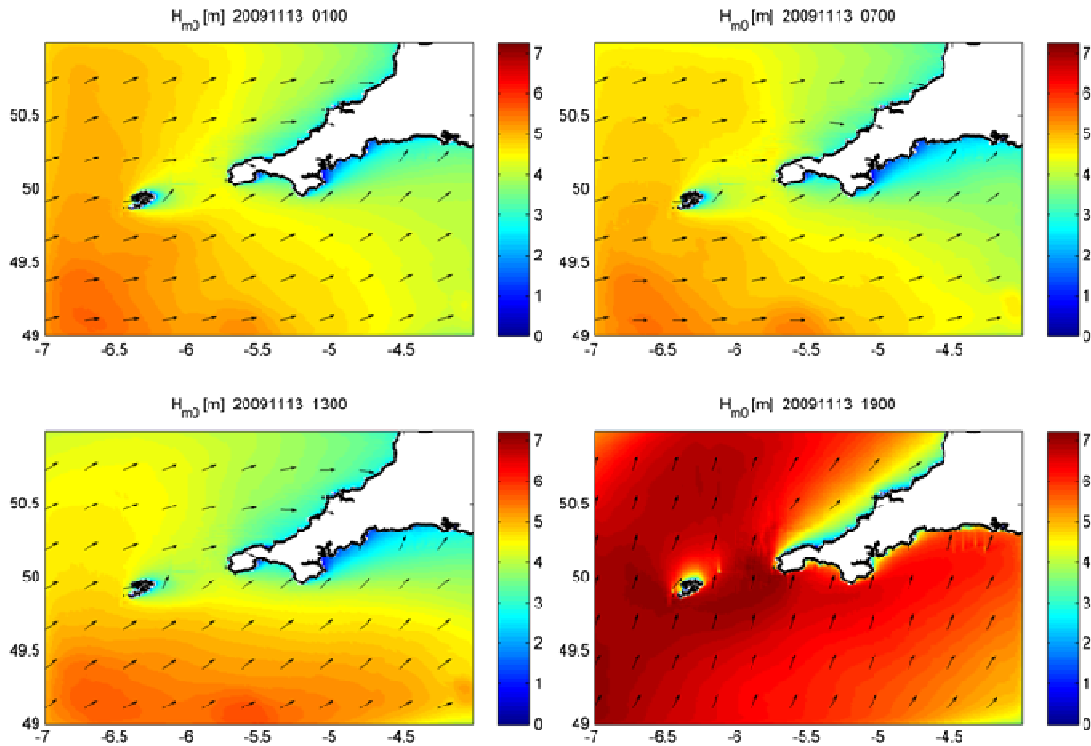


Figure 22: Spatial maps of H_{m0} showing the increasing wave height across the region over an 18 hr period in November 2009.

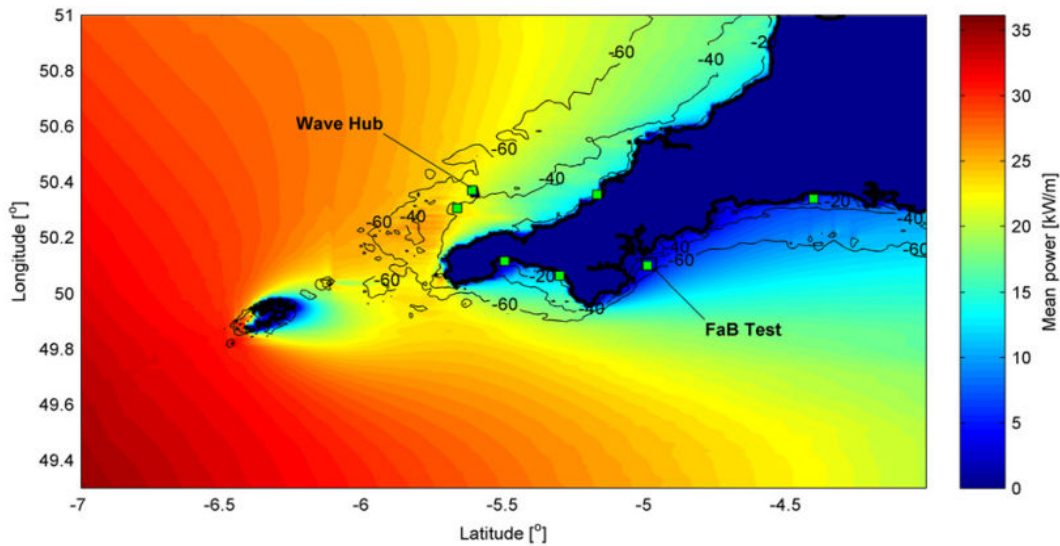


Figure 23: Mean power in kW/m across the region for the 23-year hindcast period.

3.2.4 23-year hindcast results: Site specific

In addition to providing output across the region, the 22-year hindcast also provided more detailed data for specific sites of interest. These include the Wave Hub and FaBTest sites and locations around the Isles of Scilly. This section presents a series of results for the Wave Hub, as an example of the data that is available for the other locations, in the following formats:

- Time series of wave power, H_{m0} and T_{m-10}
- Joint probability plot of H_{m0} and T_{m-10}
- Temporal power variability
- Directional power variability
- Spectral variation

Time series

Figure 24 shows the 23-year time series for wave power, H_{m0} and T_{m-10} at Wave Hub, along with the mean value for each parameter over the 23 years. The mean power at Wave Hub was found to be 20 kW/m, in agreement with values calculated from the measurement data described in Section 3.1.

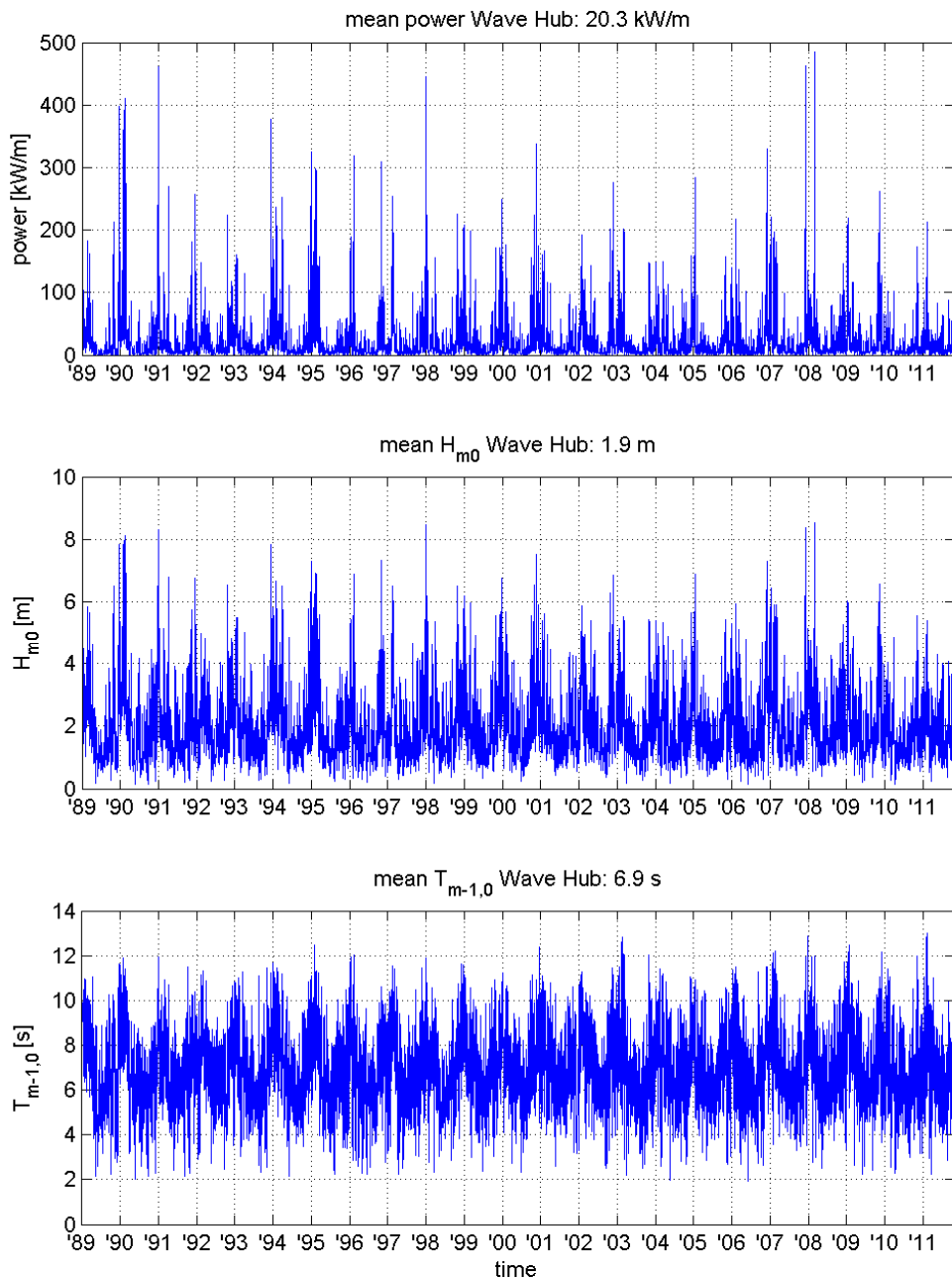


Figure 24: Time series of power, H_{m0} and T_{m-10} at Wave Hub.

Joint probability distribution

The joint probabilities of occurrence for H_{m0} and T_{m-10} at Wave Hub are shown in Figure 25. Every square shows the percentage occurrence of the combination of H_{m0} and T_{m-10} . It can be seen that the most frequently occurring sea states have a wave height of approximately 1-2 meters and a wave period of 4-7 seconds.

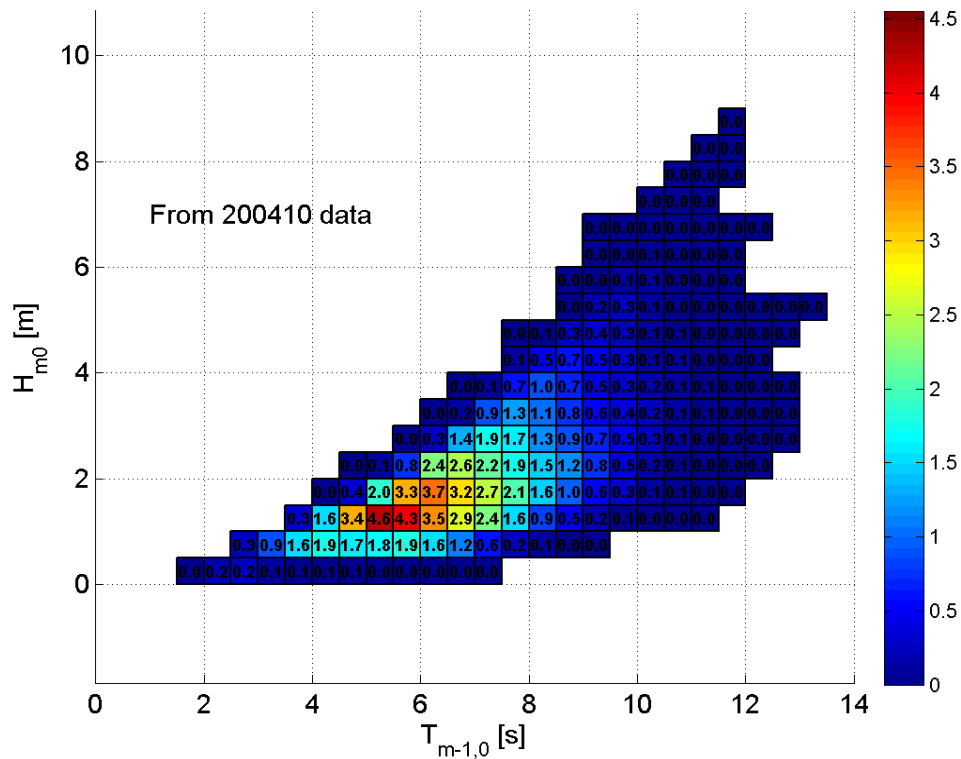


Figure 25: Joint probability distribution for H_{m0} and $T_{m-1,0}$ at Wave Hub.

Temporal variability

Figure 26, Figure 27 and Figure 28 show the annual and monthly variation in wave power, H_{m0} and $T_{m-1,0}$ at the Wave Hub site. In addition Figure 29 presents the seasonal power variation, for which each year of the dataset was divided into spring (March, April, May), summer (June, July, August), autumn (September, October, November) and winter (December, January, February) datasets, and the mean power calculated. The variation in power levels over each year is substantial, with average monthly power levels over 50 kW/m in some winter months, compared with frequent monthly averages below 10 kW/m in the summer months. The figure in the mid panel suggests an overall trend of decreasing power levels. Averaged over the whole dataset, it can be seen that December, January and February are the most energetic months with mean power levels up to 40 kW/m. Wave heights vary from 1.3 meter in summer to 2.8 meter in winter. Wave periods vary from 6 seconds in summer to 9 seconds in winter.

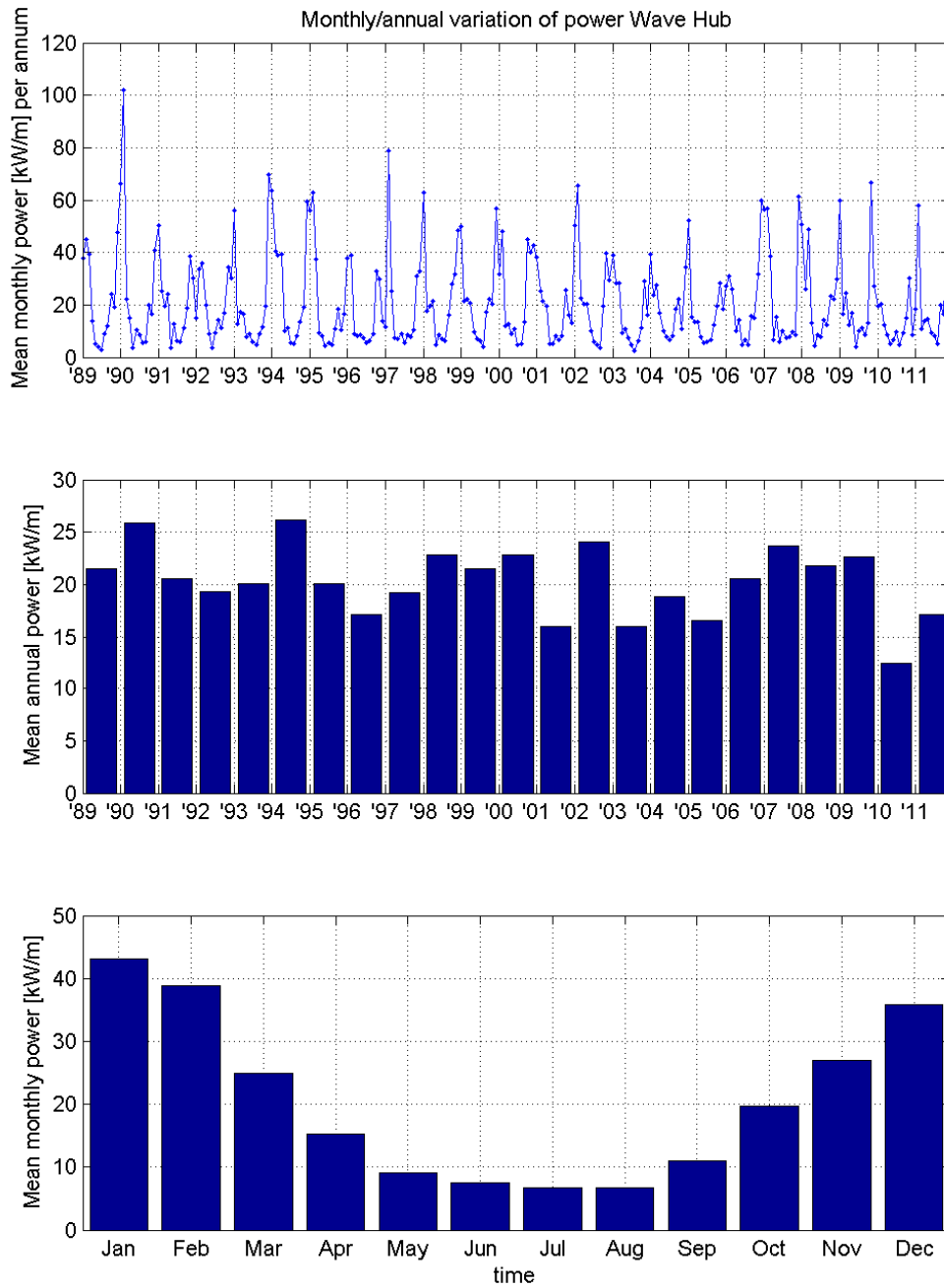


Figure 26: Monthly/annual variation of power at Wave Hub.

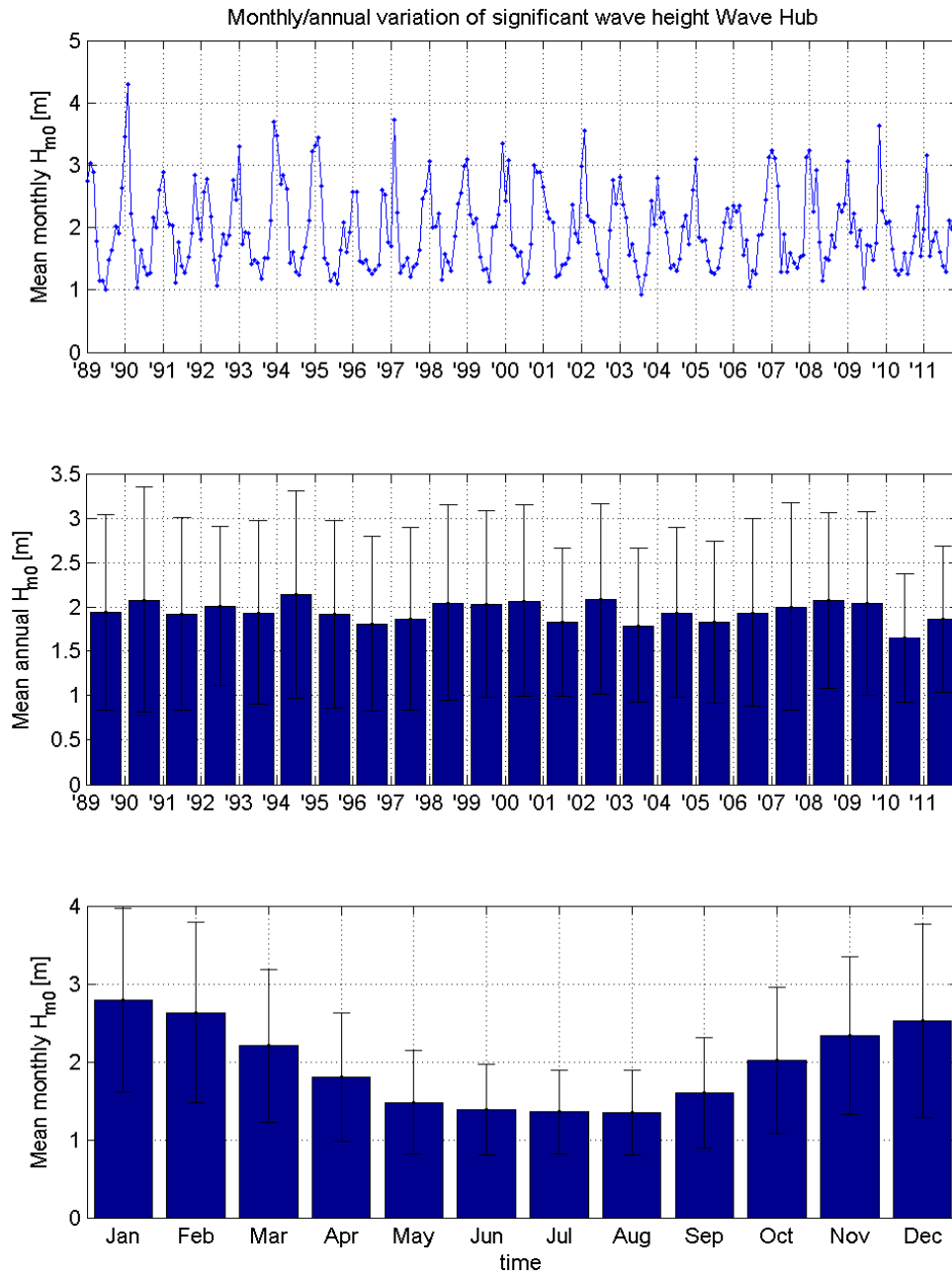


Figure 27: Monthly/annual variation of H_{m0} at Wave Hub, with bars showing the standard deviation in the data.

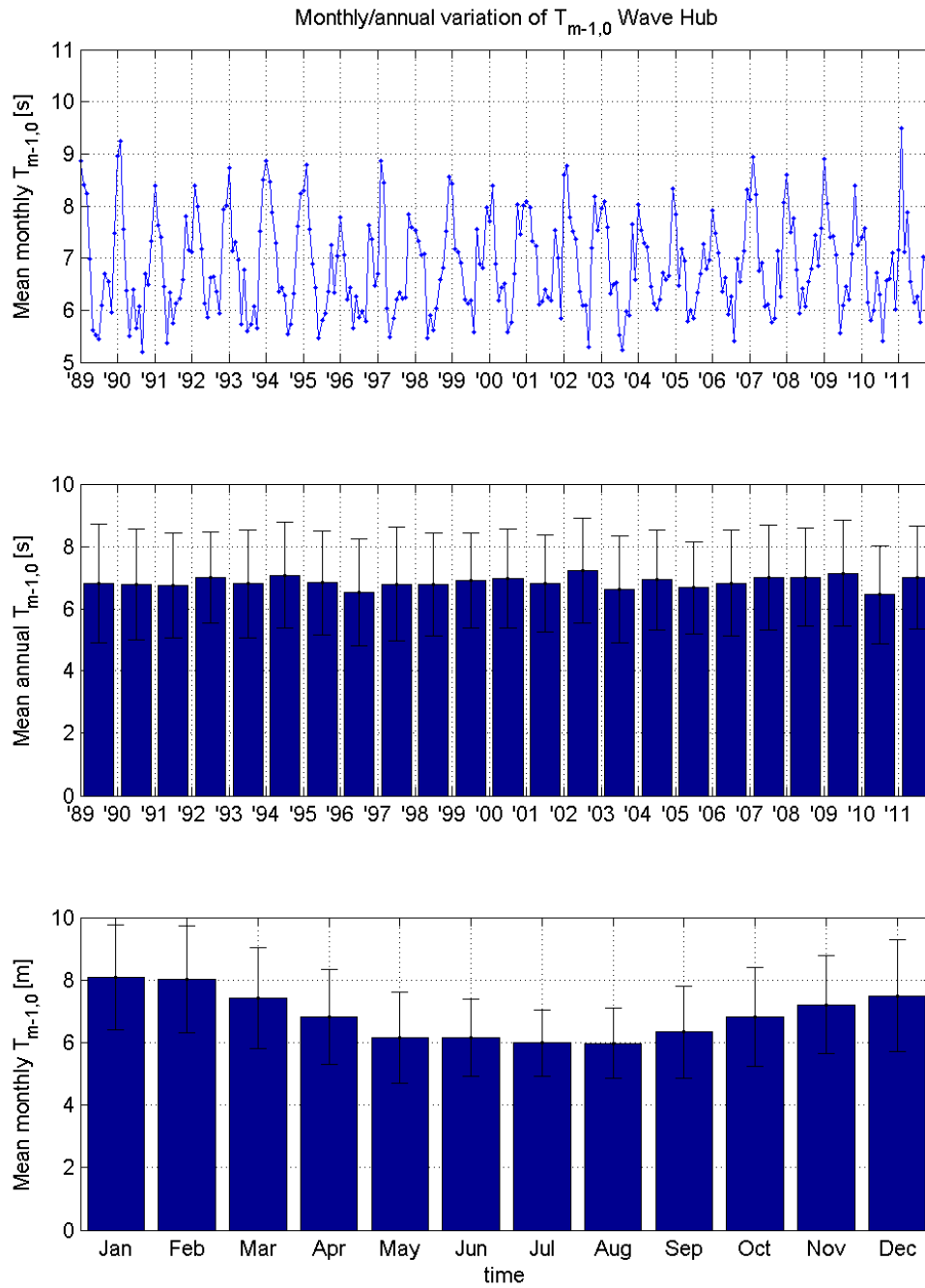


Figure 28: Monthly/annual variation of $T_{m-1,0}$ at Wave Hub, with bars showing the standard deviation in the data.

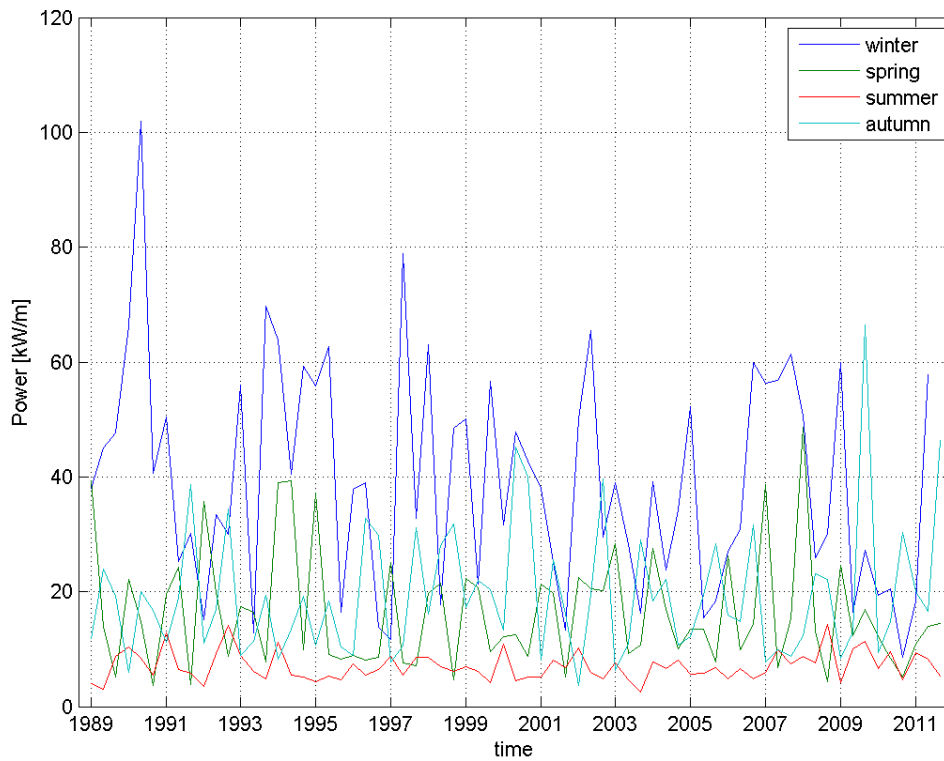


Figure 29: Seasonal variation of power at Wave Hub.

Directional variability

Figure 30 shows the directional wave power variation. The left-hand figure shows the occurrence of wave power below 50 kW/m and the right-hand figure shows the occurrence of wave power above 50 kW/m. It can be seen that most wave energy comes from the west and in addition the most energetic waves come from the west.

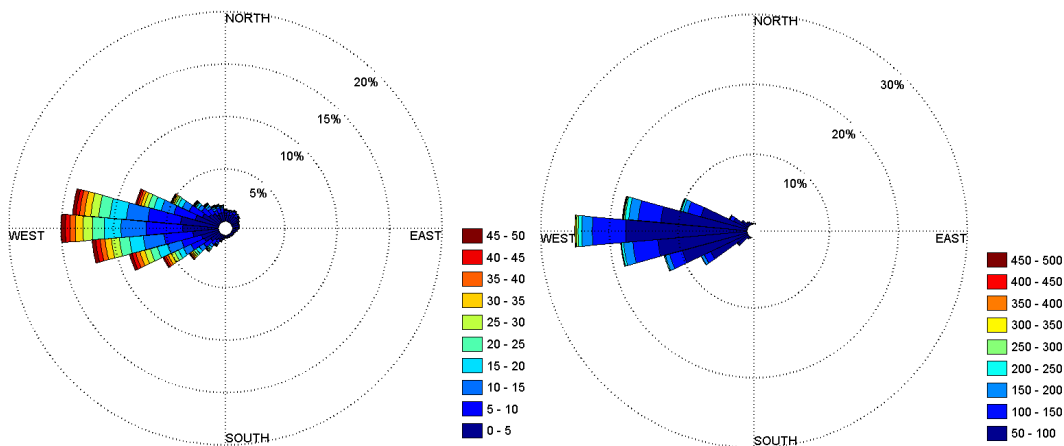


Figure 30: Wave rose for wave power [kW/m] at location 1, left-hand figure for power < 50 kW/m, right-hand figure for power > 50 kW/m.

Figure 31 shows the mean wave power binned by wave direction. The mean wave power is largest for wave directions between 240 and 300° North, with respectively 26 kW/m and 24 kW/m for the 240-270 and 270-300° bins. The joint probability between H_{m0} and $T_{m-1,0}$ is shown for these bins in Figure 32 and Figure 33. These show that the most frequently occurring waves for westerly wave directions are larger than the most frequently occurring waves in the joint probability plot considering all directions (Figure 25).

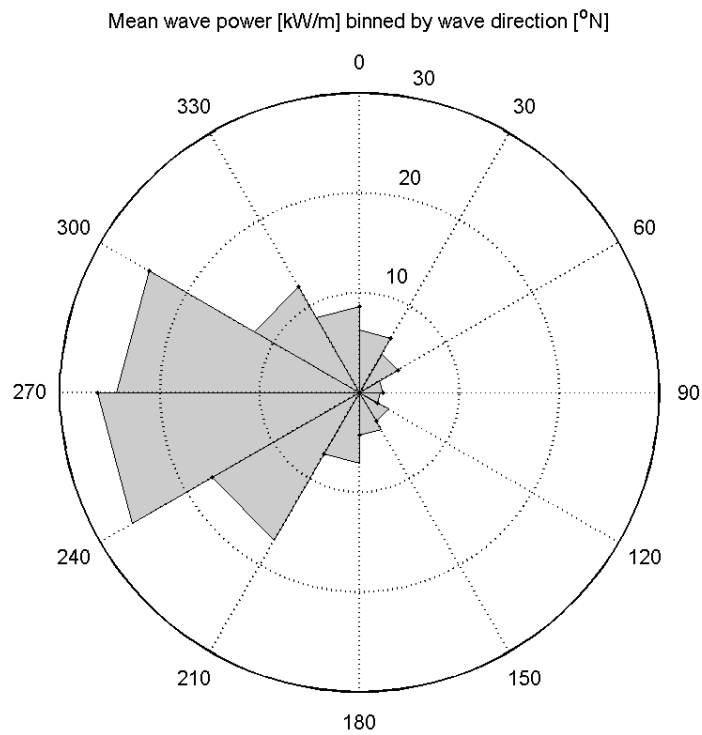


Figure 31: Mean wave power (kW/m) binned by wave direction (°N) in 30 degree bins.

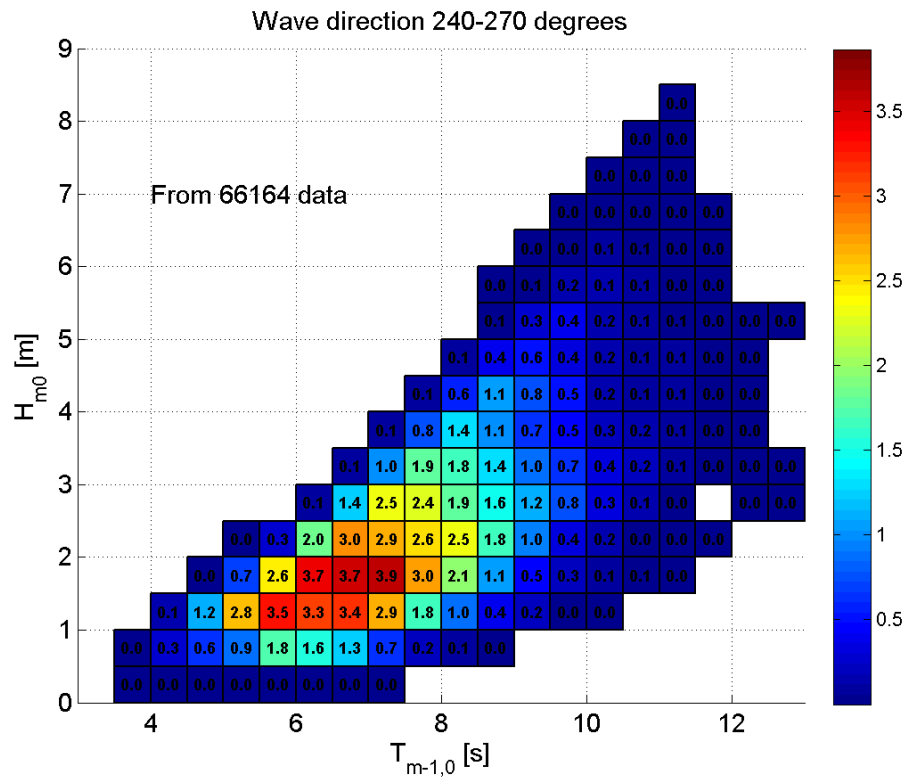


Figure 32: Joint probability H_{m0} and $T_{m-1,0}$ for wave direction bin 240-270°.

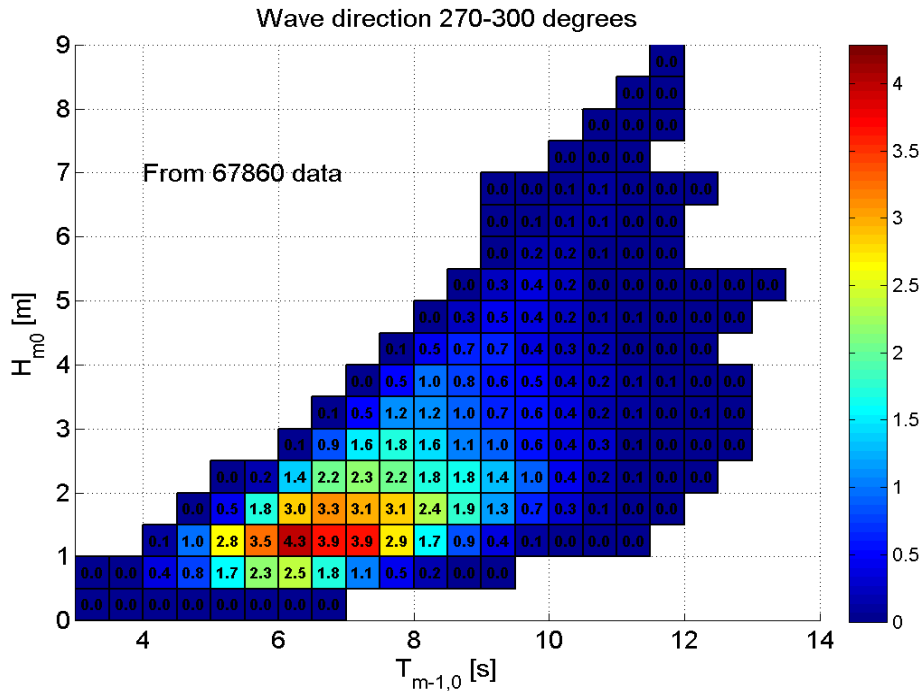


Figure 33: Joint probability H_{m0} and $T_{m-1,0}$ for wave direction bin 270-300°.

Spectral variation

Figure 34 presents spectral data in a scatter diagram format. For each bin of the scatter diagram, all spectra with parameters that fall within the bin limits are plotted and the mean spectrum for the bin is calculated. The figure indicates that bi-model sea states are common occurrences for the smaller seas.

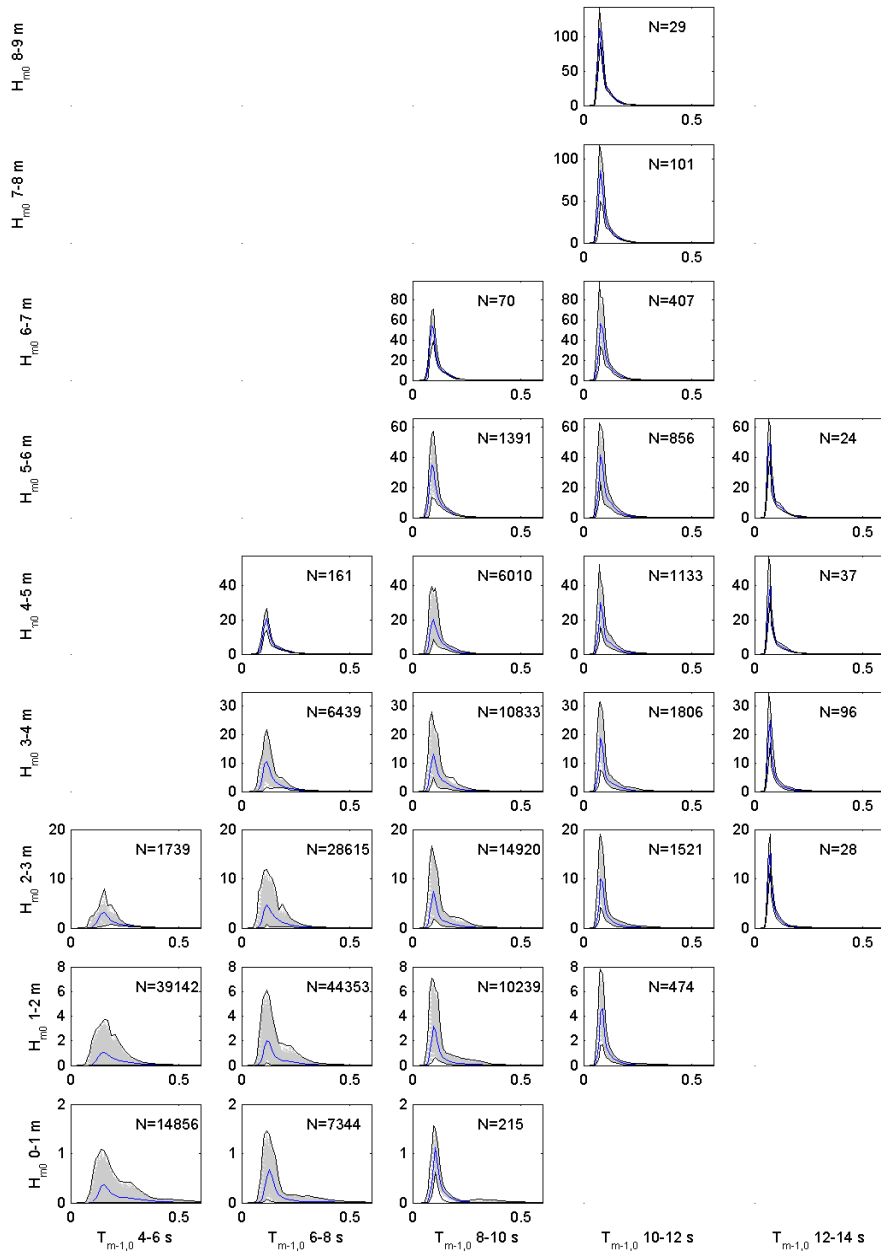


Figure 34: Spectral variation, with frequency [Hz] on the x-axis and energy density [m^2/Hz] on the y-axis.

4 Resource assessment for the Iroise Sea

The Iroise sea is the area located in the north of the Bay of Biscay, at the entrance to the Channel, off the coast of Finistère, Brittany, France. It extends from the north of Ouessant Island and the Molène archipelago to the south of Sein Island and Penmarc'h cape, and in the west to the limit of the territorial waters. It can be noted that Parc National Marin d'Iroise is included in the Iroise Sea.

In spite of heavy marine traffic as well as fishing and recreational activities, many locations have been identified in the Iroise Sea that are thought to be suitable for extraction of marine renewable energy. For instance, previous studies showed that the yearly average wave power in this area can reach up to 45 kW/m, which makes it one of the most energetic wave sites in Europe (Figure 35). Additionally, the area is subject to tides with a large tidal range inducing flows with high velocities in specific locations. In particular, the Fromveur strait in the Molène archipelago, south of Ouessant Island, is subject to currents with velocities up to $\sim 4\text{m/s}$ and has been identified as a potential site for deployment of tidal turbines.

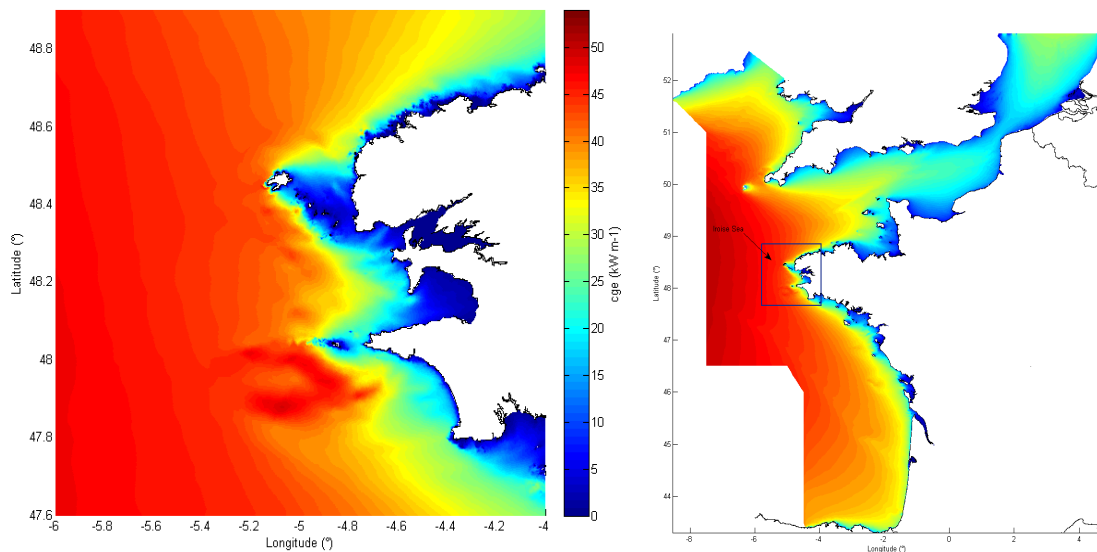


Figure 35: Location map showing the extent of the Iroise Sea (left) and its relationship to the full numerical model domain (right).

This chapter presents a detailed characterisation of the climatology of the Iroise Sea, mostly based on analysis of a specific hindcast database developed for that purpose, providing assessment of the wave and tidal resource and its variability in time and space.

4.1 Measured data

In-situ measurement databases suitable for resource assessment in the Iroise Sea are limited due to the lack of specific projects to deploy MRE devices in this area to date. Nevertheless, the Iroise Sea has been monitored for years and in-situ and remote measurement databases are available that can be of interest, mostly for validation of dedicated forecast/hindcast models.

4.1.1 Wave data

The main source of measured wave data available for the Iroise Sea is the measurement data provided by the wave buoy referenced 02911/62069 (named "Les Pierres Noires") operated by CEREMA¹ since 2005 and part of the PREVIMER² service (see figure 36). This Datowell Waverider buoy is moored at the point with coordinates 048°17.420'N, 004°58.100'W, in approximately 60 m water depth. It provides spectral information every half hour, from which a large set of wave parameters relevant to resource assessment can be derived. Those include significant wave height, mean and peak periods as well as mean and peak directions. Data is available through the CANDHIS³ archiving service. Other data sets are also available from this service but most of them correspond to short duration surveys and would not be suitable for a proper resource assessment. The buoy 02902 "Ouessant Large", moored at the point with coordinates 048°30.00'N, 005°45.00'W, farther offshore in the west of the Iroise Sea, also offers relevant information for validation purpose as it extends over 16 years.

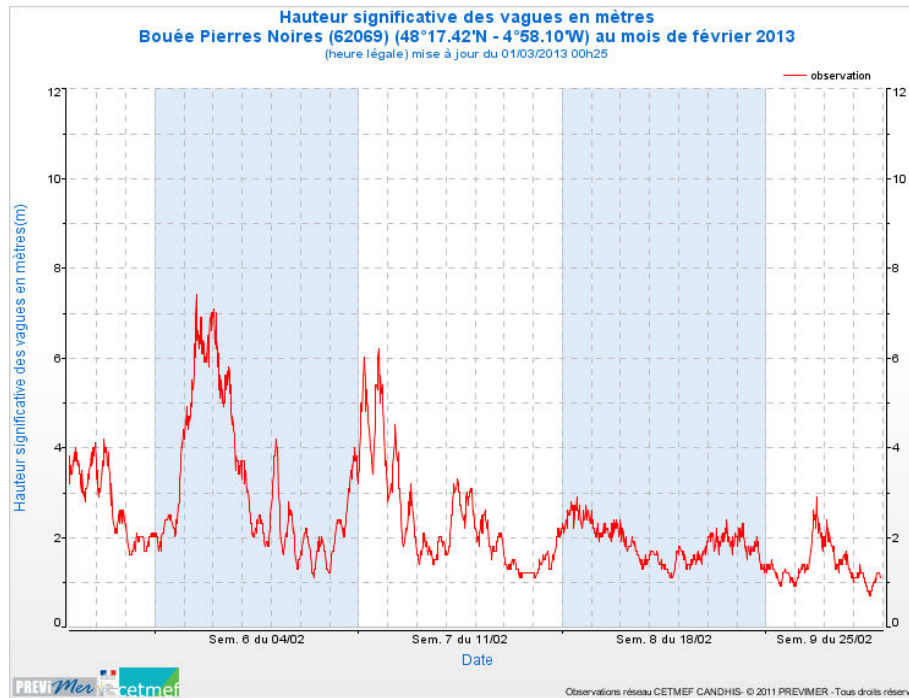


Figure 36: Example of a 62069 Wave Buoy Record - Significant Wave height February 2013.

4.1.2 Current data

Several tidal current surveys were conducted in the Iroise Sea areas during the last decades, involving deployment of ADCPs or Lagrangian drifters. The main purpose of these surveys was the validation of ocean models such as Mars 2D/3D or identification of specific local phenomena (Muller *et al.*, 2010). Hence, in-situ measurement data sets are limited and of too short a duration for a full assessment of the current resource.

¹ CEREMA : Centre d'Etudes et d'Expertise sur les Risques, l'Environnement, la mobilité et l'Aménagement.

² www.previmer.org

³ CANDHIS : Centre d'Archivage National de Données de Houle In-Situ (<http://candhis.cetmef.developpement-durable.fr>)

The main long-duration dataset available for the Iroise Sea is the one provided by the HF radars deployed along the coast and covering most of the area. These HF radars, owned by SHOM⁴ and operated by Actimar⁵ use the WERA technology (Helzel *et al.*, 2011). They were deployed in 2005 and allow measurement of surface currents over an area extending 150 km offshore, providing near real time data every 10 minutes.

A specific study on improvement of processing algorithms for current measurement using HF radar was conducted by Actimar as part of MERiFIC task 3.4. The report (MERiFIC deliverable 3.1.4 “Processing and Analysis of HF Radar Measurements of Currents and Sea States in the Iroise and Celtic Seas”) also provides some insight on the ocean and tidal current climatology in the Iroise Sea. An example of the output from the HF radars is shown in Figure 37.

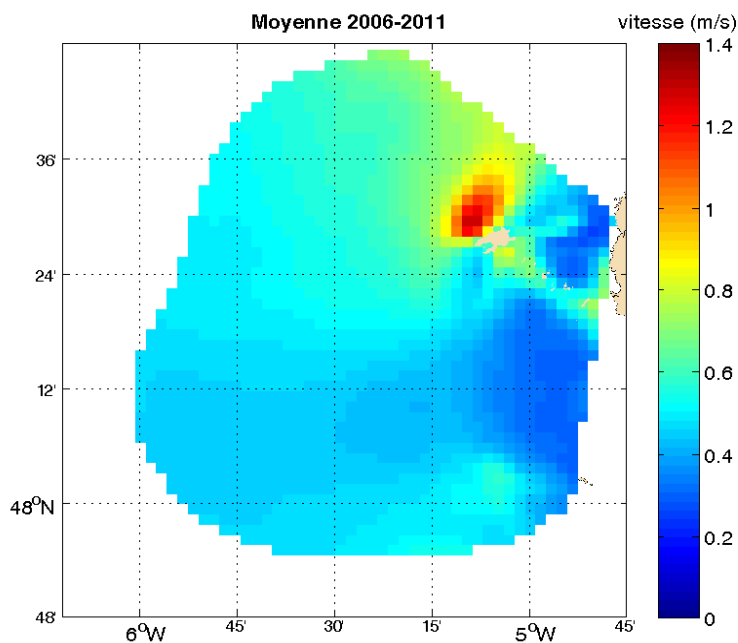


Figure 37: Mean surface current velocity amplitudes over the period 07/2006 - 08/2011.

4.2 Wave numerical modelling

Wave resource assessment in Iroise Sea was mostly based on analysis of a hindcast database built using a specific configuration of the WaveWatch III© (WW3) wave model.

4.2.1 Model set-up

Datasets were obtained running the WW3 code (see §2.2.1), version 4.09. An unstructured grid was built with a resolution ranging from 200 m to 10 km, adapted at various scales from the open sea to the shore (Boudière *et al.*, 2013). Even though the MERiFIC study focuses on the areas of the Iroise Sea and the southwest UK, it was decided to configure the model to cover a broader area. The full computational domain extends from the southern North Sea to northern Spain, covering the Channel and the whole continental shelf in the Bay of Biscay (see Figure 35). One benefit of having considered this larger area is the availability of data covering the area of the southwest UK modelled by the University of Exeter using the SWAN model. These

⁴ SHOM : Service Hydrographique et Océanographique de la Marine – www.shom.fr

⁵ Actimar Océanographie Opérationnelle – www.actimar.fr

two datasets are used for the cross-comparison of methods presented in MERiFIC deliverable 3.1.5 (“Cross-analysis of Resource Assessment Methods”).

The dataset extracted from this database for this specific resource assessment study in the Iroise Sea extends over the domain 004°00’W to 006°00’W, and 47°36.00’N, 48°54.00’N (Figure 38). Its total duration is 19 years (1994 – 2012) with a time step of one hour.

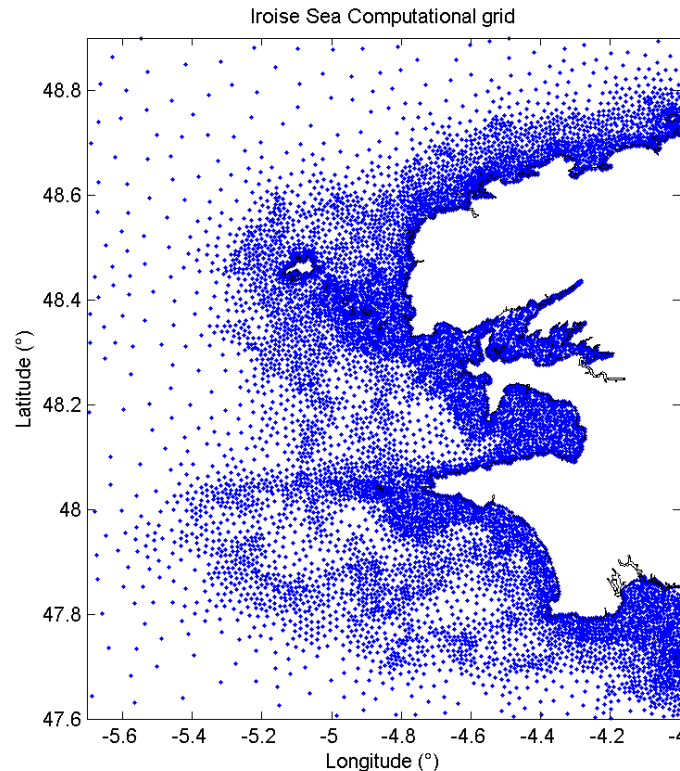


Figure 38: Iroise Sea wave model computational grid.

Bathymetry

The high resolution bathymetry used in this configuration combines the data from SHOM for the coastline and from surveys conducted by IFREMER and SHOM for the bathymetry (MNT 100 m and 500 m).

Forcing fields

The wave model is forced by the wind field from the CFSR reanalysis (Climate Forecast System Reanalysis (Saha *et al.*, 2010)) that was produced at NCEP (National Centre for the Environmental Prediction) in 2010. This 10 m wind field is a reanalysis over a 31 year period from 1979 to 2012, with a spatial resolution ranging from 0.25° at the equator to 0.5° at higher latitudes.

Water levels, surges and currents were computed using the MARS 2D hydrodynamic model, (see §2.2.2). In order to avoid the rather heavy handling of currents and water level data produced by the seven embedded models, the choice was made to build atlases of harmonic components. A hindcast was produced over a one year period (2008) and analysed to produce tide and tidal current harmonic component atlases for each of the seven models. Tides and tidal currents were then predicted for any period of time over the whole domain. The tidal constituents and water levels were updated with a 30 minutes time step and interpolated on the wave model grid with the finest resolution.

Output parameters

In total, a set of 37 global parameters were produced at each point of the computational grid (Boudière, 2014), including significant wave height H_s (m), peak period T_p (s), energy period $T_{m-1,0}$ (also written T_e) (s), wave directions at the peak frequency (D_p) and energy flux or power, $C_g E$ or P (kW/m), more specifically used in the present resource assessment study. Such a refined grid allows an accurate description of the variability of sea-states in space, of prime interest for resource assessment.

Marine energy devices will be deployed in high energy areas, where the environmental conditions are not necessarily the harshest but can vary in space and time and can often be complex with multi-modal sea-states, superposition of swell and wind seas and strong wave-current interaction. Directional spectra provide the most comprehensive information on the distribution of wave energy within a sea-state, and as such are of great use for resource assessment and description of climatologies, especially when spectral bandwidth and directional spreading are to be characterised. Saving all directional spectra at each node of the computational grid was simply not possible for practical reasons related to data handling and storage. Nevertheless, and with the objectives of the use and exploitation of this database in mind, a coarser output grid was created, derived from the original computational mesh, on which directional spectra were saved at each time step. This output grid was specifically designed so that locations of interest for wave energy assessment, such as the Wave Hub site for example, could be taken into account. At each point of this coarser grid, directional spectra (24-directions x 32-frequencies matrices) were saved with a one hour time step.

4.2.2 Model validation

An extensive validation programme was conducted using various datasets combining in-situ measurements from directional buoys, remote sensing from satellite altimeters and output from the NOAA/NCEP configuration of WW3 (even though the latter is not presented here as it is limited to deep and intermediate water depths outside the Iroise sea area).

In-situ datasets used for this validation include data from the CANDHIS buoys network operated by CEREMA as well as data from Météo-France buoys.

About 15 buoys were used for validation which proved the good agreement of the model with in-situ observation overall. Of major interest is of course the comparison with buoy 62069 located in the Iroise Sea (see §4.1.1) which shows a very good agreement with less than 5 cm of bias and an RMS error of approximately 13 cm (Figure 39).

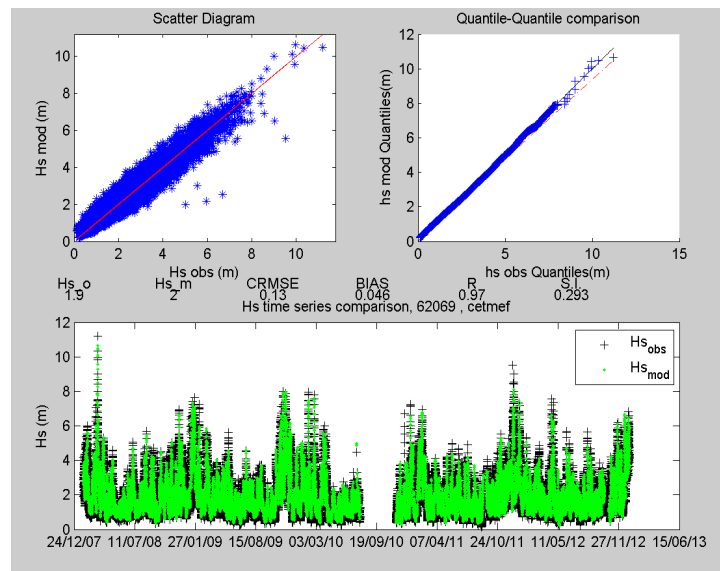


Figure 39: Model validation - Cross-comparison with buoy 62069.

Validation by cross-comparison with remote sensing data was conducted using the CERSAT⁶ database of wave and wind parameters from altimeters. This database includes the ENVISAT, ERS1/2, TOPEX, JASON1/2 and GFO altimeter data, pre-calibrated and corrected. Due to the high resolution of the global wave parameter output grid of the model, model output could be compared to the satellite data provided along the tracks of the altimeters over the whole domain. Validation was performed for the whole period of hindcast. The wave model has a one hour time step, thus, individual hindcast data points were interpolated in time onto the tracks of the altimeters. Again, comparison proved the model to be of good quality with a bias ranging between 2.9 % and 7 % depending on the altimeter, and RMS error smaller than 14 cm (Figure 40).

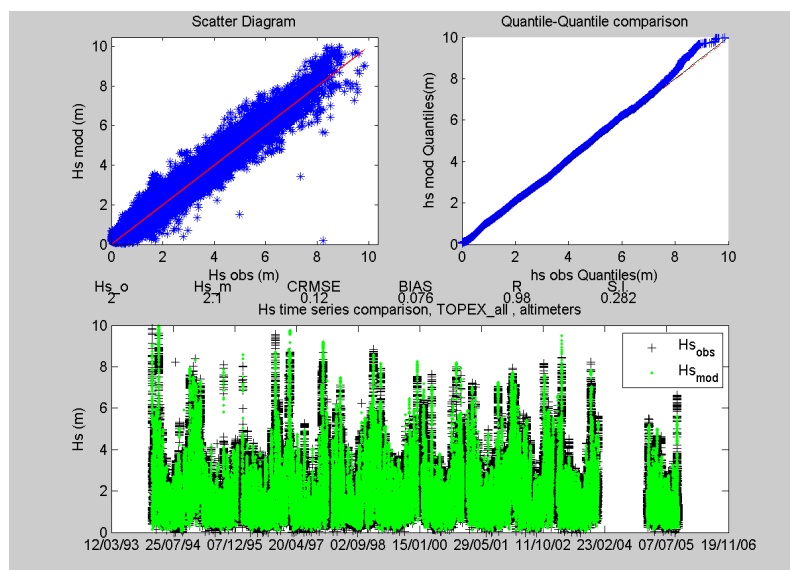


Figure 40: Model validation - Cross-comparison with Topex altimeter data.

⁶ CERSAT : <http://cersat.ifremer.fr/>

With the availability of this validated and refined hindcast database, it was possible to conduct an extensive resource assessment at both a regional and a site-specific level.

4.2.3 19-year hindcast results: Regional

The domain considered for this resource assessment study in the Iroise Sea extends over the domain delimited by longitudes 004°00'W to 006°00'W and latitudes 47°36.00'N to 48°54.00'N. The total duration of the time series is 19 years (1994 – 2012) with a one hour time step.

Parameters considered for this regional study include:

- Significant wave height H_s (m)
- Energy period $T_{m-1,0}$ (or T_e) (s).
- Peak direction D_p (°)
- Power (energy flux) $C_g E$ (or P) (kW/m).

Yearly means of each of these four parameters computed over the 19 years are plotted in Figure 41 and provide an overview of the regional climatology:

Significant wave height varies from approximately 2.6 m in deep waters to the west and 2.5 m over most of the area to very low values, below 1 m, in coastal areas and bays. Also clearly visible is the shadowing effect induced by Ouessant Island and the Molène archipelago in the north and Sein Island in the south.

Energy period is on average approximately 9 s, reducing to ~7 s to the east of the Molène archipelago, the sheltered bay of Douarnenez and the south-east of Penmarch cape.

The direction of propagation of sea states is predominantly from the west to north-west sector, except along the southern coasts where the southwesterly direction dominates because of both refraction and the masking effect of the shore. Specific features can be observed, for example if waves enter the Fromveur strait between Ouessant and Molène Islands from the south-west, wave direction to the north of Molène island is predominantly north-west to north because of the long swell systems travelling around Ouessant's north coast. A gradient of direction is also noticeable in the Audierne bay, shifting from west to south along the coast from the south of the bay to its northern perimeter.

Finally, the wave power appears relatively consistent over the western part of the area with an average value ~45 kW/m and then rapidly decays as the waves propagate towards the coastal areas in the east. Clearly visible again is the blocking effect induced by the Molène archipelago. A small area south west of Sein Island can be seen, where the power reaches higher values of around 50 kW/m.

These general features are in agreement with the well known climatology of the north of the bay of Biscay, dominated by westerly (north-west to south-west) sea states generated by the low pressure systems travelling from west to east in the northern Atlantic.

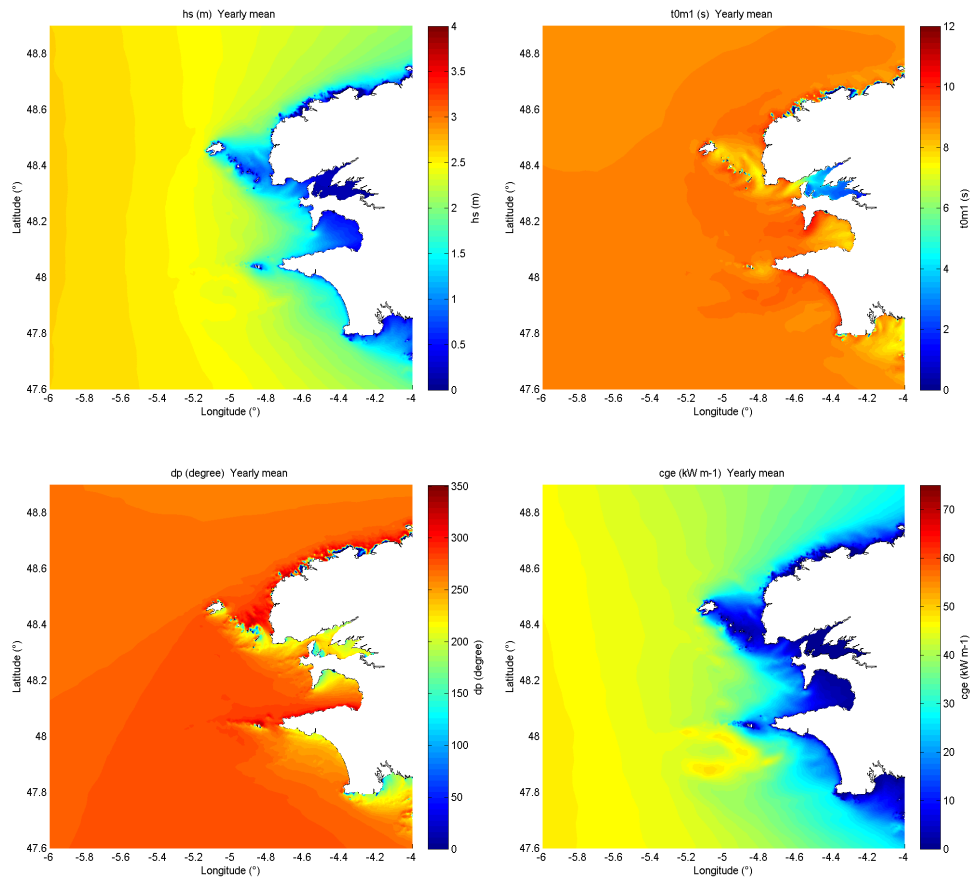


Figure 41: Annual mean global parameters for the Iroise Sea (H_s (m), $T_{m-1,0}$ (s), D_p (°), $C_g E$ (kW/m).

Similar regional maps of the monthly average values of these four parameters are presented in Appendix B. The general features of the evolution in space of the parameters observed in the annual mean maps are clearly visible, however, the key characteristic that can be observed in the monthly mean maps is the seasonal variability.

January is the most energetic month with an average significant wave height of ~ 3.8 m offshore to the west of the region. A “winter” season can be clearly identified lasting over the months of November to February, during which average significant wave height off-shore is above 3m. Monthly average energy periods during that season are around 10 s, so the average power is above 80 kW/m with values above 100 kW/m in January.

A “summer” season with mild sea states can also be identified over the period from May to August. Average significant wave height during that time is globally below 2 m and the associated averaged energy periods are around 8 s. Hence, the average power is reduced to values below 20 kW/m.

“Intermediate” seasons March-April and September-October, are periods of transition between these two main seasons. Average significant wave height is around 2.5 m while the energy period takes values around 9 s.

The magnitude of this seasonal variability, especially in terms of available power, is of prime importance for the management and planning of marine energy plants. If the global trend of

this variability can be considered to correlate well with electricity consumption (RTE, 2013), marked by a higher demand in winter, it can significantly affect the design, management of operations and maintenance of a plant. This point will be discussed in more detail in the following section where two specific sites are studied.

4.2.4 19-year hindcast results: Site specific

Bearing in mind the general trends of the regional wave climatology, we now focus on two specific sites so as to provide a more detailed insight on the local resource and its variability.

As there are no existing test sites or production plants at present in the Iroise Sea, two locations were selected which can be considered representative of possible sites to be investigated for the deployment of wave energy systems.

The first site considered here is located offshore, to the western extent of the Iroise Sea in deeper, unsheltered waters (water depth ~ 118 m) where wave power is higher. Coordinates of the reference point, labelled I5 (see Merific deliverable 3.6.2, “Best practice report - Installation Procedures”), are $48^{\circ}18.00'N$, $5^{\circ}42.00'W$.

The second site was chosen closer to the shore, in the south of Audierne bay (see Figure 42) so as to provide an insight on available resource in more sheltered locations where deployment of wave energy plants could still be considered in spite of a lesser available power. Coordinates of the reference point, labelled I7 (see Merific D.3.6.2), are $47^{\circ}52.02'N$, $4^{\circ}25.638'W$, with water depth ~ 38 m.

The northern part of the domain was disregarded when selecting sites because of the heavy marine traffic at the entrance to the Channel, and areas in the east of the Molène archipelago and Douarnenez Bay were not considered because of the limited available power.

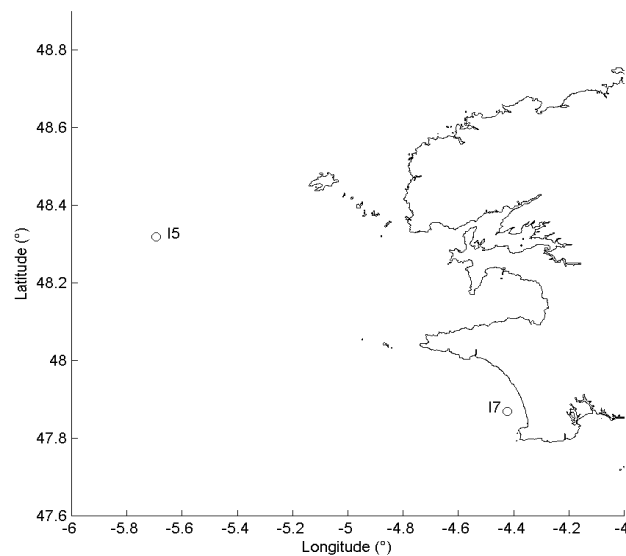


Figure 42: Reference sites for the site-specific study.

Site I5

Statistics for the main sea state parameters H_s , $T_{m-1,0}$, $C_g E$ and D_p are presented in Figure 43.

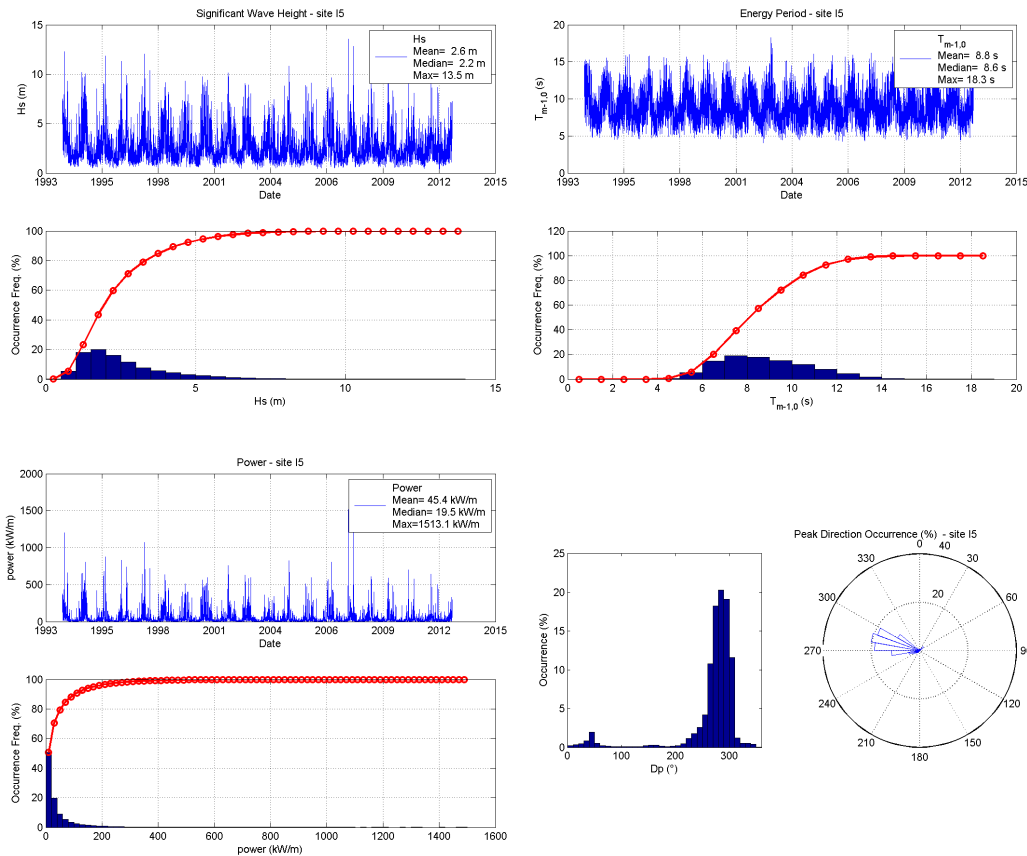


Figure 43: Key statistics for site I5.

Significant wave height at site I5 averages 2.6 m, with a median of 2.2 m and a maximum value of 13.54 m. The associated mean energy period is 8.8 s, giving a mean power of 45.4 kW/m and making this site a rather energetic one. However, it should be taken into account that the median value is only 19.5 kW/m, while the maximum can reach up to 1513 kW/m during storms.

The duration of the database allows an extrapolation of the significant wave height values associated with the 50 year and 100 year return period, using the POT⁷ method with an exponential law fitting. These are presented in Table 10.

Table 10: Significant wave height return values at site I5.

Return period	50 years	100 years
Significant Wave Height (m)	14.6	15.5

⁷ POT : Peak Over Threshold

As can be seen from the histogram of the peak directions, most of this energy is propagated by wave systems travelling from the west to north-west sector, even though north-easterly sea states are also identified.

A joint distribution of the energy period and peak direction as a function of significant wave height (Figure 44) shows that sea-states with low energy period are spread over all the directions while the angular interval over which long period sea-states are observed is restricted to the south-west to north-west sector ($240^\circ - 320^\circ$). These longer period sea states include residual swells with lower H_s , together with energetic wind seas with significant wave heights higher than 6 m corresponding to storms.

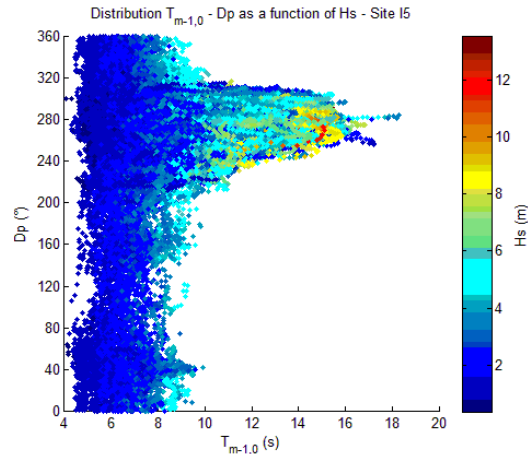


Figure 44: Joint distribution of $T_{m-1,0}$ and D_p as a function of H_s – site I5.

A joint distribution of the significant wave height and peak direction as a function of power $C_g E$ (Figure 45), shows that the angular sector of energetic sea states is slightly broader: 210° to 330° when considering sea-states with H_s of around 4 m to 5 m, but reducing to around 280° for the most energetic sea-states (which correspond to a very limited number of events).

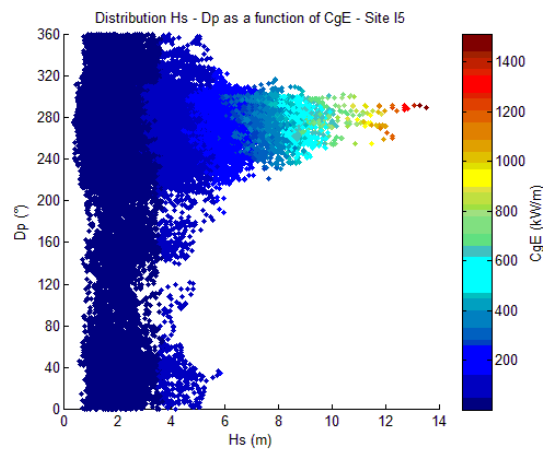


Figure 45: Joint distribution of H_s and D_p as a function of $C_g E$ – site I5.

In addition to these results, the scatter diagram presented in Figure 46 provides information on the distribution of events by bands of the joint parameters $T_{m-1,0}$ and H_s with $1 \text{ s} \times 0.5 \text{ m}$ bins. The most frequent events in the energy period range between 6 and 8 seconds and significant wave height between 1 m and 2 m whilst events with periods above 14 s and H_s higher than 9 m are scarce.

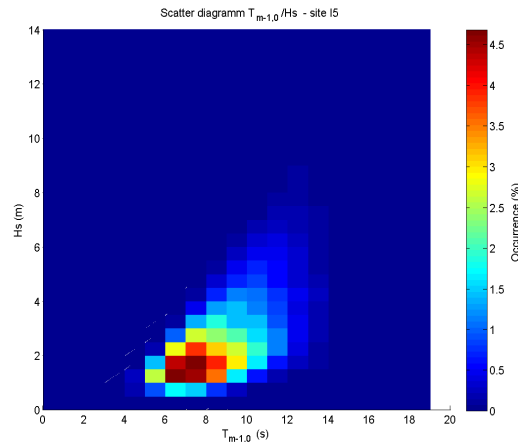


Figure 46 : $T_{m-1,0} - H_s$ scatter diagram – site 15.

As pointed out in the regional analysis, assessment of the seasonal and inter-annual variability of the sea states and available power is of prime importance for the development of marine energy plants. This is now investigated through the analysis of the time-averaged values of the same four parameters.

The annual and monthly variabilities of H_s , $T_{m-1,0}$, $C_g E$ and D_p are presented in Figure 47 to Figure 50. Seasonal variability is clearly visible on the time series of the monthly mean values of the significant wave height over the 19 years of the hindcast dataset (Figure 47, upper plot). Also noticeable is the inter-annual variability, with “winter” mean significant wave heights ranging between 5.2 m and 3.7 m. The histogram of the annual means show that these can be up to 13% higher and 16% lower than the global mean significant wave height (2.58 m). Error bars superimposed onto these annual means indicate the associated standard deviation of the monthly means which can reach up to 1.24 m (1995). The monthly variation is described by the histogram on the lower plot showing monthly means larger than 3 m (up to 3.8 m in January) over the period from November to February and lower than 2 m from May to August (1.7 m in the summer months). Associated standard deviations are around 0.75 m for the most energetic months and 0.22 m during the summer period.

Similar trends are observed for the monthly and annual variability of the energy period $T_{m-1,0}$ (Figure 48). Overall average energy period is 8.81 s and inter-annual variation is limited (less than 1 s). Most noticeable is the seasonal variation of the period with monthly means ranging from 6.78 s to 11.75 s (upper plot) and having an average value of around 10.2 s in the winter months and 7.4 s in the summer period. Such a span of variation could have an influence on the design of structures such as wave energy converters for example, or floating structures with taut moorings, which might have a resonant response.

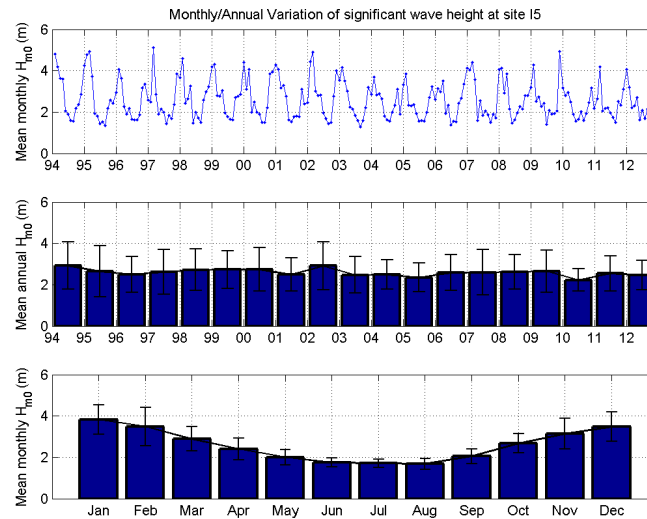


Figure 47: Monthly/annual variation of significant wave height at site I5.

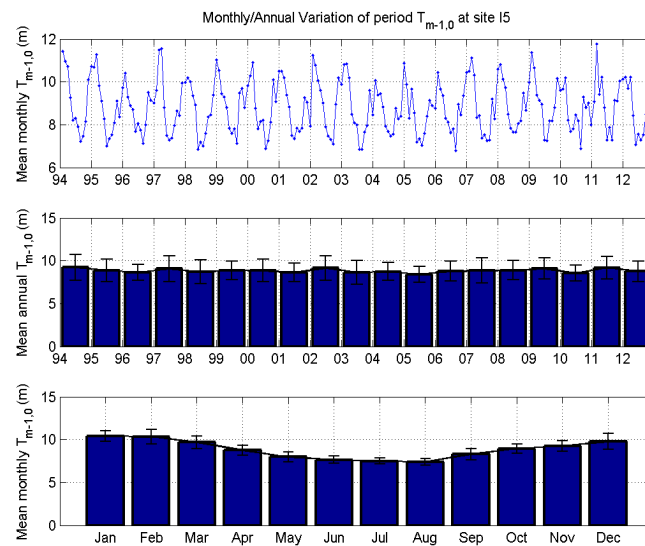


Figure 48: Monthly/annual variation of energy period at site I5.

As a consequence of the significant wave height and energy period variations, an important seasonal and inter-annual variability of the wave energy flux (power) is also seen.

If the overall average power is ~ 45 kW/m, monthly mean values range from 6.3 kW/m to 190 kW/m (Figure 49, upper plot). Monthly average power is above 50 kW/m from November to March, with a peak at around 103 kW/m in January (lower plot). It should be noted that the standard deviation is quite large, about 40 kW/m. Also noticeable is the inter-annual variability (centre plot) with standard deviations larger than 50 kW/m. Available power is very limited, ~ 13 kW/m, during the summer months from June to August.

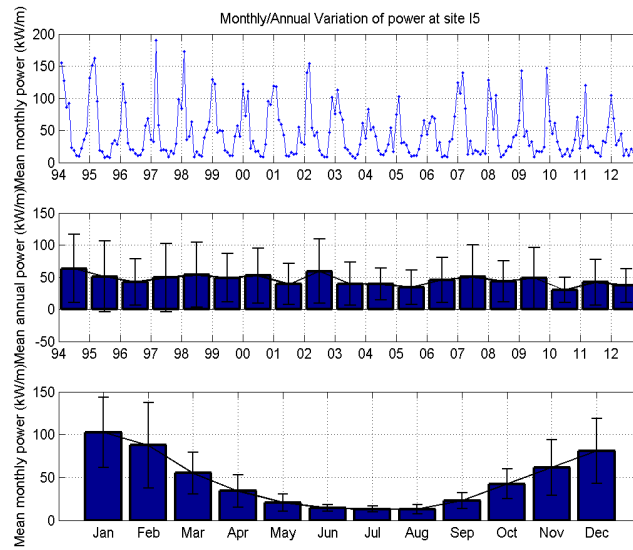


Figure 49: Monthly/annual variation of power at site 15.

Seasonal variability of the peak direction is rather limited (Figure 50) and sea states are predominantly westerly to north-westerly all year long, even though north-easterly events are also identified at this off-shore location.

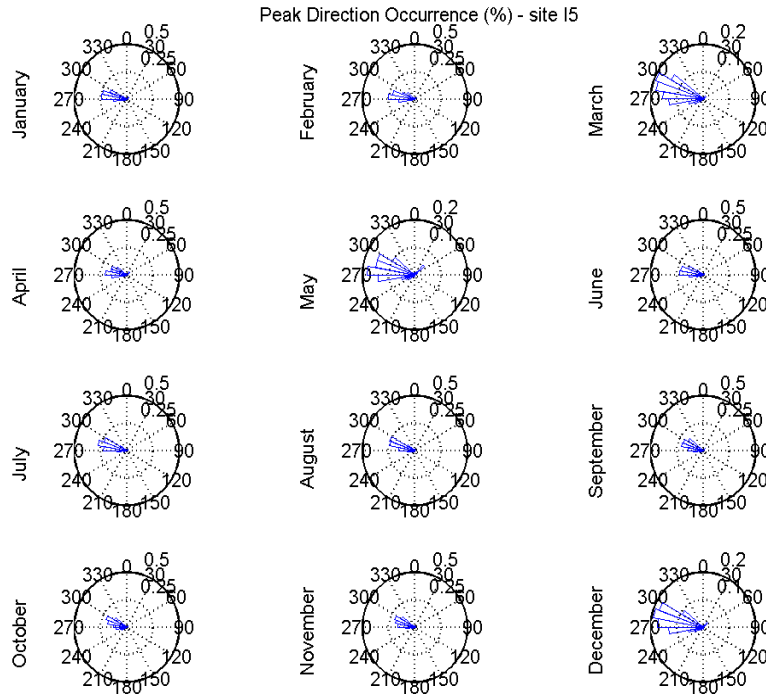


Figure 50: Monthly variability of peak direction at site 15.

Figure 51, where the occurrence of peak directions is superimposed on the average power available per 10° angular sectors, shows that the most energetic sectors (with $C_g E \sim 50$ kW/m) are correlated with those having the highest occurrence. North-easterly events provide on average less power, between 15 and 20 kW/m.

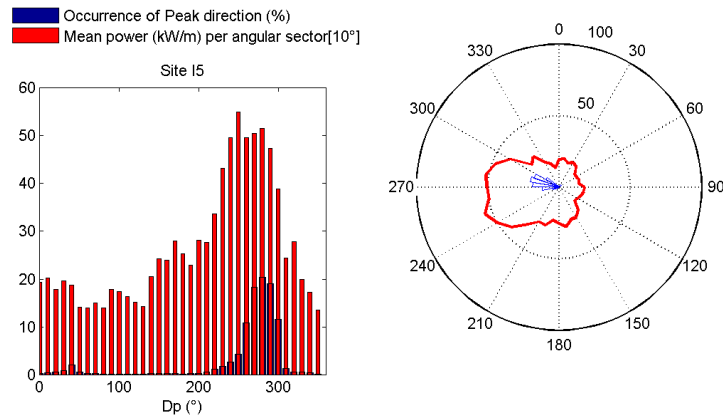


Figure 51: Comparison of power angular distribution with wave peak directions at site I5.

As has been observed, wave seasons do not necessarily match with the calendar seasons. Nevertheless, seasonal variations of the main parameters, evaluated on the basis of the calendar seasons are presented in Figure 52 for the purpose of comparison with other datasets. Spring and summer are identified as less energetic, and a non-negligible inter-annual variability is observed for the winter season.

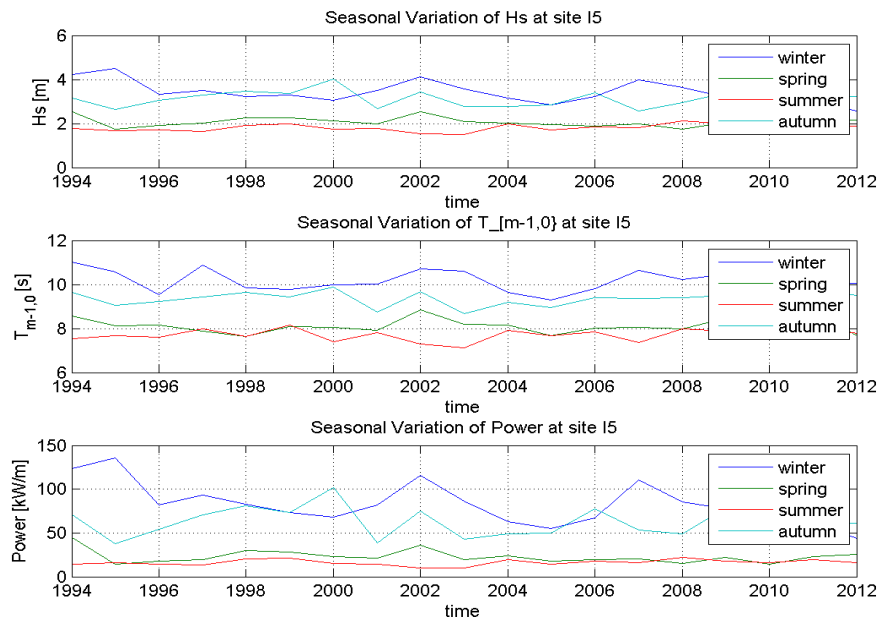


Figure 52: Seasonal variations of H_s , $T_{m-1,0}$ and $C_g E$ at site I5.

Figure 53 presents spectral data in scatter diagram format. For each bin of the scatter diagram, all spectra with parameters that fall within the bin limits (1 m range for H_s , 2 s range for T_e), are plotted together with the min, max and mean frequency spectra.

It can be observed from the shape of the spectra, showing a broad range of distributions of the energy density (especially visible for lower H_s) and secondary peaks that multi-modal sea states occur. Spectra for higher significant wave heights show a more uni-modal shape as sea states are usually dominated by an energetic, fully developed wind sea.

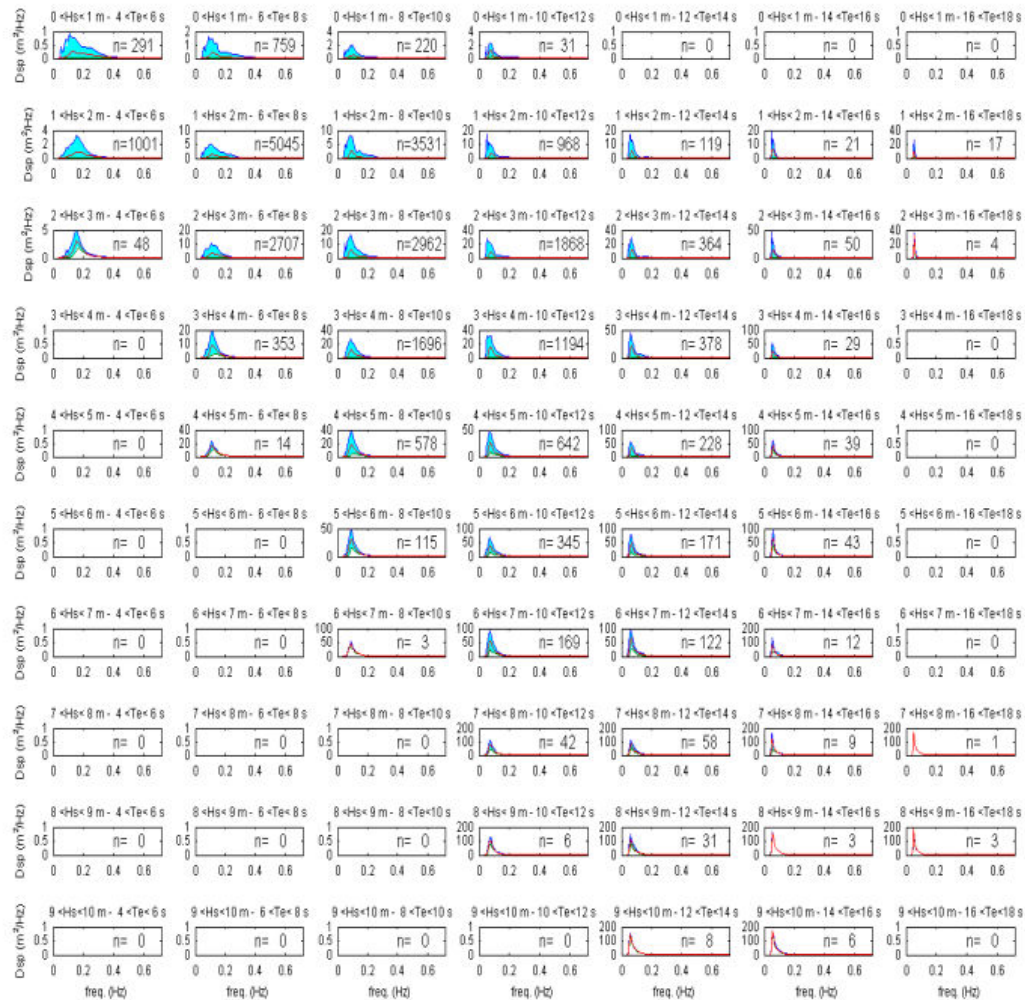


Figure 53 : Spectral variation at site I5, with frequency (Hz) on the x-axis and energy density (m²/Hz) on the y-axis.

Figure 54 illustrates the joint distribution of the significant wave height and energy period as a function of the spectral peakedness factor Q_p (Goda, 1976) whose value increases as the spectral bandwidth narrows. Fully developed wind-seas will have a Q_p value close to 2 ($\text{Log}_{10}(Q_p) \sim 0.3$) while narrow-banded swells will be associated with higher values, occasionally larger than 4 ($\text{Log}_{10}(Q_p) \sim 0.6$), (Saulnier, 2011). According to this, some very narrow-banded swell systems are observed with significant wave height below 4 m while the most energetic events are confirmed to be fully developed wind seas.

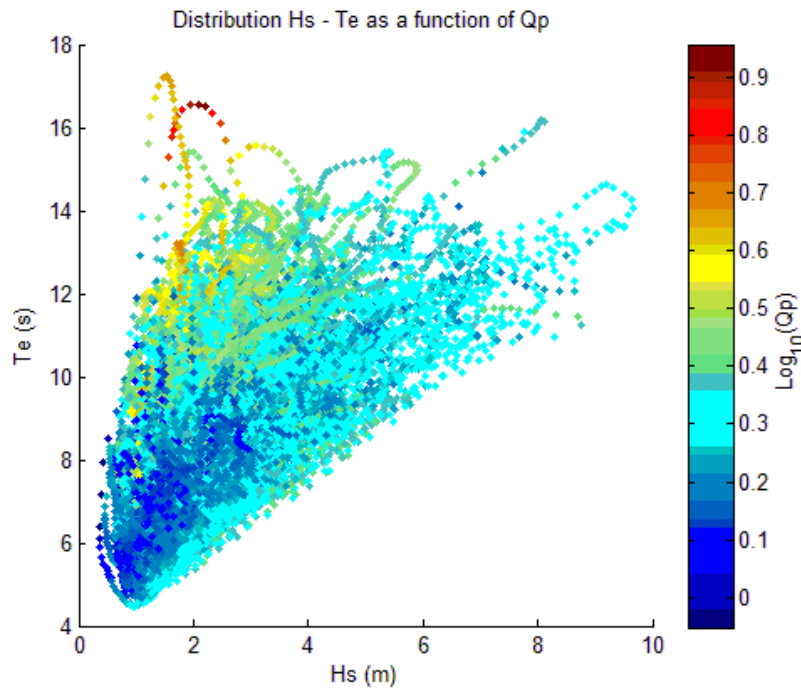


Figure 54 : Joint distribution of H_s and T_e as a function of $\text{Log}_{10}(Q_p)$ at site I5.

Site I7

Statistics for the main sea state parameters H_s , $T_{m-1,0}$, $C_g E$ and D_p for site I7 are presented in Figure 55.

Significant wave height at site I7 is 1.6 m on average overall with a median of 1.3 m and a maximum value of 8.6 m. The associated mean energy period is 8.8 s, giving an average power of 19.8 kW/m, only 43.6 % of that available offshore at location I5. The median value is only 8 kW/m and the maximum reaches 548 kW/m, approximately 35 % of the maximum reached during the strongest events at location I5.

As for site I5, the duration of the database allows an extrapolation of the significant wave height values associated with the 50 year and 100 year return period, using the POT method with an exponential law fitting. These are presented in Table 11. It should be noted that the maximum value identified in the database is close to these return values.

Table 11: Significant wave height return values at site I7.

Return period	50 years	100 years
Significant Wave Height (m)	8.9	9.0

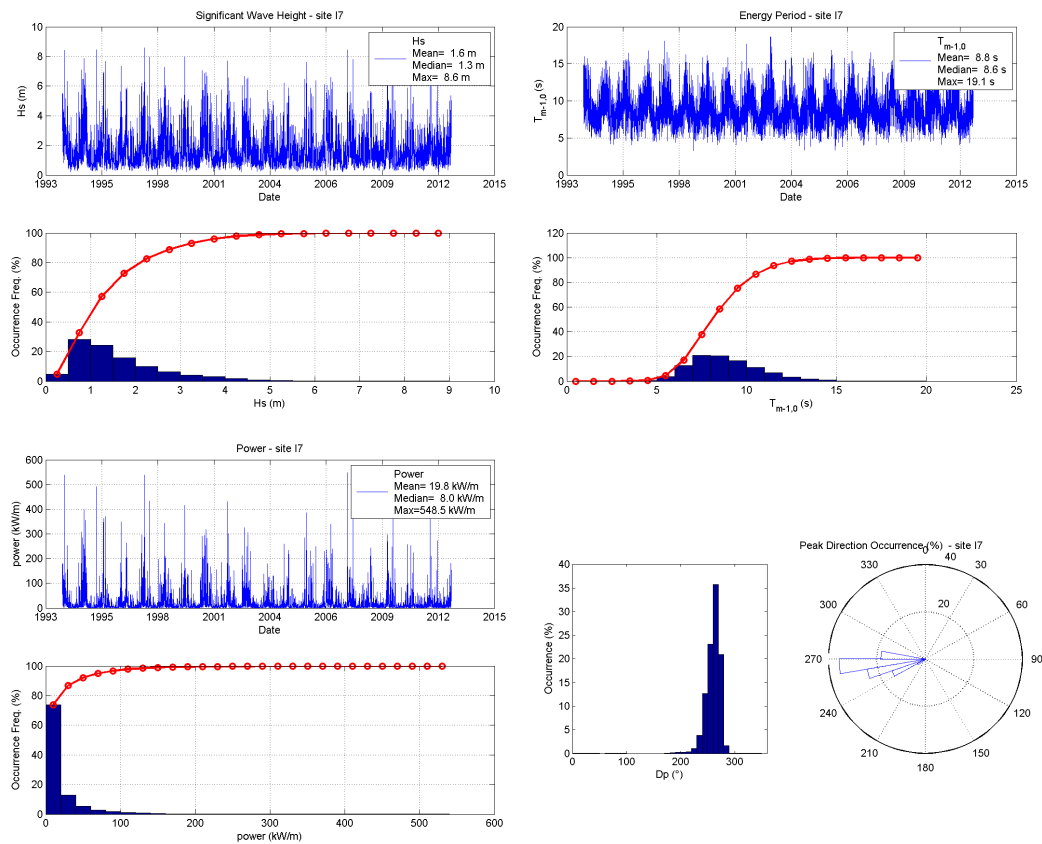


Figure 55: Key statistics for site I7.

As can be seen from the histogram of the peak directions, most of this energy is propagated by wave systems travelling from the south-west to west sector. This change of dominant direction compared to the offshore location is due to both the masking effect of the “Raz-de-Sein” and the cape at the northern end of the Audierne bay, and also to refraction effects. North-easterly sea states are almost non-existent here because of the proximity of the shoreline to the east and the limited available fetch.

This result is confirmed by the joint distribution of the energy period and peak direction as a function of significant wave height (Figure 56) showing that almost all sea states are in the south to north-east sector (180° - 300°). A clear cut-off is visible for wave systems with energy period longer than 10 s which do not propagate from directions more southerly than $\sim 240^{\circ}$, as a result of both the presence of the cape at the southern end of the bay and of refraction phenomena. These longer period sea-states also include the most energetic events with significant wave height up to the maximum value of 8.6 m.

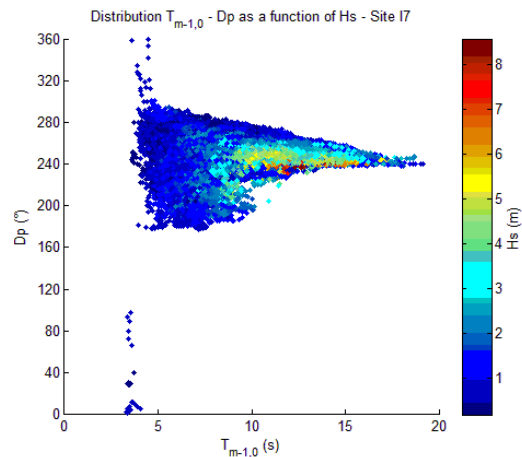


Figure 56: Joint distribution of $T_{m-1,0}$ and D_p as a function of H_s – site I7.

A joint distribution plot of the significant wave height and peak direction as a function of power $C_g E$ (Figure 57) clearly confirms this trend, with an angular sector reducing to a narrow band around 240° as the significant wave height, and hence the power, increases.

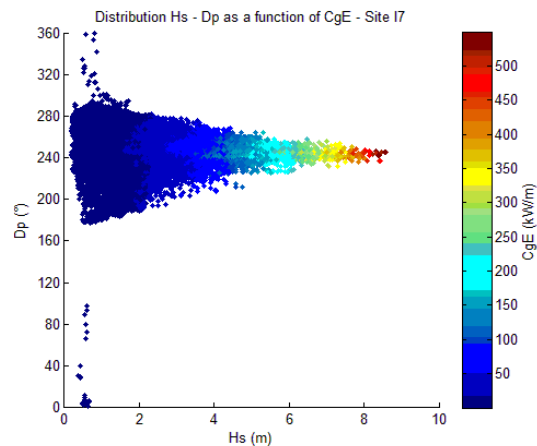


Figure 57: Joint distribution of H_s and D_p as a function of $C_g E$ – site I7.

In addition to these results, the scatter diagram presented in Figure 58 provides information on the distribution of events by ranges of the joint parameters $T_{m-1,0}$ and H_s , with $1 \text{ s} \times 0.5 \text{ m}$ bins. The most frequent events are in the range of energy periods between 7 and 9 seconds and significant wave height between 0.5 m and 1.5 m, whilst events with periods above 14 s and H_s higher than 6 m are scarce.

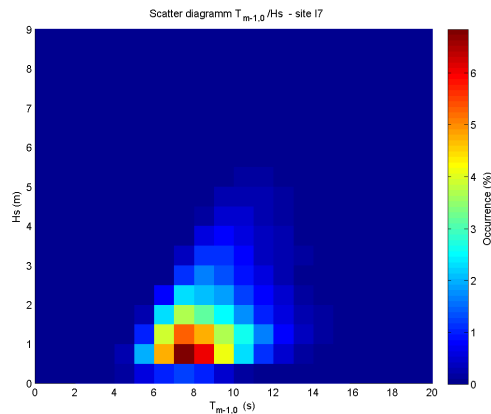


Figure 58 : $T_{m-1,0}$ – H_s scatter diagram – site I7.

The annual and monthly variability of H_s , $T_{m-1,0}$, $C_g E$ and D_p for site I7 are presented in Figure 59 to Figure 62.

Seasonal variability is clearly visible on the time series of the monthly mean values of the significant wave height over the 19 years of the hindcast dataset (Figure 59, upper plot). Also noticeable is the annual variability, with “winter” significant wave heights ranging between 3.2 m and 2.2 m and “summer” significant wave heights of around 1 m.

The histogram of the annual means shows that these can be up to 15% higher or lower than the global mean significant wave height (1.63 m). Error bars superimposed on these annual means indicate the associated standard deviation of the monthly means which can reach up to 0.85 m (1995). The monthly variation is described by the histogram on the lower plot showing monthly means greater than 1.95 m (up to 2.4 m in January) over the period from November to February, and below 1.3 m from May to August. Associated standard deviations are around 0.6 m for the most energetic months and about 0.2 m during the summer period.

Similar trends are observed for the monthly and annual variability of the energy period $T_{m-1,0}$ (Figure 60). The overall average energy period is 8.81 s, and inter-annual variation is limited (less than 1 s). Trends and values are similar to those observed offshore, as could be expected. The seasonal variation of the period with monthly means ranges from 6.73 s to 11.42 s (upper plot), with an average value of approximately 9.9 s in the winter months and 7.4 s in the summer period.

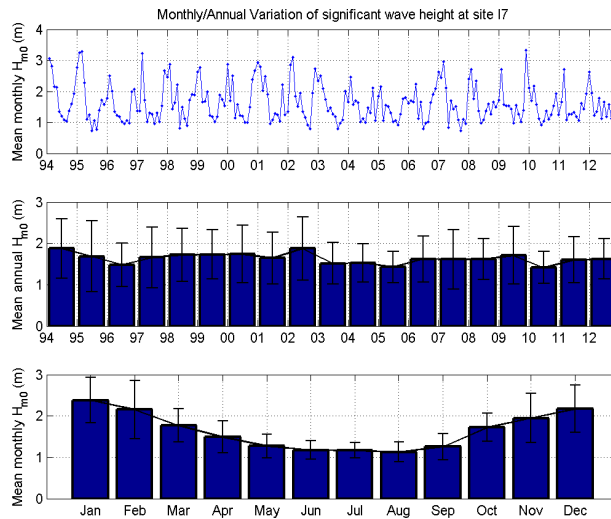


Figure 59: Monthly/annual variation of significant wave height at site I7.

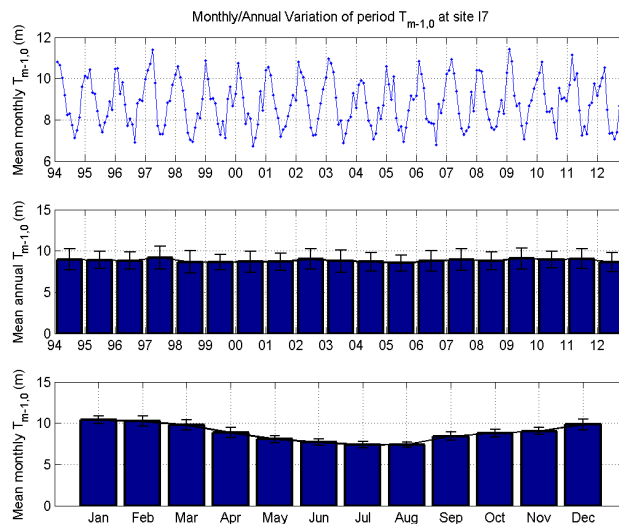


Figure 60: Monthly/annual variation of energy period at site I7.

As a consequence of the significant wave height and energy period variations, a key seasonal and inter-annual variability of the wave energy flux (power) can also be identified.

If the overall averaged power is ~ 19.8 kW/m, monthly mean values range from 2.8 kW/m to 74.8 kW/m (Figure 61, upper plot). The monthly average power is above 25 kW/m from November to March, with a peak of around 44 kW/m in January (lower plot). The standard deviation during these months is ~ 20 kW/m. Also noticeable is the inter-annual variability (centre plot) with standard deviations larger than 20 kW/m. Available power is very limited, about 2.5 kW/m, during the summer months of June to August.

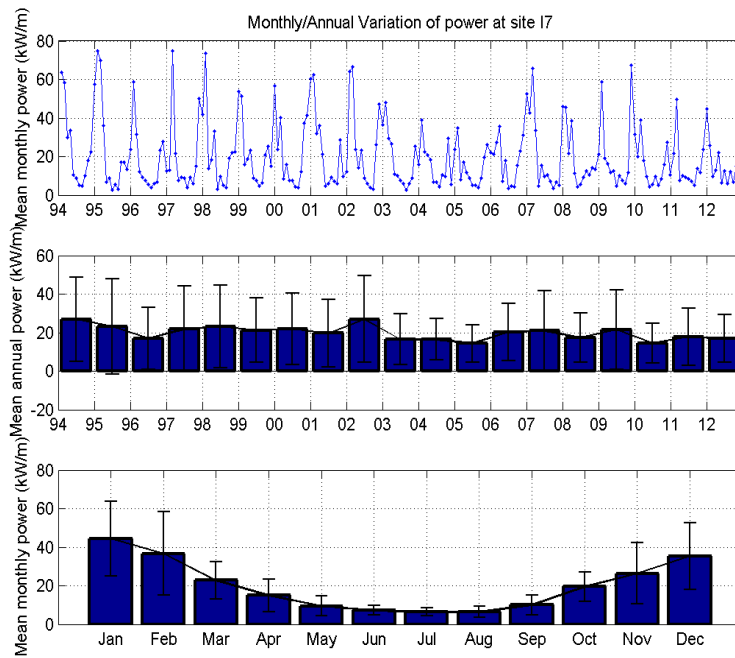


Figure 61: Monthly/annual variation of power at site 17.

The seasonal variability of the peak direction is limited (Figure 62), but it can be observed that sea states are predominantly south-westerly during the winter months and westerly during the summer period.

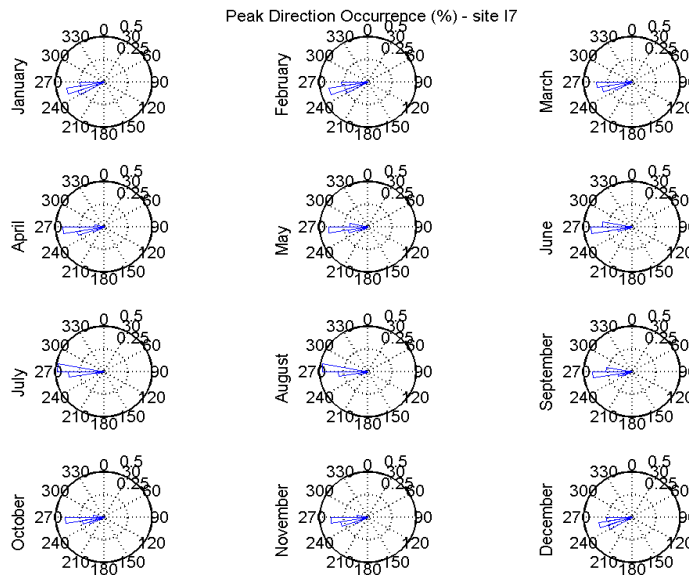


Figure 62: Monthly variability of peak direction at site 17.

In Figure 63, the occurrences of the peak directions are superimposed on the average power available per 10° angular sectors, showing that the most energetic sectors (with $C_g E > 25$ kW/m) are oriented slightly more south-west than those having the highest occurrence.

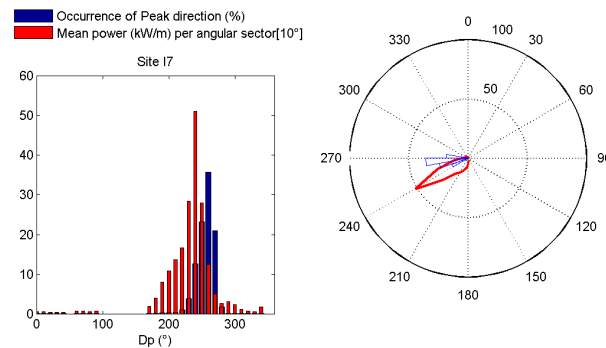


Figure 63: Comparison of the power angular distribution with wave peak directions at site I7.

Seasonal variations of the main parameters, evaluated on the basis of the calendar seasons, are presented in Figure 64 for the purpose of comparison with other datasets. Spring and summer are seen to be less energetic, and a non-negligible inter-annual variability is observed for the winter season.

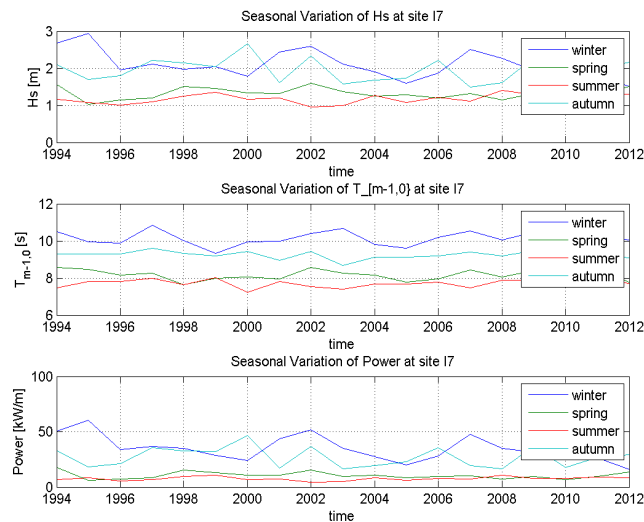


Figure 64: Seasonal variations of H_s , $T_{m-1,0}$ and $C_g E$ at site I7.

Figure 65 presents spectral data in scatter diagram format. For each bin of the scatter diagram, all spectra with parameters that fall within the bin limits (1 m range for H_s , 2 s range for T_e), are plotted together with the min, max and mean frequency spectra.

As could be expected for this less energetic site (I7), a larger number of spectra are observed in the bins associated with the lower values of H_s . These spectra clearly exhibit a broad distribution of energy densities and secondary peaks, indicating that multi-modal sea states occur. Spectra at higher significant wave heights show a more uni-modal shape as sea states are usually dominated by an energetic, fully developed wind sea.

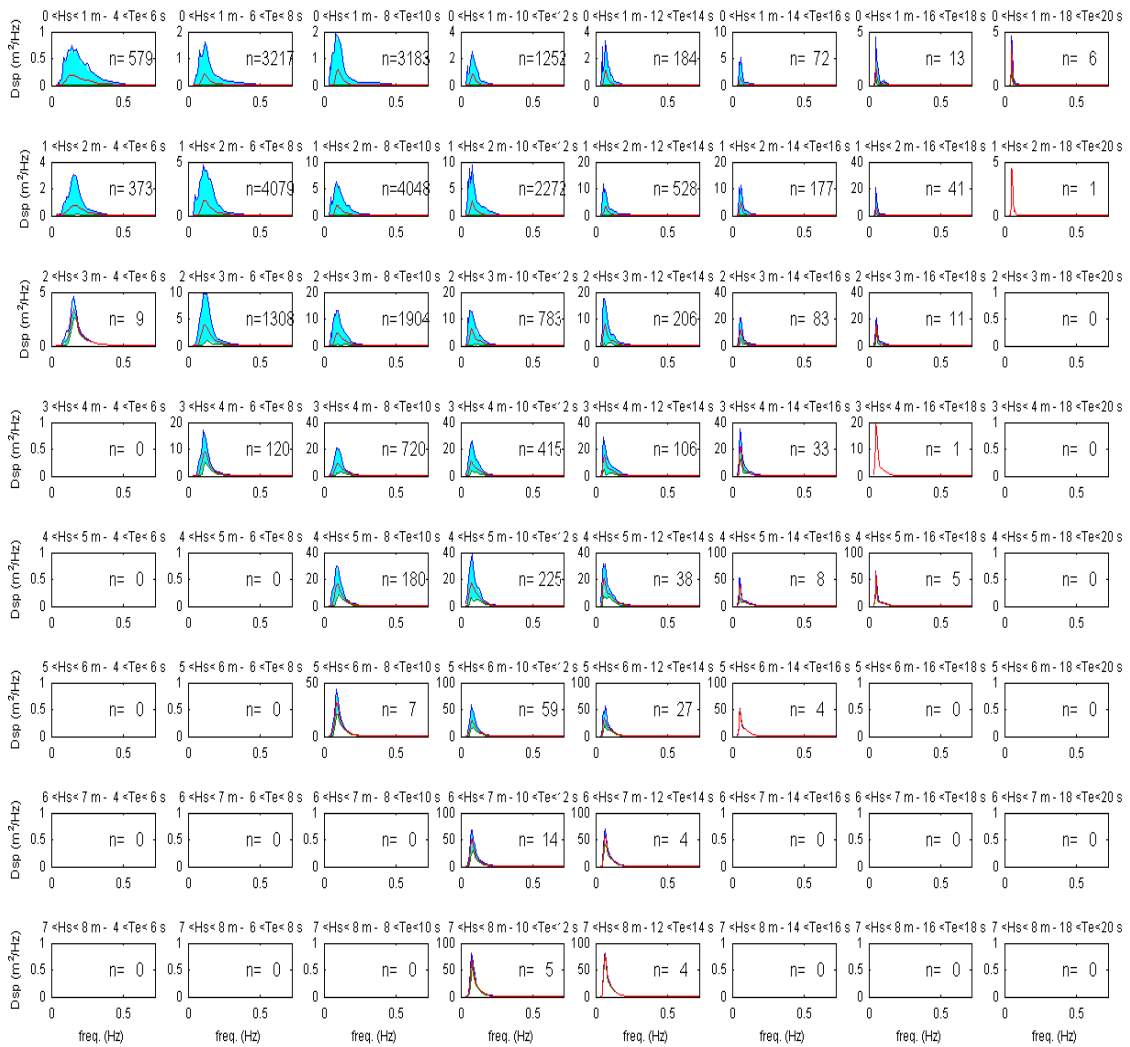


Figure 65 : Spectral variation at site 17, with frequency (Hz) on the x-axis and energy density (m²/Hz) on the y-axis.

Figure 66 illustrates the joint distribution of the significant wave height and energy period as a function of the spectral peakedness factor Q_p (Goda, 1976). As for site 15, some very narrow-banded swell systems are observed with significant wave height essentially below 2 m, while the strongest events are confirmed to be fully developed wind seas.

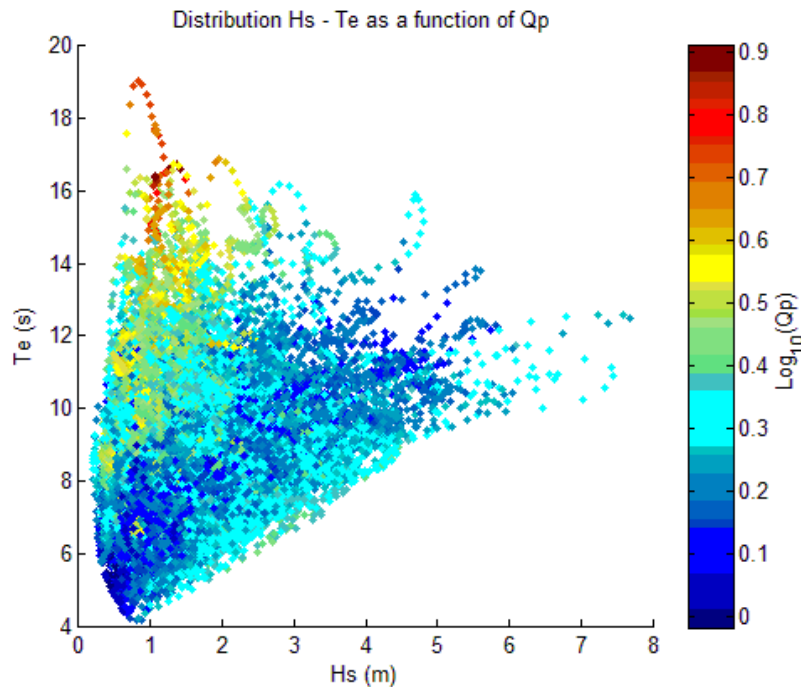


Figure 66 : Joint distribution of H_s and T_e as a function of $\text{Log}_{10}(Q_p)$ at site 17.

4.2.5 Discussion on site comparison

Two major differences can be observed when comparing sites I5 and I7. The first one is related to the direction of the incoming energy. If the predominantly energetic sector is from south-west to north-west offshore (I5), with low sea states incoming from all directions, it reduces to a narrower angular range slightly more to the south-west at site I7, because of both sheltering effects of the coast, which also limits the fetch to the east, and the refraction effects as waves propagate to shallower depths.

The second effect, which is certainly the most noticeable, is the dissipation of energy from the offshore location I5 to the nearshore location I7. The power available nearshore is only about 43 % of the power available offshore, mostly because of the energy dissipation during the propagation of wave systems in intermediate water depths (between ~ 118 m and ~ 40 m). Nevertheless, studies described in the previous section point out the strong variability of the resource, especially offshore where during extreme events, a power of ~ 1500 kW/m was identified. However, when considering wave energy extraction, one should consider that during such energetic events, corresponding to extreme storms, devices are unlikely to be operational and would most probably be in 'survival' mode. Hence, the power associated with such extreme events should not be accounted for as part of the available or extractable power.

We can consider, for example, a "production" threshold for the significant wave height, such that power is not accounted for as part of the available power for events with significant wave height above that threshold. Figure 67 and Figure 68 show the time series of significant wave height and power at locations I5 and I7 respectively, considering a 5 m 'production' threshold. Such a threshold could be considered low for some wave energy converters, but is still reasonably high for different types of devices and provides an interesting insight into the problem. This threshold was actually selected because it reduces the maximum power at both sites to a similar value close to 200 kW/m (about four times the off-shore average value),

whilst not eliminating too large a number of events. Significant wave height remains below the threshold 92.27% of the time offshore and 98.76% nearshore.

With this threshold, the offshore extractable mean power reduces to 26.5 kW/m, and the nearshore to 17.2 kW/m, giving a ratio of 65 %. It should be noted that the median value nearshore is minimally affected, only being reduced by 4%.

This example shows that when investigating wave energy production sites, *a priori* less energetic sites should not be neglected; what should be considered is the actual extractable energy together with the additional cost related to structural design and reliability of the structure induced by the higher constraints and loadings of harsher offshore environments.

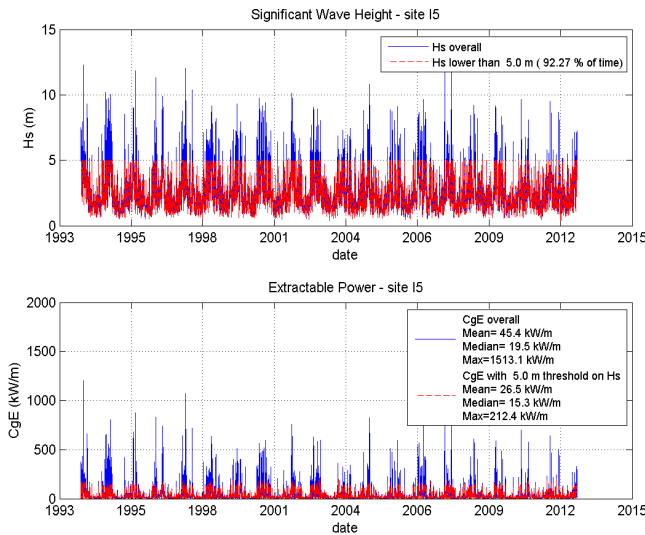


Figure 67 : Power statistics with 5m H_s threshold - site I5.

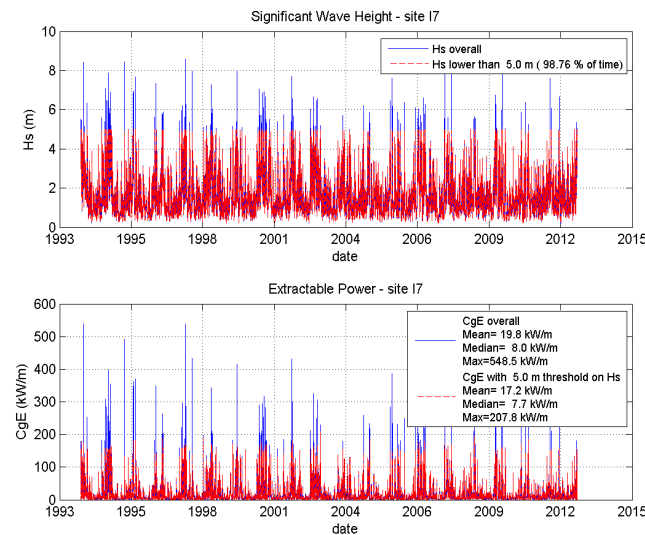


Figure 68: Power statistics with 5m H_s threshold - site I7.

4.3 Numerical modelling of currents

The current model used here to create datasets for tidal resource assessment is the MARS model (Model for Application at Regional Scale) developed at IFREMER (see § 2.2.2) and operationally used in the Previmer⁸ service. It was designed for the simulation of flows in coastal areas from the regional scale down to the scale of small bays or estuaries where circulation is generally driven by complex processes. Datasets used for this analysis were extracted from the Mars 2D Manga 700 database, providing information on current velocity and direction on a 700 m resolution regular grid covering the Channel and the Bay of Biscay with a one hour time step. The forcing wind field is the Météo-France ARPEGE meteorological data.

The Iroise Sea circulation has been widely studied, especially since the 1980s, and sensitivity to large scale circulation, mostly in the west of the area, has been identified, as well as more seasonal variability which can be found closer to Ouessant Island (Muller *et al.*, 2010). Nevertheless, as this resource assessment study mostly focuses on the most energetic locations of the Iroise Sea dominated by tidal currents, a one year time series of data was considered in this study.

4.3.1 Current modelling results: Regional

In order to provide an overview of the regional distribution of currents in the Iroise Sea, a map of the maximum local velocities (i.e. maximum current velocity identified at each point of the grid over the one year of data) is plotted in Figure 69.

The strongest currents, with velocities over 4 m/s are identified in the Fromveur Strait and along the north-western coast of Ouessant Island. Other identified areas with strong currents, i.e. velocities over 3m/s, include the straits between the islands in the Molène archipelago as well as the areas in the west (Chaussée de Sein) and in the east (Raz de Sein) and of Sein Island in the south. Energetic currents are also visible along the north coast.

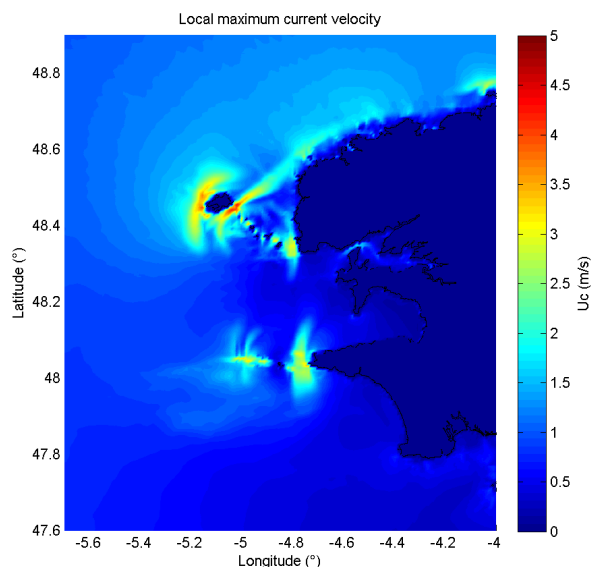


Figure 69: Local maximum current velocity in the Iroise Sea.

⁸ www.previmer.org

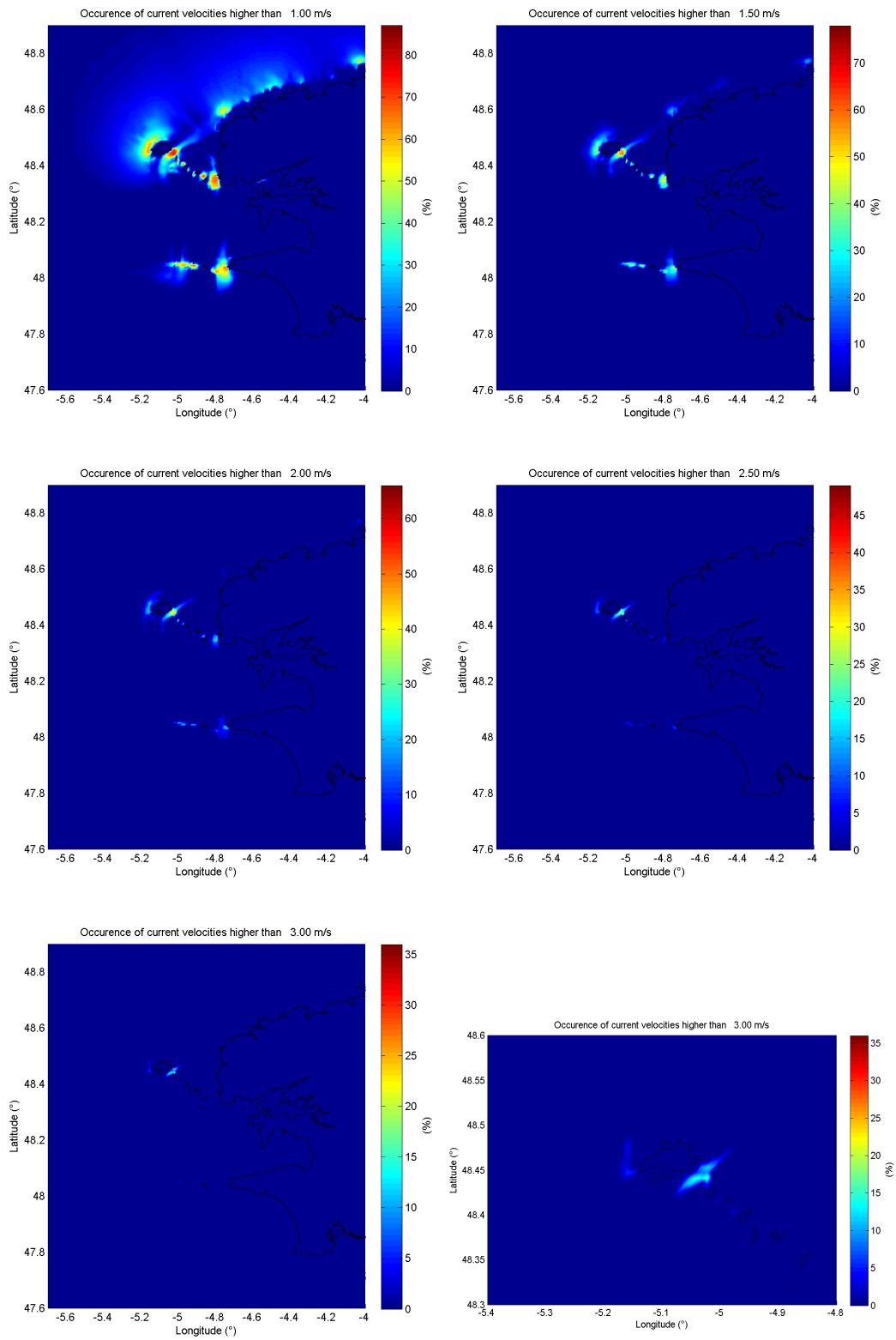


Figure 70: Occurrence of current velocities above a threshold velocity.

In order to assess the actual potential, it is not only the maximum values that should be considered but also the frequency of occurrence of flows with velocities above a given threshold.

Maps provided in Figure 70 indicate the percentage occurrence of velocities above thresholds of 1 m/s, 1.5 m/s, 2 m/s 2.5 m/s and 3 m/s.

If the general pattern of this mapping is similar to the one observed for the distribution of maxima for velocities up to 1.5 m/s, the locations where currents above 2 m/s are observed are much more limited, and this is reduced to only the Fromveur strait and the south-western coast of Ouessant Island for velocities above 3 m/s (lower right figure is a zoom of lower left figure over that area).

In fact, currents reach velocities above 2m/s for a maximum 65% of the time over a very limited area in the Fromveur, and closer to 40% of the time in the other areas of this strait. This reduces to 35% locally and less than 15% globally in the strait for velocities above 3 m/s.

4.3.2 Current modelling results: Site specific

The Fromveur strait has been identified as a potential site for deployment of tidal current turbines, and therefore provides a location for a more specific study.

The point with the highest velocity identified by the model in the strait is considered here. Coordinates of this point are 5°1.398'W, 48°27.228'N, with water depth ~56 m.

The amplitude and direction of the current velocity derived from the zonal and meridional components are plotted in Figure 71 and Figure 72 for the three first months of the year, together with the sea level elevation. Periods of spring and neap tides can be clearly observed.

The maximum identified velocity over the whole time series is 4.26 m/s. The maximum amplitude of the water level variation identified during spring tides is 3.6 m, so the maximum tidal range is therefore approximately 12% of the mean water depth.

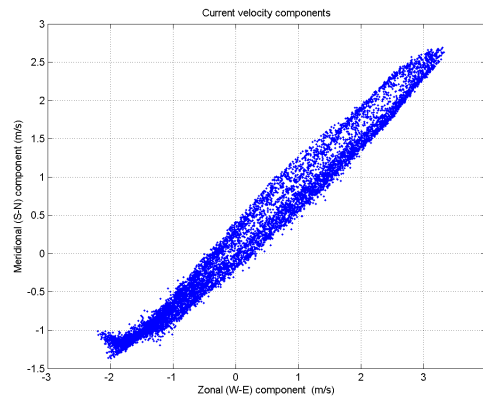


Figure 71: Current zonal and meridional components.

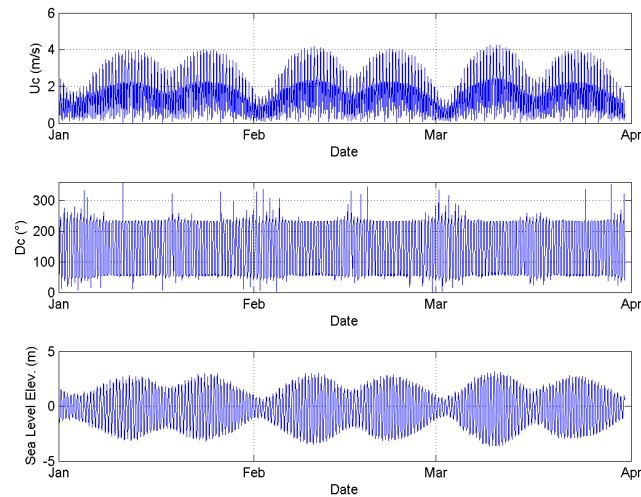


Figure 72: Time series of current velocity and direction, and sea level elevation.

The distribution of current direction is clearly marked, with a flow from 56.7° during ebb and from 230° during flood. Current directions take all values over the range 0° to 360° during slack water times and, as can be observed in Figure 72, are more likely to be in the northern sector during neap tides.

From the distribution of velocities as a function of direction, plotted in Figure 73, current velocities observed during ebb are lower than those observed during flood and barely reach values of 2.45 m/s. Average direction during ebb is 56° while average flood direction is 173.4° so that a misalignment of about 6.6° is observed between ebb and flood. A trend is also observed on the direction of the ebb velocities, slightly shifting by about 10° to the east for velocities above 2 m/s. Finally it is observed that the higher the velocities, the narrower the directional spreading.

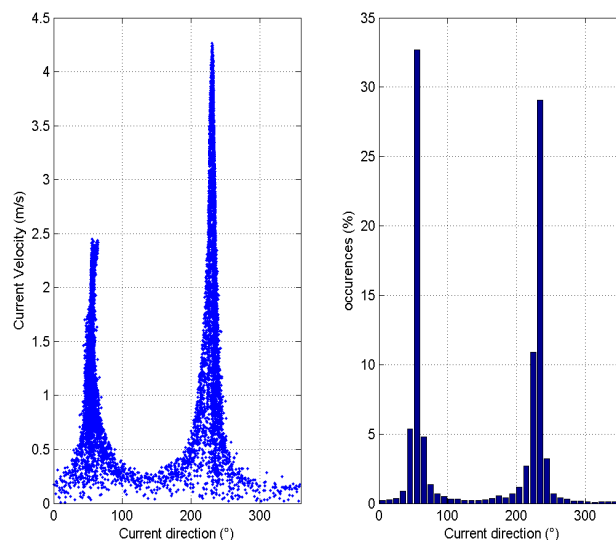


Figure 73: Ebb and flood current direction.

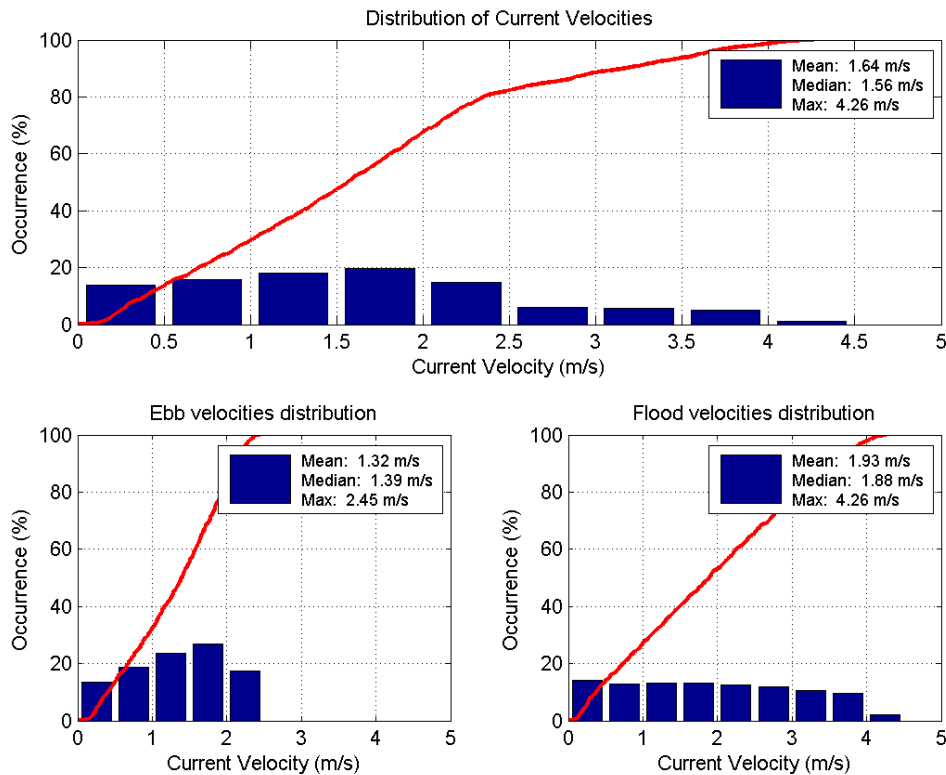


Figure 74: Distribution of current velocities.

The main ebb and flood current statistics are presented figure 74. Mean ebb velocity is 1.32 m/s, with a principal mode between 1.5 m/s and 2 m/s. Ebb velocities are lower than 2 m/s for 83% of the time.

Mean flood velocity is 1.93 m/s but velocities are evenly distributed, between 14% and 10.7 % per 0.5 m/s bin between 0 m/s and 3.5 m/s. Flood velocities are higher than 2 m/s about 47% of the time.

An asymmetry of the flow between flood and ebb such as the one identified at this site is not just a local feature, but can be observed all along the Fromveur strait. Nevertheless, variability in direction and velocity of the tidal current is highly site dependent because of the complexity of the flow and the bathymetry, and specific surveys should be conducted at any deployment site as identification of this variability is of prime importance for the design and array layout of a tidal plant as well as the assessment of its overall efficiency.

Of interest for the characterisation of the resource, in addition to current velocities, is the power of the flow and its distribution.

The power of the flow passing through a unit area is given by:

$$P=0.5*\rho*v^3 \quad (W/m^2)$$

Where ρ is the water density ($\rho=1024 \text{ kg/m}^3$) and v is the current velocity.

Map plotted figure75 shows the distribution of the local maximum current power in the Iroise Sea and is to be compared to the map of local maximum current velocity (figure 69).It can be observed that areas with high power level are more restricted.

Histograms of the power estimated at the same location in the Fromveur strait are plotted figure 76. It is observed that the power is less than 5 kW/m² 75 % of the time and less than 10 kW/m² ~85% of the time overall and 100% of the time during ebb.

These values identified from model data provide an estimate at a given location. Because of the high variability in space of the flow in such an energetic area, it would be recommended to conduct local in-situ surveys.

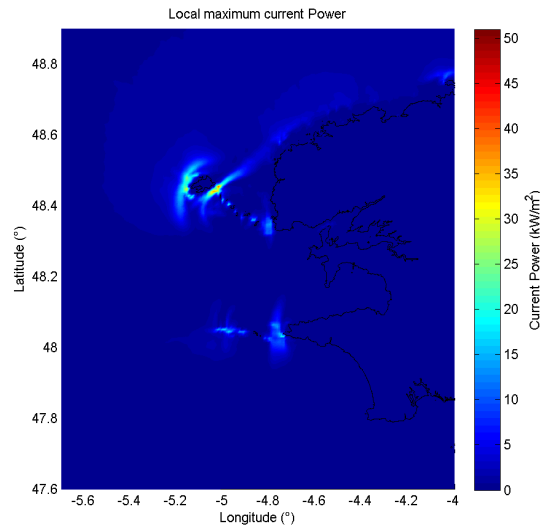


Figure 75 : Local maximum current power in the Iroise Sea.

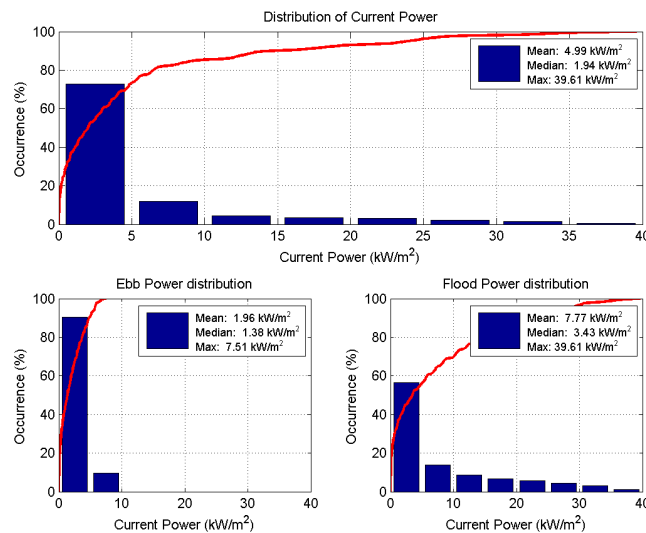


Figure 76 : Distribution of current power.

Part of the complexity of the flow in the Iroise Sea is due to wave-current interaction. Waves will affect the local kinematics of the tidal flow, especially in the intermediate depths of the Molène archipelago. In return, currents will modify the main characteristics of the waves and sea states through different processes such as refraction. Some specific features related to wave-current interaction in the Iroise Sea are presented in the following section.

4.3.3 Wave-Current interaction

As previously discussed, strong tidal currents occur at various locations in the Iroise Sea. It can be seen from wave measurements made by the buoy 02911/62069 “Les Pierres Noires” that the significant wave height is modulated at the tidal period. Figure 77 shows that the coupling of current with wave propagation introduced in the wave model allows this modulation to be modelled well (on the plot, model prediction is blue, measurement is red). It was observed that in certain situations, the amplitude of this modulation could reach values of about 1 m. A Fourier analysis of the significant wave height obtained from the model at that location for the year 2008 clearly shows the tidal harmonics in the wave signal (especially at the M2 harmonic 12 h 25 min period), confirming this strong coupling (Figure 78).

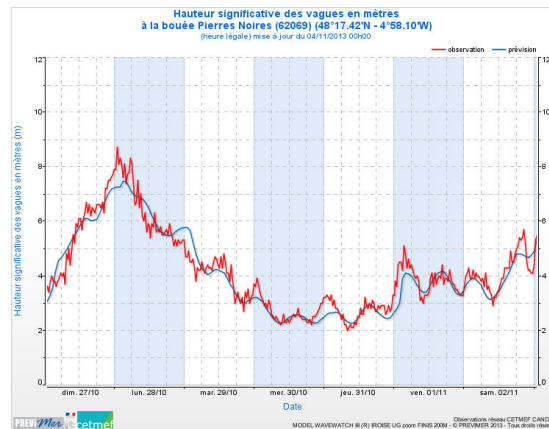


Figure 77: Measurement and modelling of significant wave height at buoy 02911/62069.

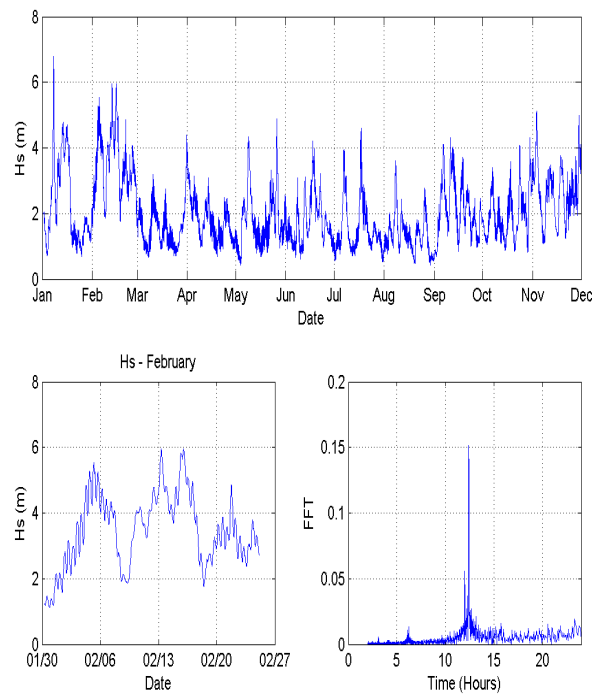


Figure 78: Fourier analysis of the significant wave height.

This modulation is also observed in other characteristic wave parameters such as peak period, peak direction or even directional spreading. As described by Ardhuin *et al.* (2012), this modulation effect is related to refraction by the strong tidal currents. This cyclic modulation must be accounted for in the statistics for sea state characterisation, especially if it is not just a local effect, as it might affect design of wave energy converters as well as management of marine operations.

In order to assess the influence of tidal currents on sea state characteristics at a regional scale, a Fourier transform of the time series of the significant wave height was performed at each point of the model's computational grid in order to assess the amplitude of the component at the tidal period (even though various tidal harmonics could be identified, only the M2 tidal component is considered here).

Figure 79 shows the non-dimensional amplitude of the tidal component of the significant wave height normalised by the maximum amplitude of this tidal component observed over the domain. This coefficient is expressed as a percentage and the colour scale on the map has been limited to 50% in order to make the lower amplitudes more visible.

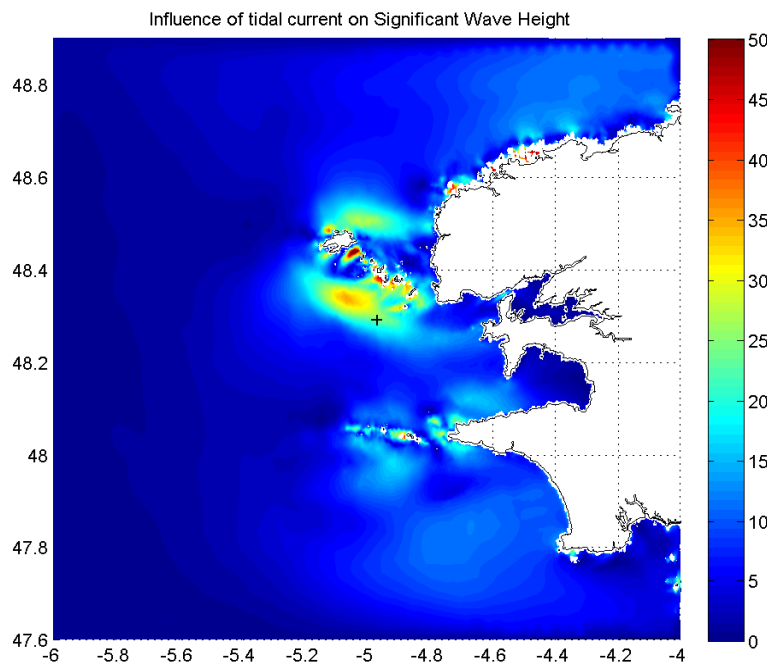


Figure 79: Influence of tidal currents on significant wave height.

If large amplitudes of modulation are observed in strong current areas such as Fromveur or the northern coast of Ouessant Island, important modulations are also visible in other locations where currents are more limited. Buoy 02911/62069 (marked with a black cross in Figure 79) is in a modulated area even though it is out of the main current streams (see Figure 69). Tidal effects are also visible, although more limited, in the Audierne bay where current velocities are much lower (max velocity of ~ 0.5 m/s).

5 Conclusions

This report was produced as a deliverable of the study on “Resource assessment and mapping” conducted as part of Task 3.1 of the work package on “Technology Support” for the MERiFIC project. Its main objective is to provide an overview of resource assessment techniques, and of the renewable resource available in both the South West UK region, including the Isles of Scilly, and the Iroise Sea, France, for the development of ocean energy converters, mainly for wave and tidal current energy extraction. Additional information related to environmental characterisation for the management of marine operations can be found in the Merific deliverable 3.6.2 “*Best practice on installation procedures*”.

This report does not attempt to compare resource assessment techniques or the available resource in the two regions, or to make recommendations on best practice. For information on these issues, the reader is referred to MERiFIC deliverables 3.1.5, “*Cross-analysis of resource assessment methods*”, and 3.1.6, “*Best practice guidelines for wave and current resource assessments for island communities*”.

However, high-level conclusions can be drawn from this report. In particular, some elements of climatology have similarities in both areas, especially the seasonal and inter-annual variability of the available wave power. The geographical variability of the resource has also been clearly defined, with a clear reduction in available power in the nearshore regions and in the leeway of the islands.

A major difference between the two areas is the existence of strong tidal currents in the Iroise Sea where a specific location, the Fromveur strait, is identified as a possible deployment site for tidal turbines. A strong interaction of these currents with waves is seen, which affects the local variability of the sea-states. This will inevitably have implications for marine energy development, and further research in this area is required.

6 References

Akpinar, A. & Komurcu, M.I., 2012. Wave energy potential along the south-east coasts of the Black Sea. *Energy*, 42(1), 289-302.

Arakawa, A., 1966. Computational design for long-term numerical integration of the equations of fluid motion: Two-dimensional incompressible flow. Part I. *Journal of Computational Physics*, 1, 119-143.

Ardhuin, F., Roland, A., Dumas, F., Bennis, A.-C. Sentchev, A., Forget, P., Wolf, J., Girard, F., Osuna, P. & Benoit, M., 2012. Numerical wave modeling in conditions with strong currents: Dissipation, refraction, and relative wind. *Journal of Physical Oceanography*, 42, 2101-2120.

Ashton, I.G.C., 2011. PRIMaRE wave buoy array - Data processing and quality control guidelines. Technical report, University of Exeter.

Blumberg, A.F. & Mellor, G.L., 1987. A description of a three-dimensional coastal ocean circulation model. *Three-dimensional Coastal Ocean Models, Coastal and Estuarine Sciences*, 4, 1-16.

Booij, R.C. Ris, N. & Holthuijsen, L.H., 1999. A third-generation wave model for coastal regions, Part I, Model description and validation. *Journal of Geophysical Research*, 104(C4), 7649-7666.

Boudiere, E., Maisondieu, C., Ardhuin, F., Accensi, M., Pineau-Guillou, L. & Lepesqueur, J., 2013. A suitable metocean hindcast database for the design of marine energy converters. *International Journal of Marine Energy*, 3-4, e40-e52.

Boudière, E. & Maisondieu C., 2014. Manuel de l'utilisateur de la base de données HOMERE. RDT/LCSM/C&R14LCSM301/EB/CM, Ifremer.

Goda, Y., 1976. On wave groups. *Proc. 1st Behaviour of Offshore Structures Conference*, Norwegian Institute of Technology, Trondheim.

Helzel, T., Kniephoff, M., Petersen, L., Mariette L. & Thomas N., 2011. Accuracy and Reliability of Ocean Radar WERA in Beam Forming or Direction Finding Mode. *Proc. IEEE CWTMC Workshop*, Monterey, 2011.

Iglesias, G. & Carballo, R., 2010. Wave energy resource in the Estaca de Bares area (Spain). *Renewable Energy*, 35(7), 1574-1584.

Ingram, D., Smith, G.H., Bittencourt-Ferreira, C. & Smith, H. (eds.), 2011. *Protocols for the Equitable Assessment of Marine Energy Converters*. University of Edinburgh, School of Engineering Publishers, Edinburgh.

Kim, G., Jeong, W.M., Lee, K.S., Jun, K. & Lee, M.E., 2011. Offshore and nearshore wave energy assessment around the Korean Peninsula. *Energy*, 36(3), 1460-1469.

Lazure P. & Dumas F., 2008. An external-internal mode coupling for a 3D hydrodynamical model for applications at regional scale (MARS). *Advances in Water Resources*, 31(2), 233-250.

Le Hir, P., Cayocca, F. & Waeles, B., 2011. Dynamics of sand and mud mixtures: a multiprocess-based modelling strategy. *Continental Shelf Research*, 31(10), 135-149.

Longuet Higgins, M.S., Cartwright, D.E. & Smith, N.D., 1963. Observations of the directional spectrum of sea waves using the motions of a floating buoy. *Ocean Wave Spectra*, Prentice-Hall, 111-136.

Muller H., Blanke B., Dumas F. & Mariette V., 2010. Identification of typical scenarios for the surface Lagrangian residual circulation in the Iroise Sea. *Journal of Geophysical Research: Oceans*, 115, C07008, doi:10.1029/2009JC005834.

Osalusi, E., Side, J. & Harris, R., 2009. Structure of turbulent flow in EMEC's tidal energy test site. *International Communications in Heat and Mass Transfer*, 36(5), 422-431.

Rogers, W.E., Hwang, P. A., & Wang, D. W., 2003. Investigation of Wave Growth and Decay in the SWAN Model: Three Regional-Scale Applications. *Journal of Physical Oceanography*, 33(2), 366-389.

RTE, 2013. *Bilan Electrique 2013*, RTE.

Saha, S. *et al.*, 2010. The NCEP Climate Forecast System Reanalysis. *Bulletin of the American Meteorological Society*, 91, 1015–1057.

Saulnier, J.B., Clément, A., Falcão, A.F. de O., Pontes, T., Prevosto, M. & Ricci, P. , 2011. Wave groupiness and spectral bandwidth as relevant parameters for the performance assessment of wave energy converters. *Ocean Engineering*, 38(1), 130-147.

Smith, H.C.M., Haverson, D. & Smith, G.H., 2013. A wave energy resource assessment case study: Review, analysis and lessons learnt. *Renewable Energy*, 60, 510-521.

Tolman, H.L., 1999. User manual and system documentation of WAVEWATCH-III version 1.18, NOAA / NWS / NCEP / OMB Technical Note 166.

Tucker, M.J., 1993. Recommended standard for wave data sampling and near-real-time processing. *Ocean Engineering*, 20, 456-474.

Appendix A: Validation testing for the SWAN wave model for SW England

This appendix presents a more in-depth overview of the Exeter SWAN model validation data.

Error dependence on wave height and period

By looking at the error in more detail dependencies between the error and some parameters can be found. Figure 80 to Figure 83 present the bias and root mean square error of H_{m0} and $T_{m-1,0}$ binned by H_{m0} and $T_{m-1,0}$. The number of observations in each bin is shown in Figure 84.

Figure 80 shows that the largest negative bias (larger than 0.5 meters) occurs either for very steep waves or long waves. The largest positive bias occurs for long waves with wave heights smaller than 1 meter. The smallest bias can be found for wave heights between 0 and 3 meters and wave periods between 4 and 10 seconds. The probability of occurrence in this range is also the highest, see Figure 84. The root mean square error, shown in Figure 81, demonstrates the same trend as for the bias.

All bias on $T_{m-1,0}$ is negative, see Figure 82. A clear correlation can be seen between the bias and the steepness of the waves. The smallest bias is found for the steeper waves, whereas the largest bias (circa 5 seconds) can be found for long small waves. The root mean square error, shown in Figure 83, demonstrates a similar trend to the bias.

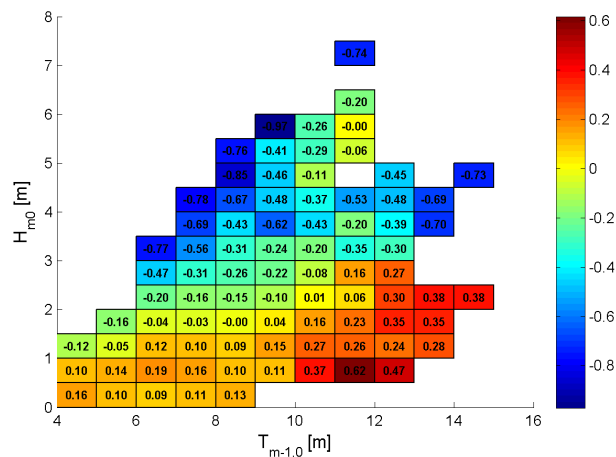


Figure 80: Bias H_{m0} [m] Exeter wave buoy D.

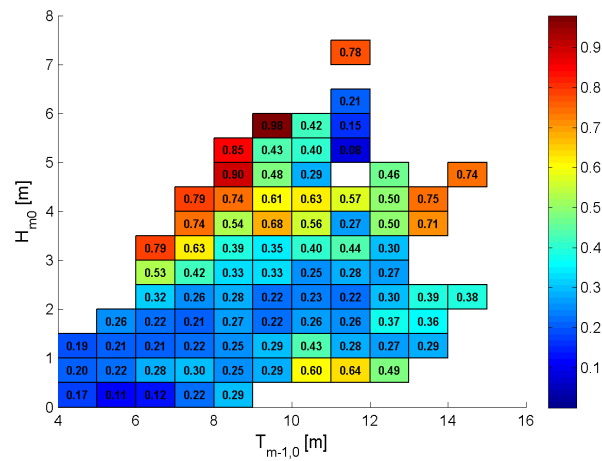


Figure 81: Root mean square H_{m0} [m] Exeter wave buoy D.

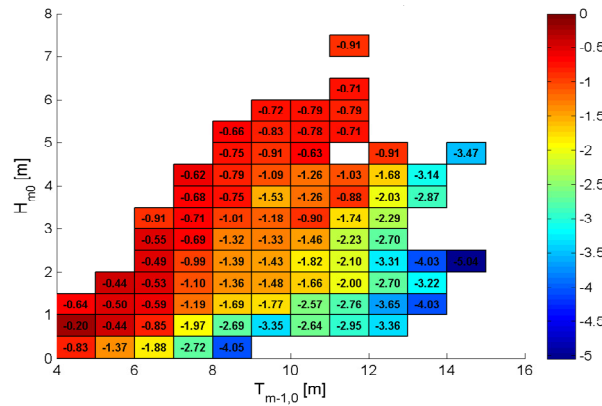


Figure 82: Bias T_{m-10} [s] Exeter wave buoy D

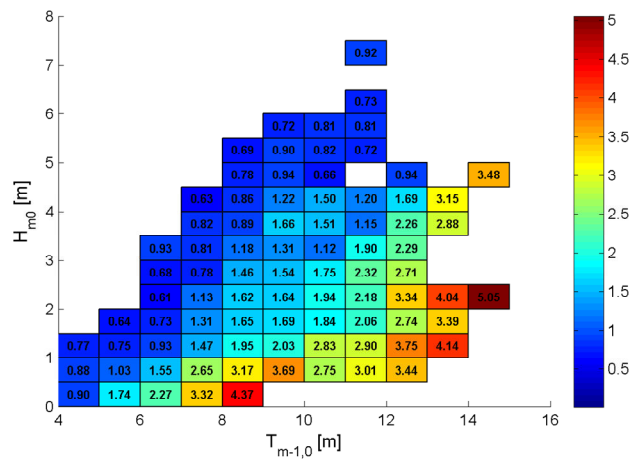


Figure 83: Root mean square T_{m-10} [m] Exeter wave buoy D

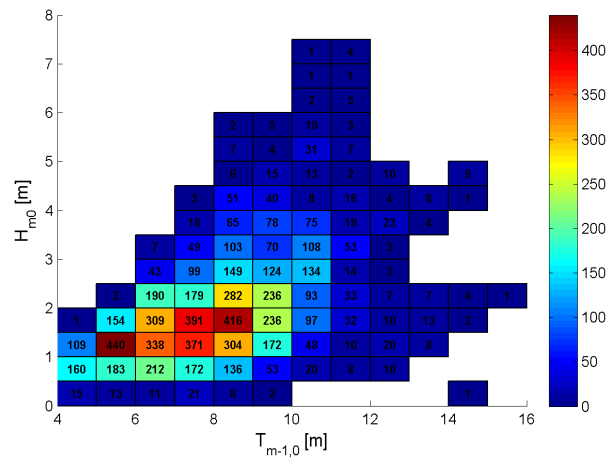


Figure 84: Number of observations Exeter wave buoy D

Figure 85 and Figure 86 present the same information as in the previous figure, but now presented in scatter plots.

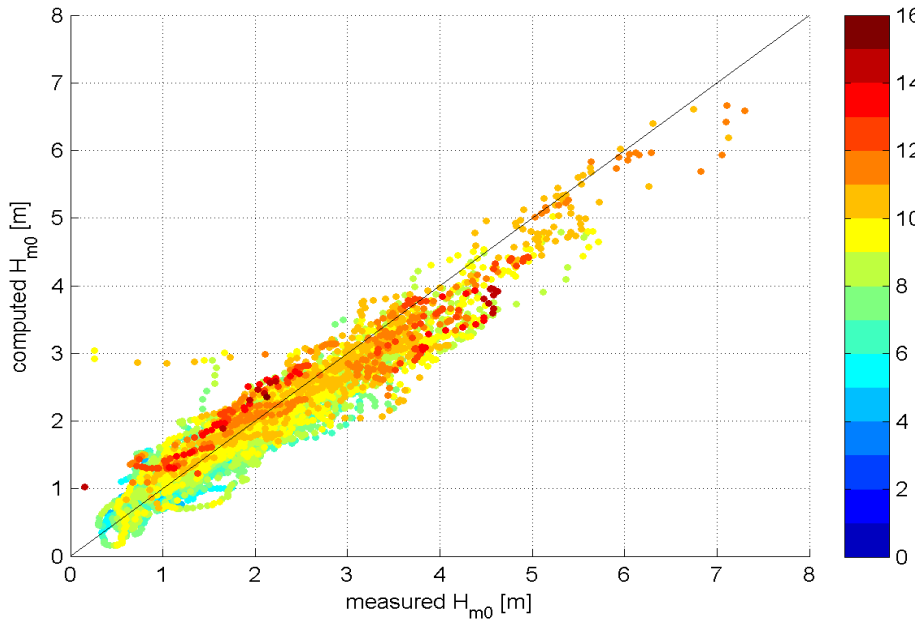


Figure 85: Scatter plot H_{m0} , Exeter wave buoy D, for different values of T_{m-10} [s] (see colour bar).

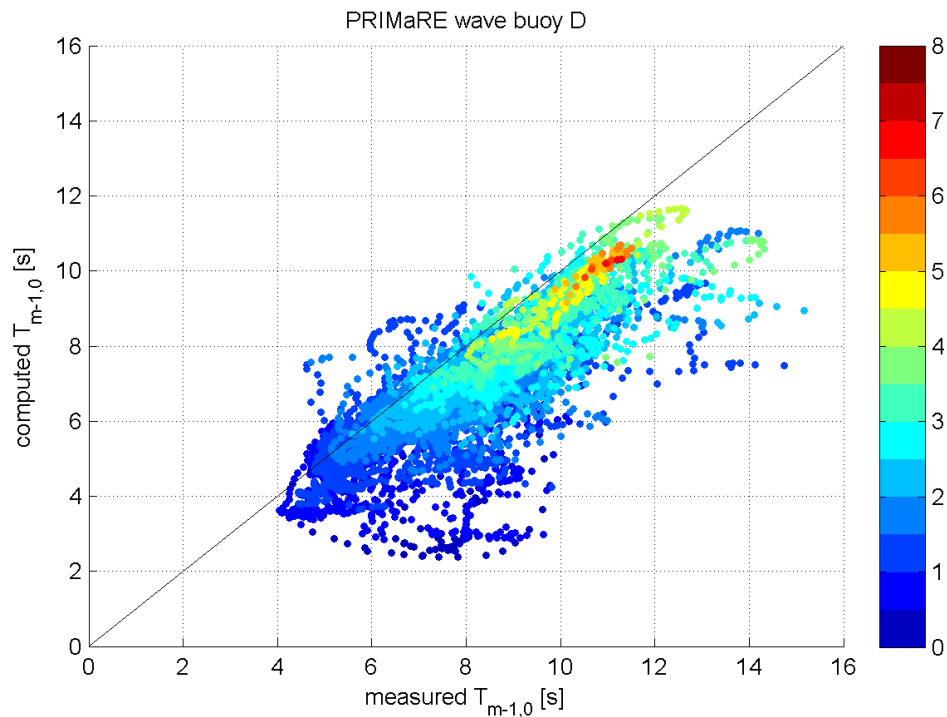


Figure 86: Scatter plot T_{m-10} , Exeter wave buoy D, for different values of H_{m0} [m] (see colour bar).

Error dependence on wave direction

Figure 87 and Figure 88 show the bias and scatter of H_{m0} and T_{m-10} per wave direction respectively. Most waves come from a westerly direction. It can be seen that most wave height errors are less than 1 meter. The positive and negative errors cancel each other out and therefore the bias is very small. As the wave heights are more often under- than overestimated, the bias is in most directions slightly negative. The largest errors are found for waves from south-westerly and north-easterly directions. For T_{m-10} the largest bias and root mean square errors come from waves with southerly directions. Errors up to 4 seconds are seen. However, most errors are in the order of 1 second.

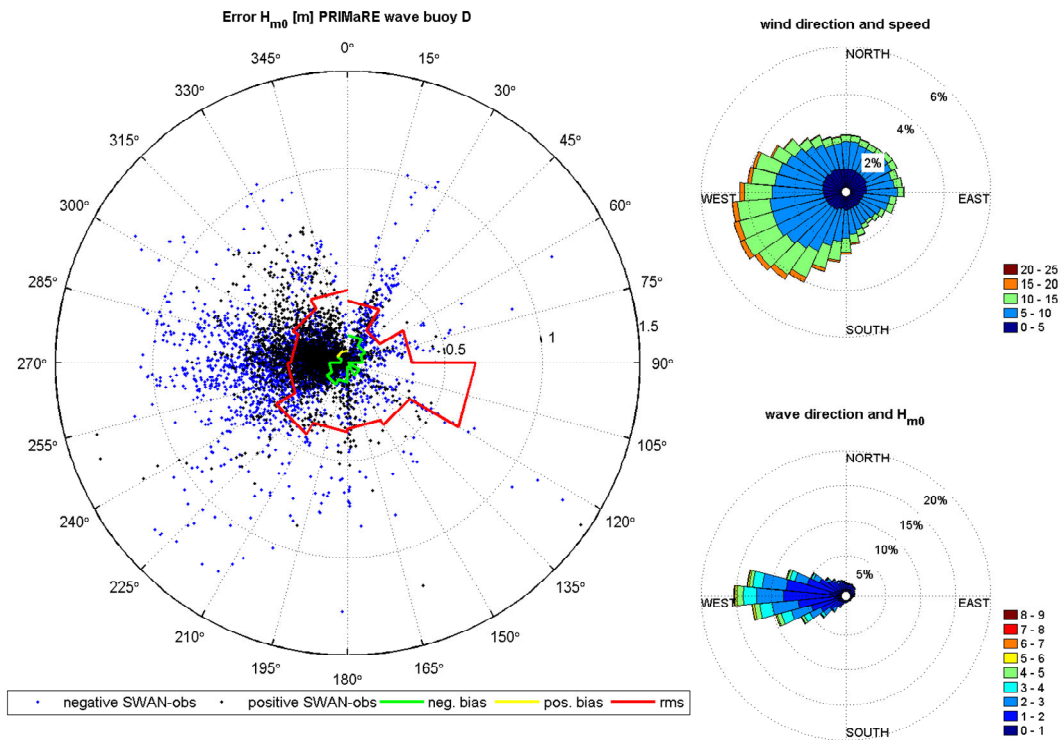


Figure 87: Bias and scatter H_{m0} vs wave direction, Exeter wave buoy D.

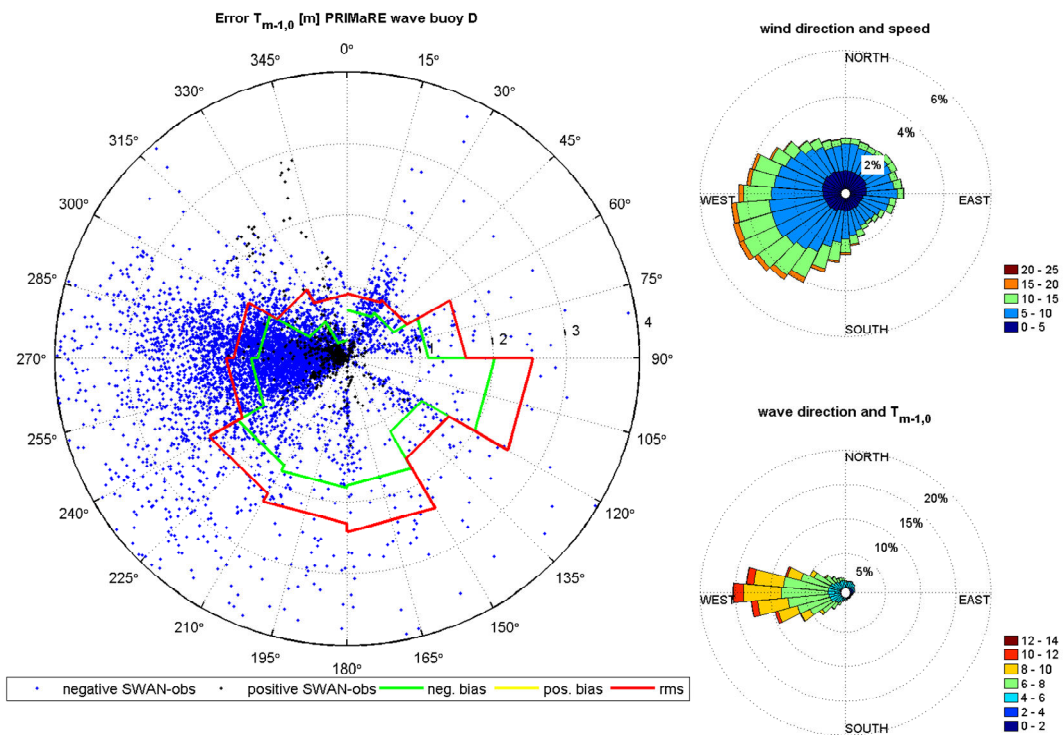


Figure 88: Bias and scatter T_{m-10} vs wave direction, Exeter wave buoy D

Error dependence on season

Figure 89 and Figure 90 show the variation in time of the bias in H_{m0} and $T_{m-1,0}$. For this analysis the figures for Perranporth are shown, as Perranporth has the longest measured dataset and is also located on the north coast of Cornwall. It can be seen that there is some monthly variation in the errors. The larger errors are more likely to occur in the winter months than in the summer months.

Figure 89 also shows the mean annual variation of the bias. Each year of the dataset was divided into spring (March, April, May), summer (June, July, August), autumn (September, October, November) and winter (December, January, February) datasets, and the mean power calculated. It can be seen that there is little annual variation of the bias.

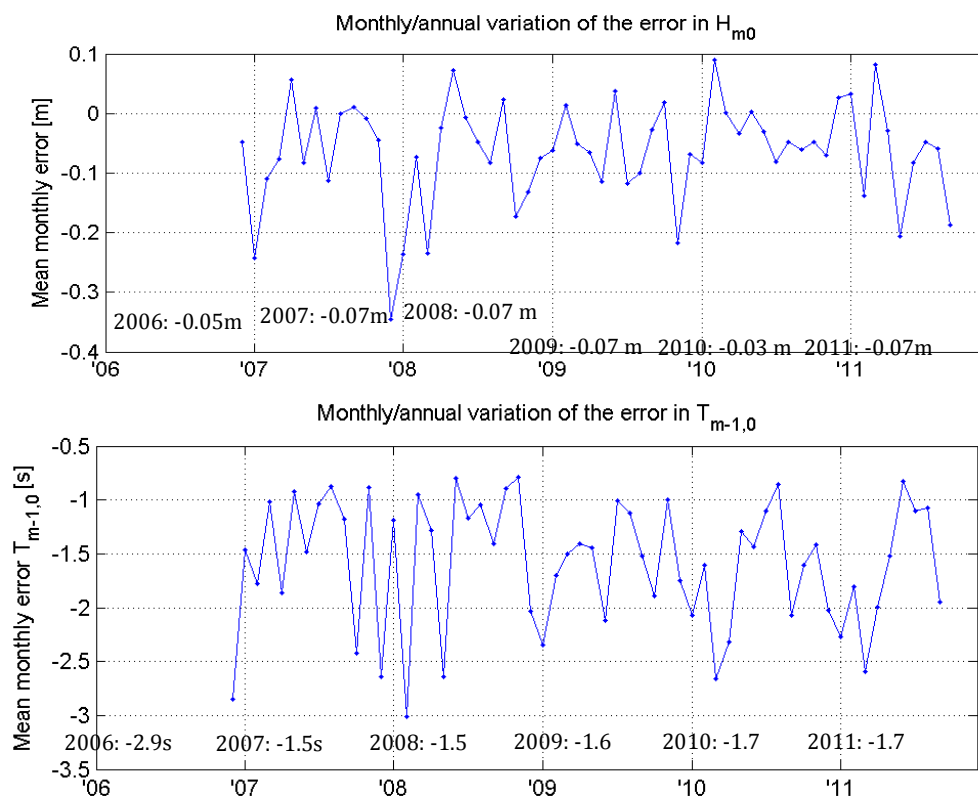


Figure 89: Monthly/annual variation of the errors in H_{m0} and $T_{m-1,0}$ Perranporth

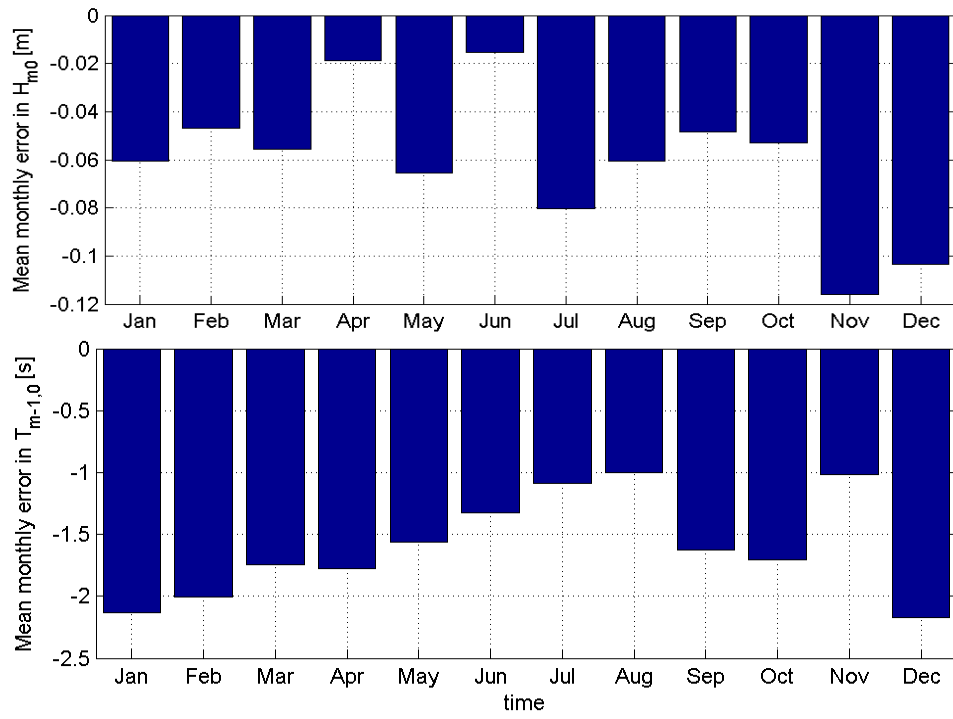
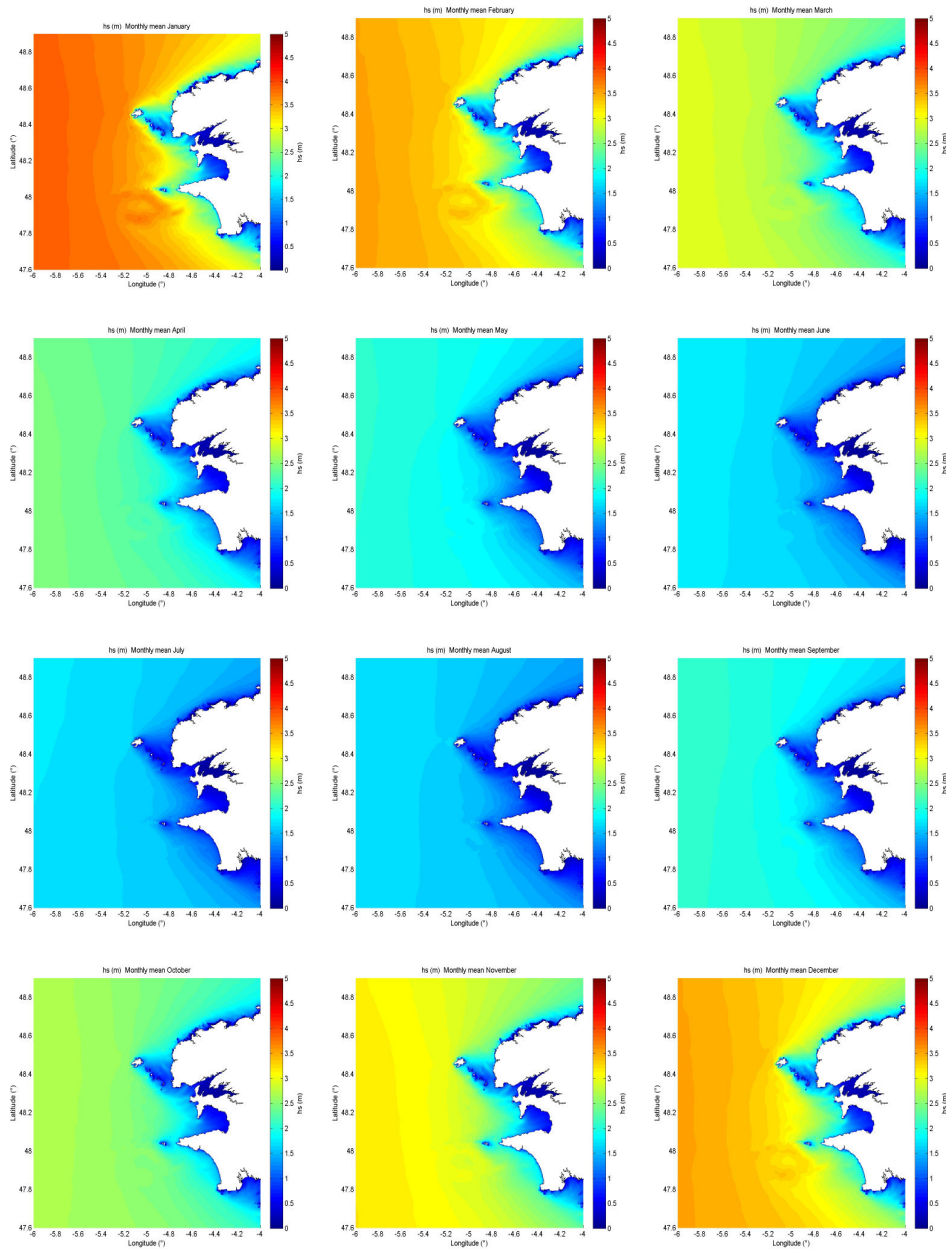


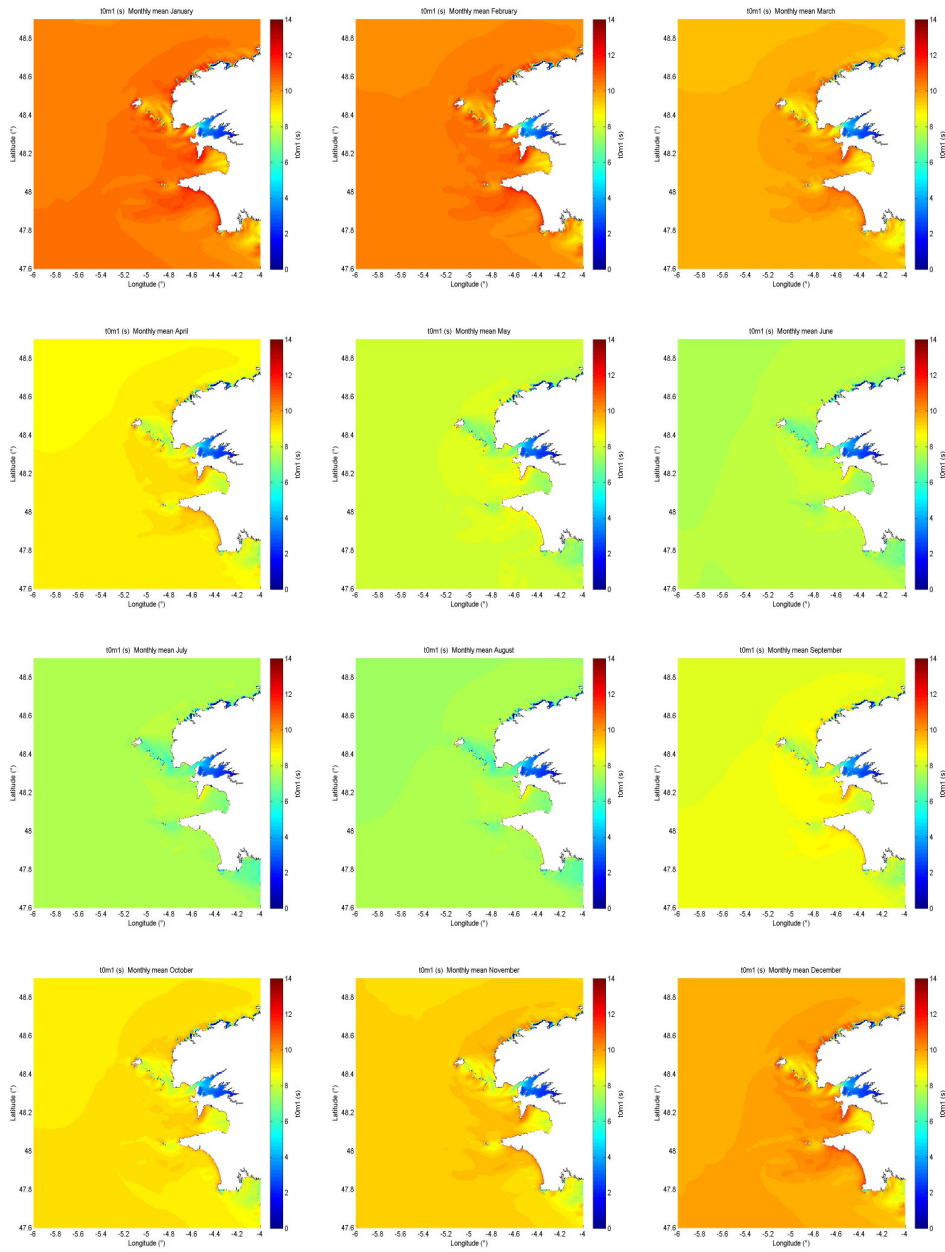
Figure 90: Mean monthly error for H_{m0} and T_{m-10} Perranporth

Appendix B: Iroise Sea wave parameters regional maps

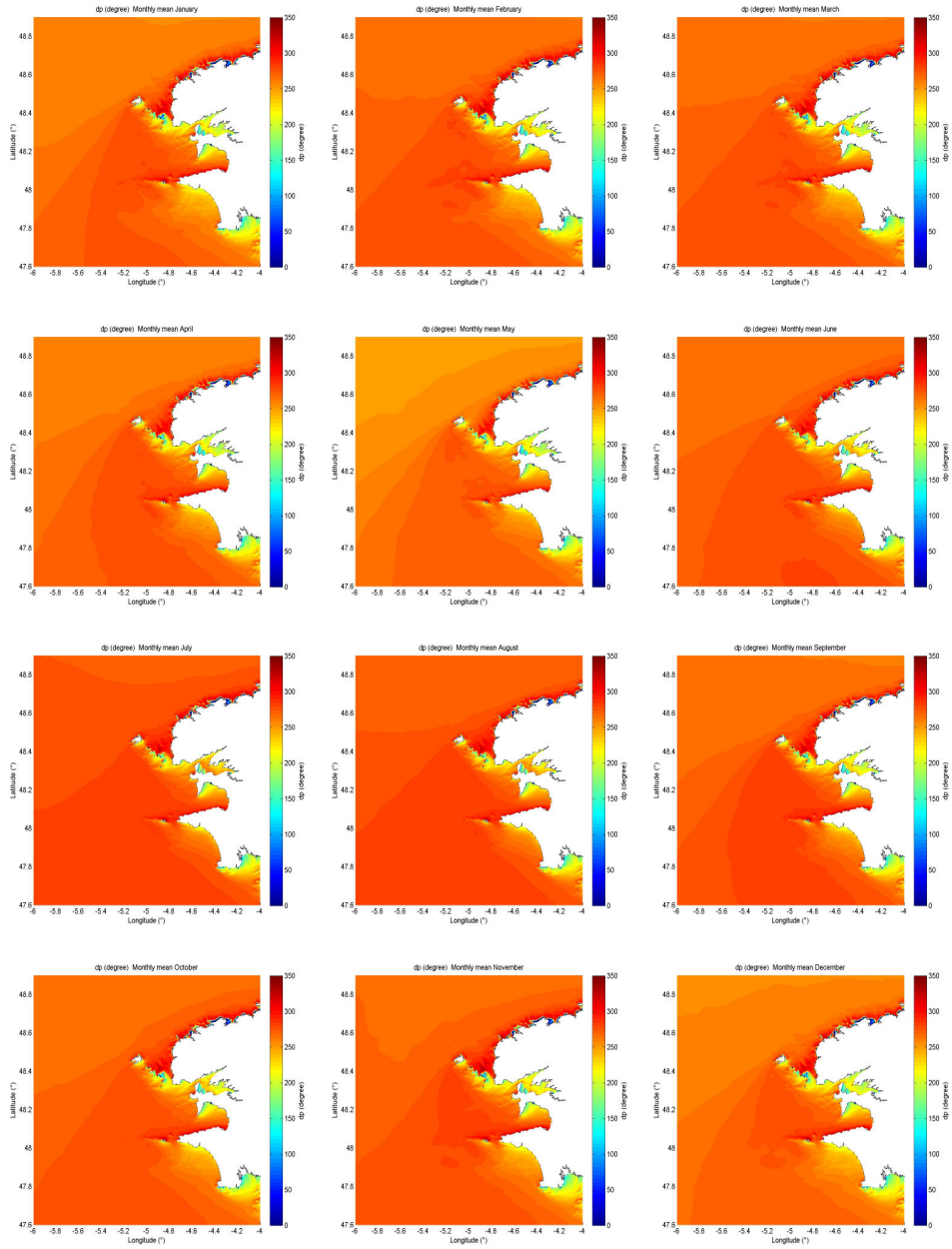
Significant wave height H_s (m) – Monthly mean



Energy Period $T_{m-1,0}$ (s) - Monthly mean



Peak direction D_p (°) - Monthly mean



Power C_gE (kW/m) - Monthly mean

